IMPERIAL COLLEGE LONDON

UNIVERSITY OF LONDON

FAR-FIELD SUPER RESOLUTION IMAGING

by

Matthew James Fleming

A thesis submitted to the University of London for the degree of

Doctor of Philosophy

Department of Mechanical Engineering

Imperial College London

London SW7 2AZ

August 2008

Abstract

Wave based imaging methods aim to build an accurate reconstruction of the physical properties of an object by recording the scattered field caused by illumination from multiple directions. Classically the minimum distance between the characteristics of the object that can be resolved by an imaging method is limited by the wavelength, λ, of the interrogating field. In order to improve the resolution shorter wavelengths can be propagated; however, due to material absorption, this limits the penetration depth of the wave which consequently reduces the potential imaging range. Any imaging technique which can overcome the resolution limit is of great practical and academic interest and represents the subject of this thesis.

Subwavelength characterisation has become well established in the field of Near-field Scanning Optical Microscopy which requires part of the probing system to be within λ of the object being illuminated (near field), in order to detect the non-propagating evanescent waves. The super-oscillatory properties of the evanescent waves are subsequently used to achieve subwavelength resolution. However, access to the near field of an object is not always feasible and since evanescent waves decay exponentially they cannot be directly detected in the far field (greater than λ from the object).

The aim of this thesis is to define and investigate an imaging strategy that will allow super resolution to be achieved from the far field. Conventional imaging techniques, which are constrained by the resolution limit, neglect the distortion of the scattered field caused by the internal structure of the object. This thesis will show that a more accurate description of the interaction of the incident field with the object, which includes the multiple scattering of evanescent waves, can lead to subwavelength resolution from the far field.

Acknowledgements

I would like to sincerely thank my supervisors Prof. Mike Lowe and Dr. Francesco Simonetti for their guidance, supervision, frank discussions and seemingly endless patience.

Furthermore, I would like to thank Prof. Peter Cawley and the various members of the NDT laboratory and associated peers who created a working environment that was both stimulating and enjoyable. I am also indebted to Prof. Richard Craster who first introduced me to the NDT group in 2003.

I also extend my thanks to the many members of the wardening team of Fisher Hall, with whom it has been a pleasure to live and work with.

I would also like to thank my parents and my sisters for their encouragement and support throughout my studies. Finally, I would like express my gratitude to Becca, for everything.

Contents

List of Figures

List of Tables

Nomenclature

$\mathbf{a}$	Vector made up of the scattering coefficients in the two cylinder scattering problem
$\mathbf{a_j}$	Coordinates of the j^{th} array element
A	Random Gaussian variable with zero mean and a standard deviation of 1
A_n^1	Coefficient corresponding to the scattering at the first cylinder
A_n^2	Coefficient corresponding to the scattering at the second cylinder
$\mathbf{b}$	Vector made up of the incident field for the case of two cylinder scattering problem
c_0	Background velocity
c_N	Noise level
$\mathbf{C_0}$	Covariance matrix
$\mathbf{C_{0N}}$	Matrix made up of the eigenvectors of the noise space of the $\mathbf{C_0}$ matrix
d	Separation distance between point scatterers
d_A	Longest distance from the transmitter to the receiver
D	Support of the object function
$\mathbf{D}$	Matrix representing the scattering caused by point scatterers
E^x	Information parameter measured along the Ω_x axis
E^y	Information parameter measured along the Ω_y axis
E_λ	Number of elements per wavelength
f	Scattering amplitude
f^M	Maximum temporal frequency
g_∞	Steering function
$\mathbf{g}$	Steering function
G	Green's function
G_∞	Asymptotic Green's function
G_0	Wave propagation between 2 point scatterers
$\mathbf{G}_\xi$	Regularization parameter
H	Point spread function
$\mathbf{H}$	Propagation of signals from scatterers/sources to array elements
H_n	n^{th} order Hankel function of the first kind

continue on next page

continue from previous page

J_n	n^{th} order Bessel function of the first kind
k_0	Wavenumber
$\mathbf{K}$	Multistatic response matrix
$\mathbf{K_0}$	Noisy $\mathbf{K}$ matrix
$\mathbf{K}_\infty$	Far-field operator
$\mathbf{M}$	Scattering matrix for the case of two cylinders
n	Index of refraction
N	Number of array elements
n_0	Noise parameter
$\mathbf{n_0}$	Noise vector
$\mathbf{N_0}$	Noise matrix
O	Object function
$\mathbf{p}(t)$	Signals recorded in the passive case
q	Random variable with a uniform distribution between $[-1\ 1]$
r_0	Characteristic size of the object
$\hat{\mathbf{r}}$	Detection direction
$\hat{\mathbf{r}}_\mathbf{0}$	Illumination direction
R	Radius of the array
$\mathbf{s}(t)$	Temporal signals produced by point sources
$\mathbf{S}$	Scattering matrix as described in quantum mechanics
t	Time
t_c	Time period over which all measurements must be taken
$\mathbf{T}$	Time reversal matrix
$\mathbf{T}_\infty$	Time reversal operator
v	Eigenfuction
$\mathbf{v}$	Eigenvector
$\mathbf{w}$	Weight vector
$\mathbf{z_j}$	Coordinates of the j^{th} point scatterer/point source

continue on next page

continue from previous page

Δr	Separation distance between array elements
Δt	Timestep
θ	Angle of illumination
ϑ	Function of a singular system
κ	Compressibility
λ	Wavelength
μ	Eigenvalue
ν	Born Approximation validation constant
ρ	Density
σ	Standard deviation of noise
σ_T	Total cross section
τ	Scattering coefficient
ϕ	Angle of detection
φ_1	Angle of incidence
φ_2	Angle of reflection
φ_c	Critical angle
ψ	Total wavefield
ψ_i	Incident field
ψ_s	Scattered field
ω	Angular frequency
Ω	Spatial frequency

Abbreviations:

ADC	**A**nalog to **D**igital **C**onverter
BA	**B**orn **A**pproximation
BM	**B**artlett **M**ethod
DAC	**D**igital to **A**nalog **C**onverter
DORT	**D**écomposition de l'**O**pérateur de **R**etournement **T**emporel

continue on next page

continue from previous page

ML	**M**aximum **L**ikelihood
MS	**M**ultiple **S**cattering
MUSIC	**Mu**ltiple **Si**gnal **C**lassification
NSOM	**N**ear-field **S**canning **O**ptical **M**icroscopy
RADAR	**Ra**dio **D**etection **a**nd **R**anging
SONAR	**So**und **N**avigation **A**nd **R**anging
TR-MUSIC	**T**ime **R**eversal and **Mu**ltiple **Si**gnal **C**lassification

Chapter 1

Introduction

1.1 Motivation

An image can be considered as the visual representation of data received at a detector or array of detectors. This seemingly prosaic definition describes a process which is not only used at the forefront of a wide variety of scientific research but has also found many diverse commercial applications. For centuries imaging systems have relied upon light scattered in the so called 'visible range' (this is light with a wavelength of $\sim 400 - 700nm$ to which the photoreceptive cells of the retina are sensitive), the electromagnetic spectrum including visible light is shown in Figure 1.1. In conjunction with devices such as telescopes and microscopes the use of visible light in imaging systems has been intrinsic in many important scientific discoveries from the cellular level, such as imaging the surface of parasites in malaria research [1] to the stellar level, including the heliocentric view of the solar system [2]. There is however information about the outside world that is not encoded into the frequency range of visible light and so consideration of electromagnetic waves outside of the visible range or mechanical waves (such as acoustic waves) that are invisible to the naked eye could provide insight into a variety of subject areas.

Imaging methods based upon information which is invisible to the naked eye have been investigated for little over a century. Whilst working in a darkened lab in 1895

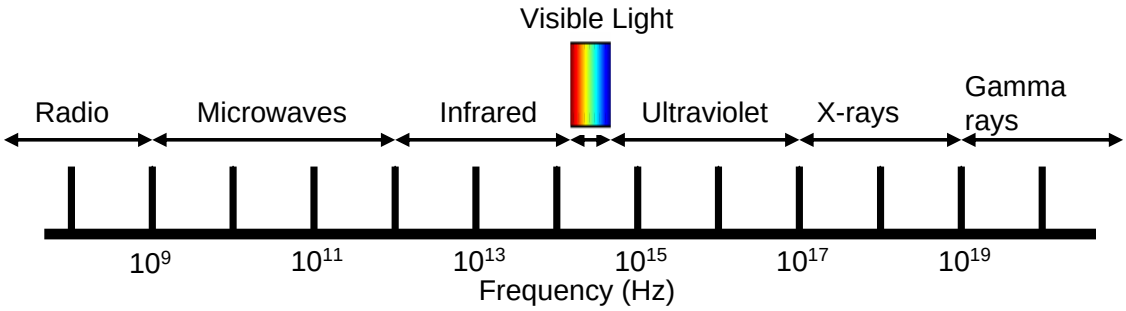

Figure 1.1: *The Electro-Magnetic Spectrum given in terms of frequency.*

Professor Wilhelm Röntgen discovered that it was possible to generate rays that could travel through media that are opaque to visible light [3]. Professor Röntgen was awarded the first Nobel prize for Physics in 1901 for this discovery [4], the rays (later termed 'x-rays') revolutionised the treatment of many medical conditions by providing high resolution images of the internal structure of the human body allowing diagnosis without having to use any invasive surgical procedures. More recently the field of Nuclear Magnetic Resonance (NMR) imaging has also been able to provide images of a patient's body non-invasively. NMR was first developed in the 1940s independently by Purcell [5] and Bloch [6] who observed the magnetic resonance of paraffin and water respectively; they were later both awarded the Nobel prize for physics in 1952 for their achievements. The field received much attention in the 1970s when it was shown that not only could NMR be used to image the internal structure of an object [7], but also that cancerous tissue behaved differently to healthy tissue when probed [8]. Currently NMR imaging methods can provide very high resolution images of a patient's internal structure thus aiding doctors in the diagnosis of many medical conditions, see for example [9], an NMR image of the author is shown in Figure 1.2.

Aside from the imaging of patient's bodies, x-rays have also been fundamental in understanding the universe at the atomic level. In 1912 Max Theodor Felix von Laue published a paper for which he would later receive the 1914 Nobel prize for physics which simultaneously proved the wave like nature of x-rays and the lattice structure of crystals. The interested reader can find out much on the history of

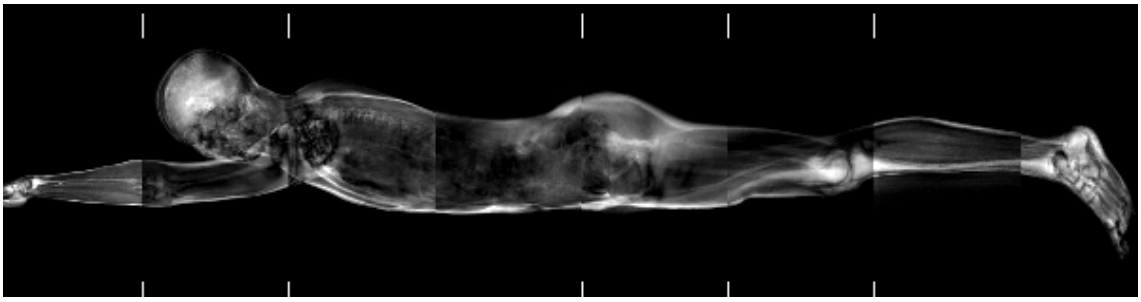

Figure 1.2: *NMR image of the author.*

x-ray diffraction in the book by Ewald [10] and the paper by Jensen et. al. [4]. This discovery led to the foundation of the field of x-ray diffraction and another Nobel prize awarded to Sir William Bragg and Sir Lawrence Bragg [11] who discovered that x-rays could be used to image the structure of chemical compounds by studying the interference pattern produced by firing x-rays at the compound in question. Amongst the many achievements of x-ray diffraction it has aided the discovery of the structure of DNA by James Watson and Francis Crick [12] and led to the synthesis of penicillin by Dorothy Hodgkin [13] which has saved countless lives.

Imaging using means outside of the visible spectrum is not just limited to the use of x-rays. Electromagnetic waves with much lower frequency ranges are used to locate aircraft in RAdio Detection And Ranging (RADAR) [14] [15] and are also used in radio astronomy [16] [17] in order to probe skies for information about stellar bodies. In a similar fashion mechanical waves have been exploited leading to the well established fields of SOund Navigation And Ranging (SONAR) [18], ultrasound [19] [20] [18] and geophysical exploration [21] [22] [23]. This is by no means an exhaustive list of the applications of imaging methods but is designed to provide an insight into the diverse range of fields to which imaging can be applied.

All of the imaging systems mentioned can only be considered useful if the images they produce are of a high enough resolution. Although it is difficult to give a rigorous definition of resolution, it can be described as how well an image displays the qualities or characteristics of the object it represents. A completely resolved image would represent all of the features of the object under consideration. As an example Figure 1.3 (a) shows a well resolved image of the hieroglyphics on the side

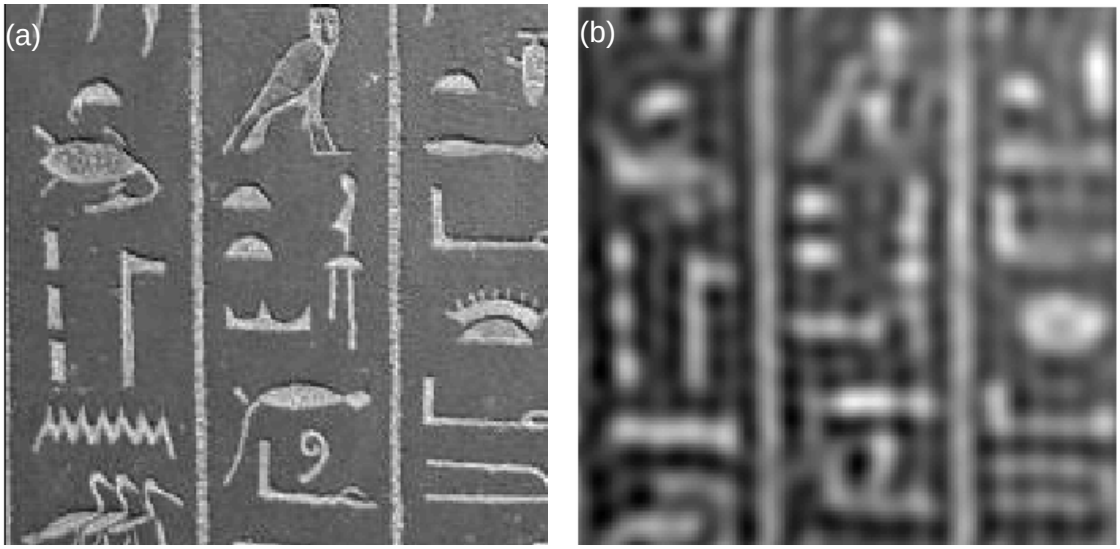

Figure 1.3: *Image of hieroglyphics on the side of a sarcophagus in the British Museum, 2007. (a) The well resolved image: the symbols on the sarcophagus are easily identifiable; (b) less resolved image: the symbols in this image have become blurred and are no longer identifiable.*

of a sarcophagus in the British Museum; the symbols in this image are clearly resolved and easily identifiable. A less resolved version of the hieroglyphics is shown in Figure 1.3 (b); the symbols in this image have become more blurred meaning information about the characteristics has been lost and so interpretation of the symbols would be difficult if not impossible. This simple example illustrates that in order for any image to provide useful information it must achieve sufficient resolution.

The first attempts to understand the physics behind resolution were carried out by Ernst Abbe [24], whose work was later reformulated by Lord Rayleigh [25] [26] [27] who determined that in order to be resolved, the minimum distance between two features within a medium must be of the order of the interrogating wavelength λ. It was determined that this limit affects all imaging methods using either electromagnetic or mechanical waves.

In some cases such as in NMR or certain applications of x-rays, the resolution of the image produced is more than adequate to resolve the required features of the medium being probed. However, both x-ray and NMR imaging systems require the

medium being imaged to be enclosed within the imaging system as shown by the full view configuration in Figure 1.4 (a). In many applications such as RADAR, SONAR and geophysical exploration only a limited view of the medium under consideration is available as shown schematically in Fig 1.4 (b). In this case images can be constructed by processing the backscattered field of one or multiple interrogating waves (electromagnetic or acoustic). The backscattering results from the interaction of the wave with any characteristics within the medium and due to the diffraction phenomenon results in images that are affected by the Rayleigh resolution limit. As the Rayleigh limit is concerned with the wavelength λ of the interrogating wave, a wave with a shorter wavelength could be propagated through the medium in order to resolve closely spaced features. However, decreasing the wavelength of the interrogating wave also decreases its effective penetration depth due to absorbtion, meaning the range of the imaging method will be reduced. It should also be noted that in some applications such as astronomy or some forms of RADAR (such as the Silent Sentry system or the Manastash Ridge Raider [15]) the system can be passive meaning the interrogating waves and their frequencies are not controlled by the observer. What is more, in ground based astronomy the ionosphere acts as a filter, only allowing waves of a certain frequency to be detected, in which case a method which could improve the resolution of an image at a fixed frequency is desirable.

In order for a wave based imaging method to be able to resolve subwavelength characteristics, a way must be found in order break the resolution limit; any imaging method that is capable of this will have achieved what is termed 'super resolution'.

1.2 Super Resolution Imaging

When waves are scattered by an object within a medium both propagating and nonpropagating (or evanescent) waves are produced. The propagating waves can be detected many wavelengths from the object, whereas the evanescent waves decay exponentially and so their detection is only possible in close proximity to the scatterer. The propagating waves contain information about the structure of the scatterer but

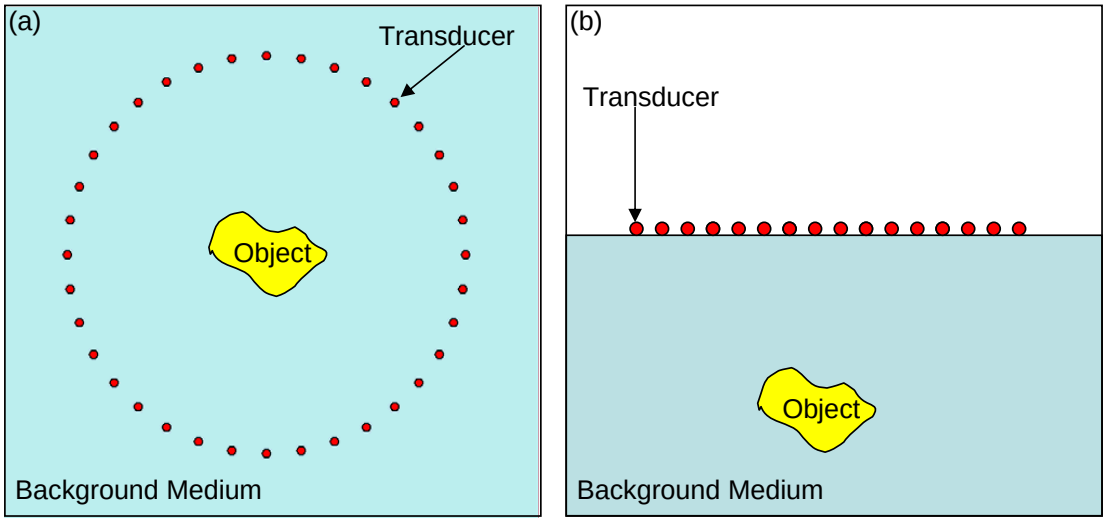

Figure 1.4: *Two possible configurations for the imaging system, (a) Circular array of sensors making an enclosed system; the array completely surrounds the object providing illumination from all directions (b) Linear array of sensors also known as partial view system; the object is not enclosed by the array and illumination is only provided from a limited range of directions.*

this information is limited by the size of the wavelength of the interrogating wave so that subwavelength information cannot be derived directly from the propagating waves. On the other hand, evanescent waves contain subwavelength information on the structure of the scatterer.

Close to the surface of the object the wavefield undergoes spatial fluctuations that occur over a scale comparable to the spatial scale of the features of the surface regardless of the wavelength. These fluctuations are the contribution from the evanescent fields and the subwavelength structure of the specimen could be determined from these fields. However, as the distance from the object increases it becomes more difficult to detect the subwavelength features as the evanescent waves decay. In 1928 Synge [28] realised that by measuring the evanescent waves produced by scattering, subwavelength information about the medium could be determined, thus breaking the Rayleigh limit and achieving super resolution. Synge stated that by scanning a source with a subwavelength aperture within one wavelength (near field) of the surface of a specimen, super resolution could be achieved. It was not until 1972

that this concept was proven experimentally by Ash and Nicholls [29] who managed to resolve features separated by $\lambda/60$ in the microwave regime. Since then this idea has developed into the now well established area of Near-field Scanning Optical Microscopy (NSOM) (see for example Betzig et al. [30], Courjon [31] and Lewis et al. [32]).

There are three general approaches to NSOM as discussed in [33]: illumination mode, collection mode and apertureless. In illumination mode, the specimen is probed by a source with a subwavelength aperture (or tip) within λ of the surface. The evanescent fields produced at the aperture interact with the surface which converts the evanescent fields into propagating fields, which can then be detected in the far field (greater than λ from the specimen) this effect is known as tunneling, this method is shown schematically in Figure 1.5 (a). Due to reciprocity the roles of source and detector in illumination mode can be switched giving equally valid results; this is known as collection mode, in which case the source is in the far field and a detector with a subwavelength aperture is in the near field. Again the evanescent fields produced at the surface are converted into propagating fields through interaction with the tip as shown schematically in Figure 1.5 (b). In apertureless techniques shown in Figure 1.5 (c), the source and receiver are both in the far field. The propagating wave is scattered by the surface, and the evanescent waves produced at the surface are then converted into propagating waves by interacting with a subwavelength tip which is brought into the nearfield. Measuring the converted evanescent fields induced by having part of the system in the near-field is essential to NSOM and enables subwavelength resolution to be achieved.

An alternative approach to near field super resolution with electromagnetic waves is to use a metamaterial (which has a negative refractive index) to focus the scattered field as shown by Pendry in [34]. The interesting subject of metamaterials has received much attention recently as it provides the possibility of being able to bend electromagnetic waves around objects making them effectively invisible [35]. Theoretically metamaterials can be used to form a perfect lens which would actually amplify the evanescent fields allowing unlimited resolution to be achieved. Super

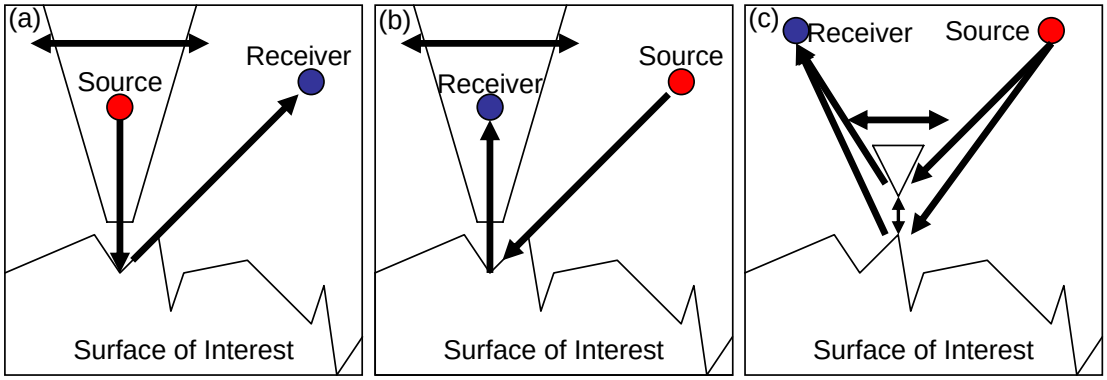

Figure 1.5: *The three types of NSOM, arrows indicating the path of the wave. (a) Illumination Mode: a source with a subwavelength aperture in the near field illuminates the surface of the sample, the resulting field is detected in the far field. (b) Collection Mode: the sample is illuminated from the far field and the resulting scattered field is detected in the near field by a receiver with a subwavelength aperture. (c) Apetureless: illumination and detection take place in the far field but a subwavelength tip is introduced into the near field to induce the tunneling of evanescent fields.*

resolution in the near field has been achieved experimentally using this method [36], however the resolution of the image is limited by the quality of the metamaterial.

In many applications access to the near field is not possible due to the features of interest being encased in a surrounding medium. In this case far field imaging (when the probing system is greater than λ from the region of interest) must be employed. As an example in medical ultrasound, a typical wavelength is $\lambda \approx 1mm$ [19] [20]. For non-invasive imaging the probing sensor has to be placed in contact with the skin, thus any structure inside the body will be tens or hundreds of λ from the probe. Therefore, excitation and reception of any wavefields must take place in the far field.

Far-field state-of-the-art imaging systems are based on the assumption that scattering of waves can be treated as the superposition of independent scattering events caused by each feature of the object acting separately; this is known as the Born Approximation. Consequently if an object consists of M features then the scattered field is considered to be the summation of the interactions of the incident field

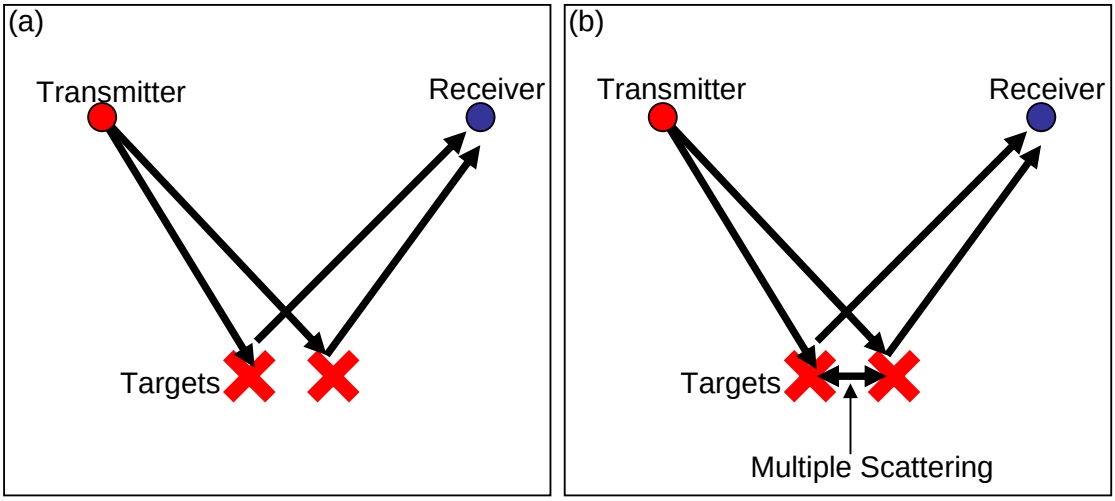

Figure 1.6: *Simple case of two scatterers. (a) Path of the scattered field under the Born Approximation; there is no interaction between the scattered fields and the targets and the resulting scattered field is the summation of the fields that would be produced if the targets were interrogated in seclusion. (b) Path of the scattered field including multiple scattering; in this case the scattered field does interact with the targets.*

from each of the features considered in seclusion. Consider the situation shown in Figure 1.6 (a), consisting of two point scatterers being probed by an incident field. Under the Born Approximation the field scattered by one of the targets does not interact with the other. This assumption precludes the possibility that subwavelength information can be conveyed to the far field as the evanescent waves do not contribute to the scattered field measured in the far field.

However, it can be observed that if the interaction of the fields scattered by different features is considered, the evanescent waves contribute to the far field. In fact, as in the case of NSOM, due to tunneling, the interaction of the purely evanescent waves causes energy fluctuations in the far field. Since evanescent waves contain subwavelength information, this multiple scattering mechanism should lead to the encoding of subwavelength information in the far field. This idea is similar to that used in NSOM. However in contrast with NSOM, where some part of the system is introduced into the near field of the specimen in order to cause the conversion of the evanescent fields into propagating fields, this approach does not rely on any part of the imaging system being in the near field. Instead the evanescent fields are

converted by interaction with other characteristics within the medium; this is shown schematically in Figure 1.6 (b).

1.3 Outline of Thesis

In this thesis, imaging techniques which can achieve super resolution by incorporating the effects of multiple scattering into the imaging method will be considered. The thesis will focus on achieving super-resolution imaging of objects in the far field of the imaging system. This study could dramatically improve the resolution achieved by current imaging technology thus allowing images with unprecedented information to be produced. This would benefit a variety of scientific endeavours potentially saving time, money and even lives.

In order to explore the possibility of far-field super resolution, this thesis will be split into the chapters described below. The thesis starts by providing the background and theory of scattering and outlining a general framework for super-resolution imaging. In particular a rigorous description of imaging as an inverse scattering problem is derived. Subsequently Chapters 6-8 provide a number of examples showing the feasibility of super-resolution imaging from the far field.

Chapter 2 will describe the forward scattering problem, which aims to determine the scattered field resulting from the illumination of a given object. This problem will be discussed under the Born Approximation and when the effects of multiple scattering are included. In order to describe this problem successfully, this chapter will include descriptions of the governing equations of wave propagation.

Having described the forward scattering problem in Chapter 2, Chapter 3 will investigate the inverse scattering problem, which aims to reconstruct the object from a given scattered field. Strategies for dealing with the non-linear, ill-posed nature of the inverse problem will be discussed in this chapter. The first imaging algorithm to be considered in this thesis (the Factorization method) will be presented in Chapter 3 as an approach of dealing with the non-linear, ill-posed inverse problem. The

consequence of assuming the Born Approximation or Multiple Scattering models on the reconstruction of the object will also be examined.

The theory discussed in Chapters 2 and 3 assumes that illumination of the object under consideration and detection of any subsequent scattered fields can be executed for every possible direction. In practice, illumination and detection occur at a discrete number of points that make up an array. Chapter 4 will discuss the practical and theoretical aspects of utilizing an array of transducers in order to illuminate an object and detect any subsequent scattered fields.

In Chapter 5 the Bartlett, Time Reversal and MUSIC and Maximum Likelihood imaging algorithms will be discussed. These imaging algorithms were originally derived to be used under a passive array system (which does not actively illuminate the object), as such this chapter will explore the link that exists between the passive and active array systems. The imaging algorithms will be adapted to be used under an active system and so will be used in subsequent chapters to reconstruct an object from the scattered field resulting from the illumination of the object by the array.

The analytical expression for the scattered field resulting from the illumination of two subwavelength separated point scatterers under both the Born Approximation and Multiple Scattering forward models will be investigated in Chapter 6. It will be shown that the inclusion of multiple scattering in the forward problem leads to a scattered field which contains more information on the subwavelength structure of the object, than is obtained under the Born Approximation. The robustness of the two forward models will be tested by adding noise to the analytical results and determining if the point scatterers are still resolvable from the corrupted data. Experimental results of the scattered field obtained from two subwavelength separated point-like scatterers will then be presented, the various imaging algorithms derived in previous chapters will be applied to this data to determine if the scatterers can be reconstructed from the scattered field and thus determine if super resolution is achievable experimentally.

Having investigated point scatterers in Chapter 6, Chapter 7 will investigate the

possibility of reconstructing extended objects from the measured scattered field. This chapter will introduce the idea of finite element analysis in order to simulate the scattered field that would be obtained from a given object. After investigating the validity of using finite element analysis in order to model the solution to the forward problem, this approach will be used to simulate the scattered field that would be generated by the cases of a cylinder and a square located at the centre of a circular array. The Factorization, Bartlett and Time Reversal and MUSIC algorithms will be applied to the finite element data to determine if the extended objects can be reconstructed, the robustness of this data to noise will also be evaluated.

The possibility of obtaining super-resolved images of extended objects will be investigated in Chapter 8. A semi-analytical model which describes the scattered field caused by the illumination of two subwavelength cylinders separated by a subwavelength distance will be considered. The scattered field in this case can be derived under either the Born Approximation or Multiple Scattering models. An investigation of the robustness to additive random noise of the two physical models will then follow. Finite element analysis will then be used in order to simulate the same forward problem. It will be shown that finite element analysis is unable to successfully model the multiple scattering of evanescent waves.

The main results and conclusions will then be summarised in Chapter 9, possible future areas of interest relating to the results presented in this thesis will also be discussed in this chapter.

Chapter 2

Forward Scattering

2.1 Introduction

The forward scattering problem consists of introducing a known incident wave into a known background medium and predicting the scattered field resulting from the interaction of the incident field and any inhomogeneities (described as Objects) present within the medium.

This chapter will outline the governing equations that describe the above problem for an acoustic wave field. In order not to over complicate the description of the governing equations or any subsequent expressions, analysis will assume a 2-D model only; the corresponding 3-D model will follow the same arguments. Moreover, the experiments and simulations carried out for this thesis will treat the 2-D case only. The governing equations will be used to study the structure of the scattered wave field in the far field. An approximate version of the scattered field will be investigated using the Born Approximation, it will be shown how this approach, which neglects the effects of multiple scattering, limits the amount of information conveyed to the far field. Finally the exact form of the far-field operator which describes the scattered field far from the object will be given and some of its properties investigated. This expression will be the starting point for discussion in the next chapter which deals with the inverse scattering problem and the possibility of achieving super resolution.

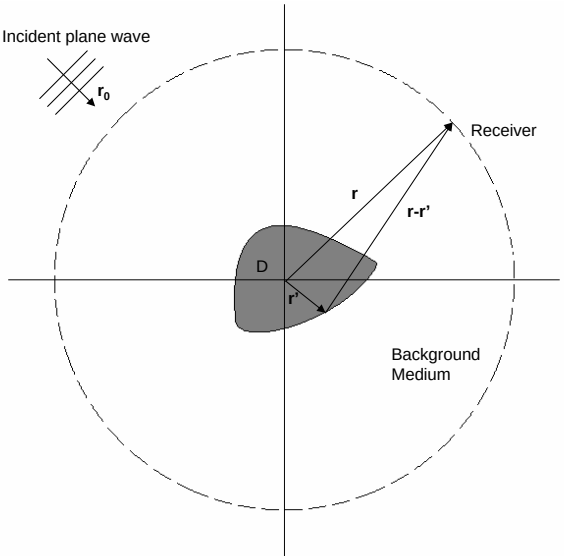

Figure 2.1: *Schematic of the scattering problem. The object is illuminated from direction* $\hat{\mathbf{r}}_\mathbf{0}$*, the resulting scattered field is detected in the far field.*

2.2 Governing Equations

In order to describe how a wavefield propagates through a medium, this section will consider the governing equations of the scattering problem. The forward scattering problem is to determine the scattered field when an object immersed in a background medium is illuminated by an incident wave, as shown schematically in Figure 2.1. It will be assumed that the object can be described by the so called 'object function' $O(\mathbf{r}, \omega)$ for a point in space $\mathbf{r}$ and the angular frequency ω determined by the incident wave. It is assumed that the spatial domain that the object occupies is given by D. Although the object function has a dependence on ω, implying a dependence on the frequency of the incident field, the analysis of the governing equations will only consider monochromatic wave fields, so any dependence on the angular frequency is taken as understood and dropped from any equations. The extension of this analysis to the case of polychromatic waves will be considered in Chapter 4 . The form of the object function depends upon the type of waves used to interrogate the object; in general the object function will depend upon the index of refraction, $n(\mathbf{r})$, and in the case of acoustic waves which will be the main concern of this thesis, it depends upon the compressibility, κ, and density, ρ, of the object [37] and is given by the

expression:

$$O(\mathbf{r}) = n^2(\mathbf{r}) - 1, \tag{2.1}$$

where:

$$n(\mathbf{r}) = c_0\sqrt{\rho(\mathbf{r})\kappa(\mathbf{r})}, \tag{2.2}$$

where c_0 is the velocity of the background medium.

The total wave field at any point within the background medium consists of the incident wave and the scattered wave caused by the interaction of the incident wave with the object. As this thesis is concerned with excitation and detection of wavefields in the far field it will be assumed that the incident wave can be represented by a plane wave. In the experiments that will be detailed in later chapters the system will not be illuminated by a plane wave but it is assumed that the region of interest is far enough away from the excitation point that the wavefront can be considered to be planar at the point at which interaction with the object occurs.

So far the description of the scattering system could be applied to the cases of electromagnetic or mechanical waves. As this thesis is mainly concerned with the application of acoustic waves it will be assumed that the wave field at the point $\mathbf{r}$ due to an illumination from the direction $\hat{\mathbf{r}}_\mathbf{0}$ can be described by the scalar potential $\psi(\mathbf{r}, \hat{\mathbf{r}}_\mathbf{0})$. This can also be used to describe electromagnetic waves if the effects of polarization are ignored. The interested reader can find out more about the representation of electromagnetic waves in the monograph by Jackson [38].

Taking into account the above assumptions, the governing equations of the 2-D scattering problem for an acoustic wavefield are:

$$\Delta\psi(\mathbf{r}, \hat{\mathbf{r}}_\mathbf{0}) + k_0^2\psi(\mathbf{r}, \hat{\mathbf{r}}_\mathbf{0}) = -k_0^2 O(\mathbf{r})\psi(\mathbf{r}, \hat{\mathbf{r}}_\mathbf{0}), \tag{2.3}$$

$$\psi = e^{ik_0\hat{\mathbf{r}}_\mathbf{0}\cdot\mathbf{r}} + \psi_s, \tag{2.4}$$

and

$$\lim_{r\to\infty} \sqrt{r}(\frac{\partial\psi_s}{\partial r} - ik_0\psi_s) = 0. \tag{2.5}$$

Equation 2.3 is known as the inhomogeneous wave equation or Helmholtz equation and represents how the wave field ψ propagates through the background medium and interacts with the object represented by $O(\mathbf{r})$. The quantity k_0 represents the wave number of the incident wave, and is derived from the angular frequency and the velocity of the background medium c_0, such that $k_0 = \omega/c_0$. Equation 2.4 represents the total wavefield represented by the incident plane wave given by the exponential function and the scattered field ψ_s which is unknown in the forward scattering problem. Equation 2.5 is known as the Sommerfield radiation condition; this is necessary to ensure that the scattered field vanishes as it approaches infinity. This system of equations for ψ guarantee the uniqueness and existence of a solution as discussed in [39].

2.3 Scattering Amplitude

Having defined the governing equations of the scattering problem in the previous section, this section will manipulate the equations so that they can be represented in a way that allows the scattered field to be given in terms of the known incident field and the object function which is also known. The first step is to derive the freespace Green's function $G(\mathbf{r}, \mathbf{r}')$ which describes how a wave field propagates from a point source $\mathbf{r}$ to an observation point $\mathbf{r}'$, in a completely homogeneous medium i.e. a medium which contains no objects. This function is a solution to the Helmholtz equation of the form:

$$\Delta G(\mathbf{r}, \mathbf{r}') + k_0^2 G(\mathbf{r}, \mathbf{r}') = \delta(|\mathbf{r} - \mathbf{r}'|), \tag{2.6}$$

where $\delta(|\mathbf{r}-\mathbf{r}'|)$ is the delta function which is zero when $\mathbf{r} \neq \mathbf{r}'$ and singular otherwise. The solution for $G(\mathbf{r}, \mathbf{r}')$ is given by:

$$G(\mathbf{r}, \mathbf{r}') = -\frac{i}{4} H_0(k_0|\mathbf{r} - \mathbf{r}'|), \tag{2.7}$$

where H_0 is a zero order Hankel function of the first kind. As $|\mathbf{r} - \mathbf{r}'| \to \infty$ Equation 2.7 has the asymptotic form:

$$G_\infty(\mathbf{r}, \mathbf{r}') = -\frac{e^{i(\frac{\pi}{4} + k_0 r)}}{\sqrt{8\pi k_0 r}} e^{-ik_0 \mathbf{r}\cdot\mathbf{r}'}. \tag{2.8}$$

The freespace Green's function describes how a wave field would propagate in a homogeneous background medium but is also invaluable in deriving a solution to the inhomogeneous wave equation.

After some manipulation of Equations 2.3, 2.4 and 2.5, the total wave field ψ can be given by the Lippmann Schwinger equation:

$$\psi(\mathbf{r}, k_0 \hat{\mathbf{r_0}}) = e^{ik_0 \hat{\mathbf{r}}_\mathbf{0}\cdot\mathbf{r}} - k_0^2 \int_D d^2 r' O(\mathbf{r}') \psi(\mathbf{r}', k_0 \hat{\mathbf{r}}_\mathbf{0}) G(\mathbf{r}, \mathbf{r}'). \tag{2.9}$$

The first term on the right hand side (RHS) of Equation 2.9 is the incident plane wave as given in Equation 2.4 and the integral term is the scattered field ψ_s. This representation allows the scattered field to be thought of as the superposition of infinite point sources distributed in D. Each of these sources has a strength proportional to the object function and the total field at that point. Considering this equation in the far field by allowing $r \to \infty$ gives:

$$\psi(\mathbf{r}, k_0\hat{\mathbf{r_0}}) = e^{ik_0\hat{\mathbf{r}}_\mathbf{0}\cdot\mathbf{r}} + \Pi f(k_0\hat{\mathbf{r}}, k_0\hat{\mathbf{r}}_\mathbf{0})\frac{e^{ik_0 r}}{\sqrt{r}}, \tag{2.10}$$

where:

$$\Pi = \frac{k_0^2 e^{i(\frac{\pi}{4}+k_0)}}{\sqrt{8\pi k_0}}, \tag{2.11}$$

and $f(k_0\hat{\mathbf{r}}, k_0\hat{\mathbf{r_0}})$, the scattering amplitude, is given by:

$$f(k_0\hat{\mathbf{r}}, k_0\hat{\mathbf{r}}_\mathbf{0}) = \int_D d^2r' e^{-ik_0\hat{\mathbf{r}}\cdot\mathbf{r}'} O(\mathbf{r}')\psi(\mathbf{r}', k_0\hat{\mathbf{r}}_\mathbf{0}). \tag{2.12}$$

In order to deal with the above integral the simplifying assumption of the Born Approximation which neglects the effects of multiple scattering, can be invoked, this approach will be investigated later in this chapter.

2.4 Spatial Frequency Domain

Before investigating the implications of the Born approximation it is useful to briefly outline the representation of $O(\mathbf{r})$ in the spatial frequency domain (here referred to as the $\mathbf{\Omega}$-space), obtained by means of the 2-D Fourier transform of the Object function:

$$\tilde{O}(\mathbf{\Omega}) = \int d^2r O(\mathbf{r}) e^{-i\mathbf{\Omega}\cdot\mathbf{r}}, \tag{2.13}$$

where $\mathbf{\Omega}$ is the spatial frequency. Conversely the geometric representation is obtained from the $\mathbf{\Omega}$-space by the inverse transform:

$$O(\mathbf{r}) = \frac{1}{2\pi}\int d^2\Omega \tilde{O}(\mathbf{\Omega}) e^{i\mathbf{\Omega}\cdot\mathbf{r}}. \tag{2.14}$$

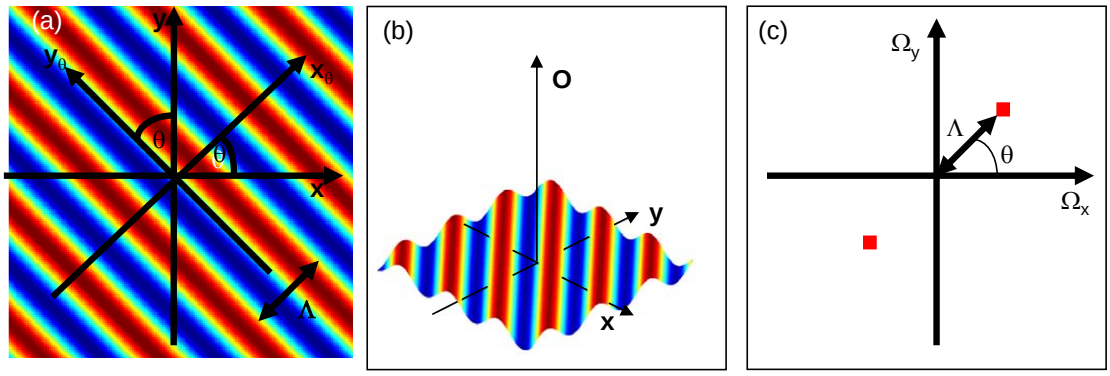

Figure 2.2: *Representations of a 2-D sinusoidal surface: (a) The surface viewed from above in geometric space, with a period of* Λ *rotated by* θ *about the* z *axis; (b) Tilted view of a portion of the sinusoidal surface; (c) Spatial frequency domain representation of the sinusoidal surface.*

Physically $\tilde{O}(\mathbf{\Omega})$ represents the object function $O(\mathbf{r})$ as a superposition of planar harmonics in the geometric space. To illustrate this, consider a sinusoidal surface in the geometric space as shown in Figure 2.2 (a) & (b). This surface is considered to be infinite in extent and traces a sine curve along the x_θ axis for every possible value on the y_θ axis, where the (x_θ, y_θ) axes are a rotation by θ of the (x, y) axes about the z axis. If the surface has a spatial period of Λ with respect to the x_θ axis, then it is fully described by two delta functions in the spatial Fourier domain $\mathbf{\Omega}$ positioned at $\Omega_x = \pm(2\pi/\Lambda)\cos\theta$ and $\Omega_y = \pm(2\pi/\Lambda)\sin\theta$ as shown in Figure 2.2 (c).

Clearly if the distance between the peaks of the sine wave representing the surface is halved then the distance between the two points in the spatial frequency domain is doubled. As a result, an object with characteristics that are closely spaced has higher spatial frequencies than one which has more widely spaced characteristics; in other words, the higher spatial frequencies represent the finer details of an object. If an Object described by $O(\mathbf{r})$ in the geometric domain, contains any subwavelength features then the spatial fourier transform of this function, $\tilde{O}(\mathbf{\Omega})$, will contain information on these features in the region $\Omega_r > k_0$.

As an example, consider the image of the Hieroglyphics (first shown in Chapter 1)

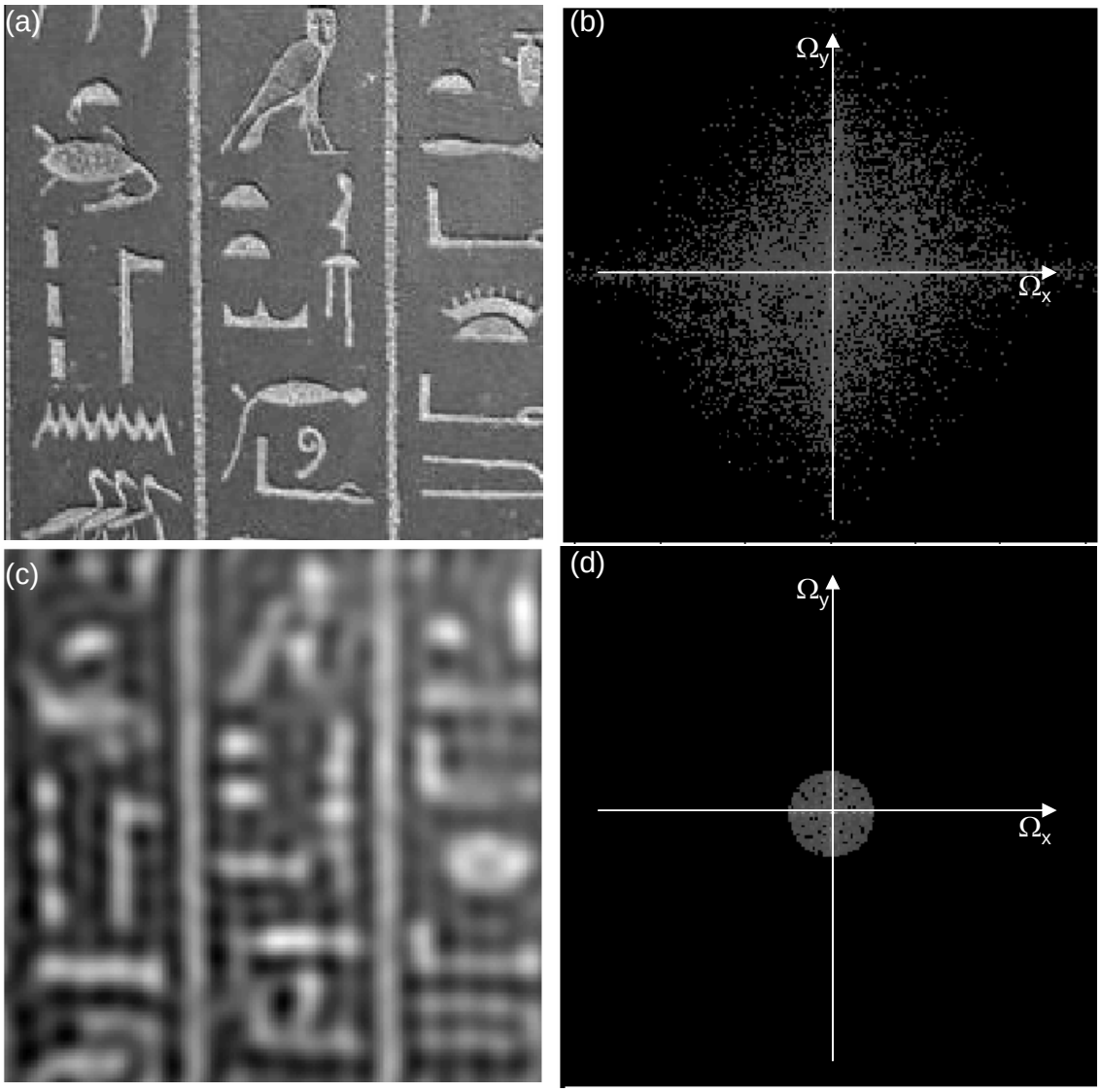

Figure 2.3: *Image of hieroglyphics represented in the geometric domain and the spatial frequency domain. (a) Original high resolution image of the hieroglyphics; (b) Ω-space representation of the original image; (c) Low resolution image of the hieroglyphics; (d) Ω-space representation of the low resolution image.*

shown in Figure 2.3 (a). A grey-scale map of the modulus of the spatial Fourier transform of this image is shown in Figure 2.3 (b); this has a maximum at the origin shown in white, and the minimum values are shown in black. The maximum at the origin represents the average intensity (or brightness) across the image; for the sinusoidal surface this value was zero. The features of the image with a low spatial frequency are represented near the origin in the $\mathbf{\Omega}$-space whereas the finer details are represented by higher spatial frequencies which are further from the origin. The low

resolution image in Figure 2.3 (c) was created by applying a low pass filter that sets the higher spatial frequencies of the transform of the original image to zero as shown in Figure 2.3 (d). By removing these higher spatial frequencies the original image becomes blurred and its finer details are lost. The importance of understanding the relationship between the geometric domain and the spatial frequency domain shall be revealed in the next section.

2.5 Born Approximation

In order to simplify the problem of obtaining the scattered field in the forward problem, the Born Approximation can be invoked. Essentially the Born Approximation consists of assuming a simplified form of the scattered field inside the object that neglects the effects of multiple scattering between features in the background medium. This translates to assuming that the total field $\psi(\mathbf{r'}, k_0\hat{\mathbf{r}}_\mathbf{0})$ in Equations 2.12 can be approximated by the incident field $\psi_i(\mathbf{r'}, k_0\hat{\mathbf{r}}_\mathbf{0}) = e^{ik_0\hat{\mathbf{r}}_\mathbf{0}\cdot\mathbf{r}}$, so that Equation 2.12 becomes:

$$f(k_0\hat{\mathbf{r}}, k_0\hat{\mathbf{r}}_\mathbf{0}) = \int_D d^2r' e^{-ik_0(\hat{\mathbf{r}}-\hat{\mathbf{r}}_\mathbf{0})\cdot\mathbf{r}'} O(\mathbf{r}'). \tag{2.15}$$

This is the spatial Fourier transform of the Object Function calculated at the spatial frequency of $k_0(\hat{\mathbf{r}} - \hat{\mathbf{r}}_\mathbf{0})$, so the scattering amplitude now has the form:

$$f(k_0\hat{\mathbf{r}}, k_0\hat{\mathbf{r}}_\mathbf{0}) = \tilde{O}(k_0(\hat{\mathbf{r}}_\mathbf{0} - \hat{\mathbf{r}})). \tag{2.16}$$

Therefore for a single incident wave with direction $\hat{\mathbf{r}}_\mathbf{0}$ and measuring the scattered field in all possible directions $\hat{\mathbf{r}}$ as shown in Figure 2.4 (a), the object function is mapped to a circle in the spatial frequency domain with a radius k_0 centred at $k_0\hat{\mathbf{r}}_\mathbf{0}$ and intersecting the origin as shown schematically by the solid circle in Figure 2.4 (b). Using every possible incident direction $\hat{\mathbf{r}}_\mathbf{0}$, the circle sweeps around the origin of

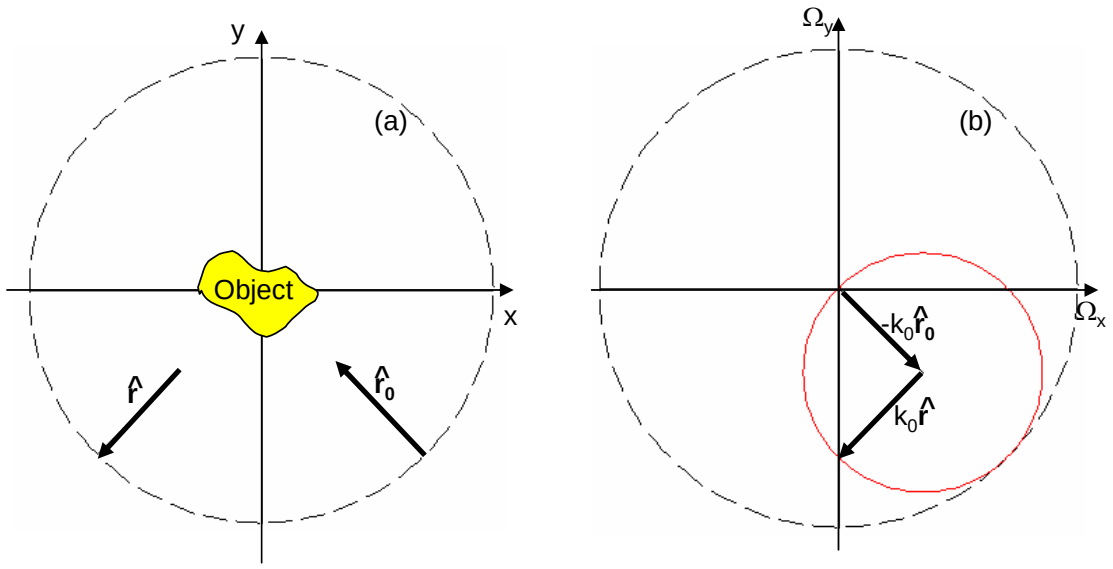

Figure 2.4: *The illumination of the object and the detection of the resulting scattered field. (a) The object is illuminated from the direction* $\hat{\mathbf{r}}_\mathbf{0}$ *and the scattered field is measured in the direction* $\hat{\mathbf{r}}$*; (b) Under the Born Approximation the scattered field measured in the direction* $\hat{\mathbf{r}}$ *from an illumination from the direction* $\hat{\mathbf{r}}_\mathbf{0}$ *is mapped to the point* $\Omega = k_0(\hat{\mathbf{r}}_\mathbf{0} - \hat{\mathbf{r}})$ *in the* $\mathbf{\Omega}$*-space.*

the $\mathbf{\Omega}$-space, describing a disk with radius $2k_0$ in the spatial frequency domain, shown by the dashed line in Figure 2.4. This is known as the Ewald limiting circle (in 3-D this becomes a limiting sphere). Consequently, under the Born Approximation the scattering amplitude provides the spatial Fourier transform of the Object function limited to a circle of radius $2k_0$ in the $\mathbf{\Omega}$-plane.

The spatial frequency $2k_0$ corresponds to a spatial harmonic of period $\lambda/2$ in the geometric domain. Therefore the characteristics of an object must be separated by more than $\lambda/2$ for them to affect the far field measurements. As a consequence, the Born Approximation provides no direct link between the spatial harmonics which correspond to the features of an object separated by less than $\lambda/2$ and the scattered field. The Born Approximation therefore limits the amount of information that is conveyed to the far field and so leads to the classical resolution limit, as will be discussed in the next chapter.

The Born Approximation can be considered to be valid if the effects of multiple

scattering are negligible, in which case the object is referred to as weakly scattering. The conditions for an object to be considered weakly scattering depend on both the contrast between the background medium and the object and the size of the object relative to the wavelength. The Born Approximation can be considered valid if the contrast is low and the object is smaller than the wavelength according to:

$$\sup_{r<r_0} |O(\mathbf{r})| < \nu \frac{\lambda}{r_0}, \tag{2.17}$$

where ν is a constant determined by the validation scheme chosen as shown in [40] and [41]. If the object is large with respect to the wavelength even if the contrast is small then the Born Approximation is no longer valid.

2.6 Multiple Scattering

In the previous section the Born Approximation gave the desired scattering amplitude in terms of the spatial Fourier transform of the object function. This section will consider the effects of multiple scattering within the object that account for the interaction of an already scattered wave with the object.

Recall the expression for the scattering amplitude but in this case consider the total wave field ψ split into its scattered and incident parts:

$$f(k_0\hat{\mathbf{r}}, k_0\hat{\mathbf{r}}_\mathbf{0}) = \int_D d^2r' e^{-ik_0\hat{\mathbf{r}}\cdot\mathbf{r}'} O(\mathbf{r}')(e^{ik_0\hat{\mathbf{r}}_\mathbf{0}\cdot\mathbf{r}} + \psi_s(\mathbf{r}', k_0\hat{\mathbf{r}}_\mathbf{0})), \tag{2.18}$$

or equivalently:

$$f(k_0\hat{\mathbf{r}}, k_0\hat{\mathbf{r}_\mathbf{0}}) = \tilde{O}(k_0(\hat{\mathbf{r}} - \hat{\mathbf{r}}_\mathbf{0})) + \int_D d^2r' e^{-ik_0\hat{\mathbf{r}}\cdot\mathbf{r}'} O(\mathbf{r}')\psi_s(\mathbf{r}', k_0\hat{\mathbf{r}}_\mathbf{0}). \tag{2.19}$$

The first term on the RHS of Equation 2.19 is the scattering amplitude given under the Born Approximation. Clearly the exact form of the scattering amplitude is

only partially described under the Born Approximation. In its current form, the significance of the integral term in Equation 2.19 is not apparent. In order to reformulate the scattering amplitude it is also necessary to introduce the transition amplitude:

$$K(\alpha\hat{\mathbf{u}}, k_0\hat{\mathbf{r}}_\mathbf{0}) = \int_D d^2r' e^{-i\alpha\hat{\mathbf{u}}\cdot\mathbf{r}'} O(\mathbf{r}')\psi(\mathbf{r}', k_0\hat{\mathbf{r}}_\mathbf{0}). \tag{2.20}$$

It should be noted that when $\alpha\hat{\mathbf{u}} = k_0\hat{\mathbf{r}}$, $K(k_0\hat{\mathbf{r}}, k_0\hat{\mathbf{r_0}}) = f(k_0\hat{\mathbf{r}}, k_0\hat{\mathbf{r_0}})$. It is also necessary to introduce the eigenfunction expansion of the Green's function as described in [42] which is given by:

$$G(\mathbf{r}, \mathbf{r}') = -\frac{1}{8\pi^3}\int_{-\infty}^{\infty} d^2\alpha \frac{e^{i\alpha\hat{\mathbf{u}}\cdot(\mathbf{r}-\mathbf{r}')}}{k_0^2 - \alpha^2 + i\epsilon}, \tag{2.21}$$

where ϵ has been introduced to avoid singularities. Thus by using the eigenfunction expansion of the Green's function and rewriting Equation 2.19 in terms of the transition amplitude the following expression is obtained after some manipulation:

$$K(k_0\hat{\mathbf{r}}, k_0\hat{\mathbf{r}}_\mathbf{0}) = \tilde{O}(k_0(\hat{\mathbf{r}}_\mathbf{0} - \hat{\mathbf{r}})) + \frac{k_0^2}{8\pi^3}\int_{-\infty}^{\infty} d^2\alpha \frac{\tilde{O}(k_0\hat{\mathbf{r}} - \alpha\hat{\mathbf{u}})K(\alpha\hat{\mathbf{u}}, k_0\hat{\mathbf{r}}_\mathbf{0})}{k_0^2 - \alpha^2 + i\epsilon}, \tag{2.22}$$

or equivalently,

$$f(k_0\hat{\mathbf{r}}, k_0\hat{\mathbf{r}}_\mathbf{0}) = \tilde{O}(k_0(\hat{\mathbf{r}}_\mathbf{0} - \hat{\mathbf{r}})) + \frac{k_0^2}{8\pi^3}\int_{-\infty}^{\infty} d^2\alpha \frac{\tilde{O}(k_0\hat{\mathbf{r}} - \alpha\hat{\mathbf{u}})f(\alpha\hat{\mathbf{u}}, k_0\hat{\mathbf{r}}_\mathbf{0})}{k_0^2 - \alpha^2 + i\epsilon}, \tag{2.23}$$

this is precisely Equation 2.19 rewritten in the $\mathbf{\Omega}$-space; this derivation follows the same method as used by Simonetti [43] in the 3-D case. As already noted, this function consists of the Born Approximated view of the scattering amplitude and an integral term. While the first term depends on the spatial frequencies of the object within the Ewald limiting circle, the latter depends on the integral of the

object function over the entire $\mathbf{\Omega}$-space. Therefore, the spatial frequencies higher than $2k_0$, relating to features of the object in geometric space separated by less than $\lambda/2$, do affect the far-field scattering amplitude. Under the Born Approximation there was a one to one mapping between the object function and the scattering amplitude. However, by considering the effects of multiple scattering the mapping is more complex.

2.7 The Far-field operator

The scattering amplitude $f(k_0\hat{\mathbf{r}}, k_0\hat{\mathbf{r}}_\mathbf{0})$ discussed in the previous sections describes how scattering of the incident wave by the object within a medium can be described either by the Born Approximation or alternatively by including the effects of multiple scattering. The scattering amplitude is the link which connects a probing wave to what is measured in the far field. In fact the scattering amplitude is the kernel of the far field $\mathbf{K}$-matrix operator $\mathbf{K}_\infty : L^2(S) \rightarrow L^2(S)$ where S is the unit circle and L^2 represents the Hilbert space, in particular:

$$\mathbf{K}_\infty|y\rangle = \int_S dS(\hat{\mathbf{r}}_\mathbf{0}) f(k_0\hat{\mathbf{r}}, k_0\hat{\mathbf{r}}_\mathbf{0}) y(k_0\hat{\mathbf{r}}_\mathbf{0}). \tag{2.24}$$

The far-field operator maps the angular spectrum of an incident plane wave, the amplitude of which is given by $y(\hat{\mathbf{r}})$, to the far field. The far-field operator $\mathbf{K}_\infty$ is linked to the well established scattering matrix as defined in quantum mechanics by the following relationship:

$$\mathbf{S} = \mathbf{I} + \frac{ik_0}{2\pi}\mathbf{K}_\infty. \tag{2.25}$$

It is known (see for example [44], [45] and [42]) that in the absence of internal absorption and due to energy conservation, the matrix $\mathbf{S}$ is normal ($\mathbf{S}^\dagger\mathbf{S} = \mathbf{S}\mathbf{S}^\dagger$ where $\mathbf{S}^\dagger$ is the adjoint of $\mathbf{S}$); this implies that the far-field operator $\mathbf{K}_\infty$ is also

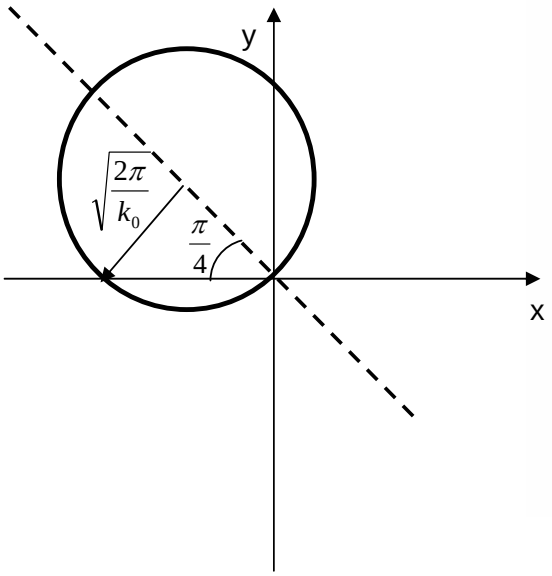

Figure 2.5: *As the far-field operator is compact it has a countable number of eigenvalues which accumulate at zero and on a circle with radius* $\sqrt{\frac{2\pi}{k_0}}$ *which intersects the origin and is centred on the line* $x = -iy$ *with* $y \geq 0$.

normal. It can also be shown that $\mathbf{K}_\infty$ is compact (as described in [46]) meaning that it has a countable number of eigenvalues which accumulate at zero. It has also been shown that the eigenvalues of the far-field operator lie on a circle in the complex plane with radius $\sqrt{\frac{2\pi}{k_0}}$ which passes through the origin and is centred on the line $x = -iy$ with $y \geq 0$ as shown in Figure 2.5. The eigenvalues $\{\mu_j\}$ and eigenfunctions $|v_j\rangle$ form an orthonormal basis for $L^2(S)$:

$$\mathbf{K}_\infty |v_j\rangle = \mu_j |v_j\rangle, \tag{2.26}$$

which due to its normality:

$$\mathbf{K}_\infty^\dagger \mathbf{K}_\infty |v_j\rangle = |\mu_j|^2 |v_j\rangle. \tag{2.27}$$

The far-field operator or equivalently its eigenvalues and eigenfunctions completely characterize the far-field pattern of a scattered field. However, if the far-field oper-

ator is not normal as is the case when absorbtion cannot be neglected [46], then a singular system $\{\mu_j, |v_j\rangle, |\vartheta_j\rangle\}$ is used to characterize the far field pattern:

$$\mathbf{K}_\infty |v_j\rangle = \mu_j |\vartheta_j\rangle, \tag{2.28}$$

$$\mathbf{K}_\infty^\dagger |\vartheta_j\rangle = \mu_j |v_j\rangle, \tag{2.29}$$

so that

$$\mathbf{K}_\infty^\dagger \mathbf{K}_\infty |v_j\rangle = |\mu_j|^2 |v_j\rangle, \tag{2.30}$$

and

$$\mathbf{K}_\infty^\dagger \mathbf{K}_\infty |\vartheta_j\rangle = |\mu_j|^2 |\vartheta_j\rangle, \tag{2.31}$$

The decomposition of the far-field operator will be useful when deriving the non-linear inverse methods to determine the object from the scattered field; this will be discussed in following chapters. It should be noted that the quantity $\mathbf{K}_\infty^\dagger \mathbf{K}_\infty$ is the Time Reversal operator $\mathbf{T}_\infty$ as introduced by Prada et all. [47]

If the Born approximation is taken in order to determine the scattered field, energy conservation laws no longer hold [38] so the far field operator is no longer normal, meaning that the eigenvalues of the far-field operator will no longer lie on a circle but will lie across the the entire complex plane. The eigenvalues of the far-field operator are also affected if the object is absorbing (such as in medical imaging). In this case the eigenvalues are contained within a circle which passes through the origin, the radius of which is based upon the absorption of the object and its geometry. This circle is in general smaller than the equivalent non-absorbing case as shown by Colton and Kress [46].

2.8 Summary

This chapter has outlined the forward scattering problem. The basic ideas and parameters involved in describing the scattering problem have been discussed and relevant relationships explained. The representation of the Helmholtz equation in integral format as the Lippmann Schwinger equation not only highlighted that the Born Approximation does not provide a link between the higher spatial frequencies of an object and the scattered field, but also that by considering the effects of multiple scattering, information on the higher spatial frequencies becomes available in the far field.

Chapter 3

Inverse Scattering

In the inverse scattering problem, the incident field is known, the scattered field has been measured but the object function is unknown. The problem therefore is to determine the object function from the measured scattered field and the known incident field plus any a priori knowledge that may be known about the nature of the object (such as its boundary conditions, size or composition). Reconstruction of the object function produces an image which represents the properties of the object, so the inverse scattering problem can be thought of as being able to build an image of the object from the scattered field. Recovering the object function is however an ill-posed non-linear problem. An alternative approach is to reconstruct just the shape of the object D from the measured scattered field. Reconstructing D simplifies the inverse problem and in many applications provides more than adequate information on the object.

This chapter will explore the challenges associated with solving the inverse scattering problem and consider methods for dealing with them. The inverse scattering problem is ill posed meaning that the solution violates at least one of the conditions of existence, uniqueness and stability outlined by Hadamard. Subsequent sections will define each of these conditions and the reasons why the inverse problem is ill posed will be examined. Methods for dealing with the ill-posed nature of the equation, known as regularization techniques, will also be outlined. Following the

discussion on the ill-posed nature of the problem, three fundamental approaches for dealing with this non-linear inverse problem will be discussed; these are: iterative methods, point source methods and linear sampling methods. Of these methods, linear sampling, which attempts to reconstruct the support of the object function from the measured data, will be the main focus of the imaging methods in this thesis. The Factorization method, which is a type of linear sampling method, will be discussed. Finally the Born Approximation, which effectively linearises the inverse scattering problem, will be examined; the consequences of this linearisation will then be discussed.

3.1 Ill-posed and Well-posed problems

In 1923 Jacques Salomon Hadamard proposed three criteria which would determine if a problem was well or ill posed, these were: existence, uniqueness and stability; see for example [39]. Put in a mathematical framework, if $x \in \mathbf{X}$ and $y \in \mathbf{Y}$ where $\mathbf{X}$ and $\mathbf{Y}$ are compact spaces and let $\mathbf{F}$ be an operator (which may be linear or non-linear) such that $\mathbf{F} : \mathbf{X} \to \mathbf{Y}$ then the equation $\mathbf{F}(x) = y$ is well posed if it satisfies:

1. Existence: for every $y \in \mathbf{Y}$ $\exists$ $x \in \mathbf{X}$ such that $\mathbf{F}(x) = y$.
2. Uniqueness: for every $y \in \mathbf{Y}$ there is at most one $x \in \mathbf{X}$ with $\mathbf{F}(x) = y$.
3. Stability: x depends continuously on y, so that for any sequence $x_n \subset \mathbf{X}$ with $\mathbf{F}(x_n) \to \mathbf{F}(x)$ as $n \to \infty$ then $x_n \to x$ as $n \to \infty$.

If all of these criteria are met then the problem is considered to be well posed, otherwise it is considered to be ill posed. Initially it was believed that only problems that were well posed were of physical interest and that although ill-posed problems were of academic interest they could not be applied to physical systems. As such the field of ill-posed problems was somewhat neglected. It became apparent however that although the inverse scattering problem was ill posed, it was of significant physical

interest in the field of imaging. The next two sections will explore Hadamard's criteria with respect to the inverse scattering problem.

3.2 Uniqueness

In terms of the inverse scattering problem, uniqueness translates to determining the conditions under which the measured scattered field uniquely determines the object function (or equivalently the index of refraction). Due to the importance of the inverse scattering problem, much work has been done on determining these conditions. It has been shown that the index of refraction $n(\mathbf{r})$ can be uniquely determined from the measured scattered field if the object is illuminated and the scattered field is measured, from every possible direction. If the measured scattered field uniquely determines the object function then unlimited resolution will have been achieved as the reconstructed image will represent the object exactly. However, the resolution of the reconstructed $n(\mathbf{r})$ from experimental measurements is limited due to noise. A related problem to the reconstruction of $n(\mathbf{r})$ is the reconstruction of the support (or shape) of the object function D; this approach provides information on the size, shape and location of the object which is often all of the information that is required about the object. However, even if only the support of the object is to be reconstructed from the scattered field, the problem of uniqueness still needs to be addressed; in this case it needs to be determined if the scattered field uniquely determines the support of the object.

The earliest work on uniqueness for the inverse scattering problem was carried out by Rellich [48] and Schiffer [49], who determined that the far-field data uniquely determines the support D of the object $O(\mathbf{r})$ under the condition that $\psi = 0$ on the boundary (Dirichlet boundary conditions). This result has subsequently been generalised (Kirsch and Kress [50]) so that it is not necessary to know the boundary conditions to determine uniqueness. The proof of this result can be found for example in [51], [50] and [52], where it is shown that if the scattered field from two objects with support D_1 and D_2 coincide for all illumination and detection directions then

$D_1 = D_2$.

The above result guarantees the uniqueness of a solution to the inverse scattering problem in the ideal case when illumination and detection can be performed for every possible direction. However experimentally this is not practical, instead illumination of the object and detection of any scattered fields will take place over a finite number of directions. In an attempt to cope with the reduced amount of information on which to find a solution, Potthast [53] and [52] introduced the idea of ϵ-uniqueness, which is less restrictive than classical uniqueness. In this case for every $\epsilon > 0$ there exists a finite number of illumination directions which will uniquely determine the support of the object up to an error of ϵ in the difference in the Hausdorff distance of the solutions (where the Hausdorff distance is a way of working out the difference between two functions). So for any $\epsilon > 0$ there exists an integer N such that if the far-field measurements obtained from the illumination of two objects $O_1(\mathbf{r})$ and $O_2(\mathbf{r})$ coincide for all N then $d(D_1, D_2) < \epsilon$ where $d(.,.)$ denotes the Hausdorff distance and D_1 and D_2 are the support of O_1 and O_2 respectively. As $\epsilon \to 0$ this is equivalent to illuminating the object from every possible direction which corresponds to $N \to \infty$ and so the arguments for uniqueness given above can be used. Experimentally the support of the object function can be determined within a given error so long as the object is illuminated from enough directions. This result is significant when dealing with linear or partial view arrays when the object is not enclosed by the array, in which case the support of the object can be determined from the scattered field within a given error so long as there are enough elements within the array. As the number of elements $N \to \infty$ then the error $\epsilon \to 0$ so that the support would be completely determined.

In summary the uniqueness of the support of the object function can be guaranteed if illumination and detection take place for every possible direction. In practise however the illumination and detection will take place for a finite number of directions which means the support will satisfy ϵ-uniqueness for some $\epsilon > 0$. Having discussed the conditions for uniqueness, the next section will look at Hadamard's other criteria and introduce the idea of regularization.

3.3 Existence, Instability and Regularization

This section will examine the existence and stability of the inverse scattering problem which will lead naturally onto the topic of regularization which is the process by which unstable problems can be stabilized. In order to deal with the issues of existence and instability a linear inverse problem will be examined, as the methods that will be considered in this thesis in order to solve the inverse scattering problem will linearize the problem in some way. Consider the inverse problem of $\mathbf{F}x = y$ where the operator $\mathbf{F}$ is linear and compact. In this case the conditions of existence of the solution can be determined by considering Picard's theorem. If the eigenvalues of the compact operator $\mathbf{F}$ are given by μ_n $(n = \{1, 2, ...\})$, then there exists orthonormal sequences $|x_n\rangle \in \mathbf{X}$ and $|y_n\rangle \in \mathbf{Y}$ such that:

$$\mathbf{F}|x_n\rangle = \mu_n|y_n\rangle, \tag{3.1}$$

and

$$\mathbf{F}^\dagger|y_n\rangle = \mu_n|x_n\rangle, \tag{3.2}$$

where $\mathbf{F}^\dagger$ represents the adjoint of $\mathbf{F}$. In this case, $(\mu_n, |x_n\rangle, |y_n\rangle)$ is said to be a singular system for $\mathbf{F}$.

Picard's theorem states that for a compact linear operator $\mathbf{F} : \mathbf{X} \to \mathbf{Y}$ with a singular system $(\mu_n, |x_n\rangle, |y_n\rangle)$, then the equation $\mathbf{F}x = y$ is solvable if it satisfies:

$$\sum_{n=1}^{\infty} \frac{1}{|\mu_n|} |\langle y|y_n\rangle|^2 < \infty. \tag{3.3}$$

In this case the solution is given by:

$$|x\rangle = \sum_{n=1}^{\infty} \frac{1}{\mu_n} \langle y|y_n\rangle |x_n\rangle. \tag{3.4}$$

The proof of this theorem can be found in the monograph by Colton and Kress [39]. Picard's theorem gives the conditions for the existence of the solution; it can also be used to highlight the instability of the inverse problem for a compact operator. In order to test the stability of the problem consider a perturbation δy to the measured data given by $y^\delta = y + \delta y$. Then the solution given by Picard's theorem is:

$$|x^\delta\rangle = |x\rangle + \sum_{n=1}^{\infty} \frac{1}{\mu_n} \langle \delta y|y_n\rangle |x_n\rangle. \tag{3.5}$$

The summation term in the perturbed solution x^δ represents the error. Even when the perturbation to the measured data δy is small the summation becomes unbounded due to the eigenvalues μ_n accumulating at zero which is a consequence of the operator $\mathbf{F}$ being compact. As the error becomes unbounded the inverse problem can be considered to be unstable.

Another consequence of the compact nature of the operator $\mathbf{F}$ is that the inverse operator $\mathbf{F^{-1}}$ is unbounded. Regularization techniques aim to construct a bounded operator $\mathbf{G}_\xi$ known as a regularization strategy which provides a stable approximation to $\mathbf{F^{-1}}$ with regularization parameter $\xi > 0$, so that the following limit is satisfied:

$$\lim_{\xi \to 0} \mathbf{G}_\xi(\mathbf{F}x) = x, \tag{3.6}$$

for all $x \in \mathbf{X}$. Applying the bounded operator $\mathbf{G}_\xi$ to the known data y will provide an approximation x_ξ of the solution to the inverse problem x. The accuracy of the approximation depends upon the regularization strategy that is chosen and any errors that are present in the measured data.

For example, the Tikhonov regularization strategy gives an approximate solution to the inverse problem by letting:

$$\mathbf{G}_\xi = (\xi\mathbf{I} + \mathbf{F}^\dagger\mathbf{F})^{-1}\mathbf{F}^\dagger, \tag{3.7}$$

and hence:

$$x_\xi = (\xi\mathbf{I} + \mathbf{F}^\dagger\mathbf{F})^{-1}\mathbf{F}^\dagger(y), \tag{3.8}$$

where the parameter ξ is chosen based upon the error $\delta y = |y^\delta - y|$ in the measured data. If the errors affect the operator as opposed to the measured data, then the above is often referred to as the Tikhonov-Morozov regularization.

An alternative form of regularization which can be applied to the solution given by Picard's theorem 3.4 is to limit the number of terms taken in the summation so that the solution would be given by:

$$x_\xi = \sum_{n=1}^{\xi} \frac{1}{\mu_n} |\langle y|y_n\rangle| x_n, \tag{3.9}$$

where it is assumed that the eigenvalues μ_n are placed in order of decreasing magnitude. In this case the regularization chooses the upper bound for the above summation. This approach is known as the spectral cut off method of regularization.

Having discussed the ill-posed nature of the inverse scattering problem, its non-linearity will be discussed in the next section. Three approaches to solving this non-linear problem will be outlined.

3.4 Non-Linear Inverse Techniques

The general inverse scattering problem is non-linear. This can be shown by considering two distinct objects $O_1(\mathbf{r})$ and $O_2(\mathbf{r})$ which produce two different far-field patterns $\mathbf{K_{\infty 1}}$ and $\mathbf{K_{\infty 2}}$ when illuminated independently. On the other hand the far-field pattern produced by the object $O_1(\mathbf{r}) + O_2(\mathbf{r})$ will not be given by $\mathbf{K_{\infty 1}} + \mathbf{K_{\infty 2}}$ due to the effects of multiple scattering. This argument shows that the forward scattering problem is non-linear with respect to the object function. This implies that the inverse scattering problem is also non-linear with respect to the object function. There are essentially three approaches to solving the non-linear inverse scattering problem as discussed by Luke and Potthast in [54] and [52], these are: iterative methods, point source methods and linear sampling methods.

In the case of iterative methods the measured scattered field is used to construct an approximate solution to the inverse scattering problem. The resulting scattered field from using the approximate solution in a forward scattering problem is then derived and compared to the measured scattered field and the results of this comparison are used to modify the approximation. This process is iterated until the calculated scattered field converges to the measured scattered field within a predetermined error. This approach can be combined with the Born Approximation (that will be discussed later in this chapter) in order to build the initial approximation. In this case this method is referred to as the Distorted Born Iterative Method. This has been shown to achieve super resolution experimentally, see for example the work done by Chen and Chew [55]. Although this is a powerful method of determining the object function from the scattered field, it should be noted that it is computationally expensive due to the number of calculations required to determine the solutions to each of the required forward scattering problems.

Another approach to solving the inverse scattering problem which has received interest from authors such as Potthast, Colton, Monk, Kirsch and Kress are point source methods. In this case the problem is split into finding the solution to the ill-posed problem of determining the scattered field from the measured far-field data

and the well-posed problem of determining the shape of the scatterer based upon an assumption about its boundary conditions. The disadvantage of this method is that prior knowledge about the properties of the object is required, which in many cases may not be available, for this reason, these methods will not be considered in this thesis.

The final approach to solving the non-linear inverse scattering problem is that of linear sampling, in which case no assumptions are made about the physical properties of the object or its boundaries. In contrast with the iterative methods, this approach does not reconstruct the object function but provides an image of the shape of the object. The main advantage of this class of methods is that the non-linear inverse problem is replaced by a linear integral problem. These methods will provide a powerful tool to investigate the effects of multiple scattering on the far-field operator. For this reason these methods will be considered in the rest of this thesis.

3.5 The Factorization Method

The Linear Sampling Method as defined by Colton [56] is a way of reconstructing the boundary of an object from the far-field operator, if the far-field operator is defined as in the previous chapter as:

$$\mathbf{K}_\infty|y\rangle = \int_S dS(\hat{\mathbf{r}}_\mathbf{0}) f(k_0\hat{\mathbf{r}}, k_0\hat{\mathbf{r}}_\mathbf{0}) y(k_0\hat{\mathbf{r}}_\mathbf{0}). \tag{3.10}$$

Then the Linear sampling method (LSM) considers the following equation:

$$\mathbf{K}_\infty|y\rangle = |g_\infty(\hat{\mathbf{r}}, \mathbf{z})\rangle, \tag{3.11}$$

where $g_\infty(\hat{\mathbf{r}}, \mathbf{z}) = e^{-ik_0\hat{\mathbf{r}}\cdot\mathbf{z}}$ is proportional to the far-field pattern of a source at a point $\mathbf{z}$ in the direction $\hat{\mathbf{r}}$ and is known as the steering function. It is assumed that for

every $\epsilon > 0$ there exists a function $y = y(\cdot, \mathbf{z}) \in L^2(S)$ such that $\|\mathbf{K}_\infty y - g_\infty\| < \epsilon$, $\|y(\cdot, \mathbf{z})\|$ becomes unbounded as $\mathbf{z}$ tends to the boundary ∂D of the support D of the object function. The linear equation produced under the linear sampling method can then be applied to the Tikhonov-Morozov regularization in order determine $|y\rangle$.

The linear sampling method was modified by Kirsch [57] who proposed the Factorization method (FM) which considers the equation:

$$(\mathbf{K}_\infty^\dagger \mathbf{K}_\infty)^{\frac{1}{4}} |y\rangle = |g_\infty(\hat{\mathbf{r}}, \mathbf{z})\rangle, \tag{3.12}$$

where $\mathbf{K}_\infty^\dagger \mathbf{K}_\infty$ is the time reversal operator $\mathbf{T}_\infty$ as described by Prada [47]. It was shown by Kirsch that a solution to Equation 3.12 exists if and only if point $\mathbf{z}$ belongs to D so long as $\mathbf{K}_\infty$ is normal. Picard's theorem implies that Equation 3.12 is solvable if and only if:

$$\sum_{j=1}^{\infty} \frac{1}{|\mu_j|} |\langle g_\infty(\hat{\mathbf{r}}, \mathbf{z}) | v_j \rangle|^2 < \infty, \tag{3.13}$$

where v_j are the eigenfunctions of $\mathbf{K}_\infty$. The function, $g_\infty(\hat{\mathbf{r}}, \mathbf{z})$, is used to probe the grid of coordinates that make up the region of interest which it is assumed contains the object as shown in Figure 3.1. Equation 3.13 sweeps the steering function $g_\infty(\hat{\mathbf{r}}, \mathbf{z})$ over each point $\mathbf{z}$. Equation 3.13 will be bounded if $\mathbf{z} \in D$ but will become unbounded otherwise. The Factorization method scans the region of interest using the following expression:

$$FM(\mathbf{z}) = \frac{1}{\sum_{j=1}^{\infty} \frac{1}{|\mu_j|} |\langle g_\infty(\hat{\mathbf{r}}, \mathbf{z}) | v_j \rangle|^2}. \tag{3.14}$$

The region of interest is defined by a grid of coordinates, and the Factorization method applies Equation 3.14 to each of these coordinates. If Equation 3.14 is applied to a coordinate $\mathbf{z}$ which is not part of the support D then the result will be

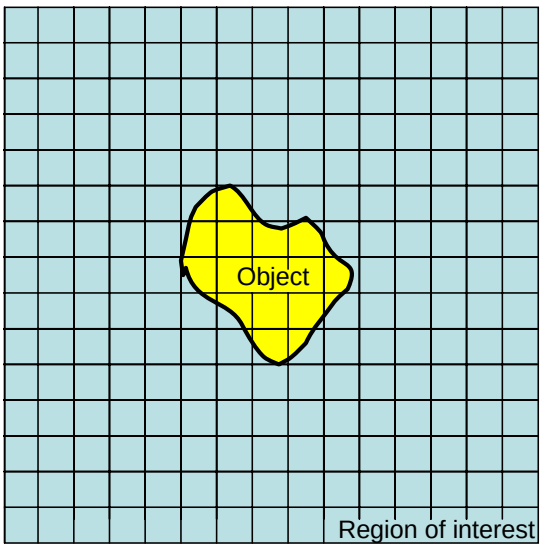

Figure 3.1: *The region of interest is characterized by a grid of points, and the steering function is used to probe each of the coordinates. If the coordinates are not on the boundary of the object then Equation 3.14 will be zero but if the coordinates correspond to a point on the boundary of the object function and Equation 3.14 will be non-zero.*

zero, however if $\mathbf{z}$ is part of D then the expression will be non-zero. By applying Equation 3.14 to each of the points in the region of interest, the object will be represented by those points where Equation 3.14 are non-zero. In the absence of noise this method can achieve unlimited resolution and has been shown to achieve super resolution experimentally, for example see [43].

3.6 The Inverse Scattering Problem under the Born Approximation

From previous discussion in this chapter, it is known that the inverse scattering problem is non-linear due to the effects of multiple scattering. In the previous chapter the Born Approximation was introduced to investigate the forward scattering problem, this approach neglects the effects of multiple scattering implying that the forward scattering problem becomes linear and as a consequence the inverse problem is also linear with respect to the object function. The benefits and consequences of

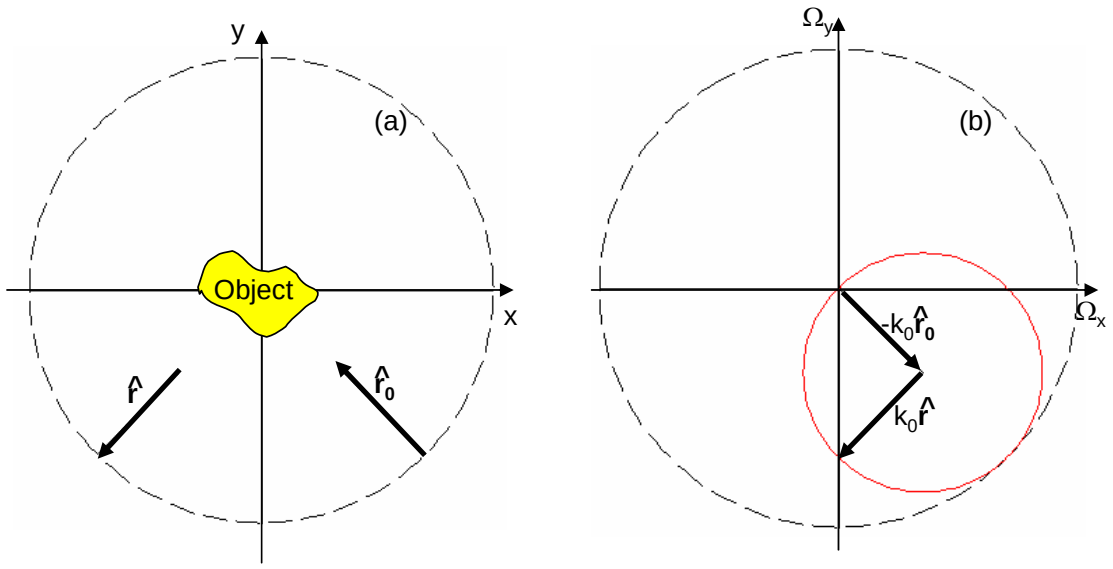

Figure 3.2: *The illumination of the object and the detection of the resulting scattered field. (a) The object is illuminated from the direction* $\hat{\mathbf{r}}_\mathbf{0}$ *and the scattered field is measured in the direction* $\hat{\mathbf{r}}$*; (b) Under the Born Approximation the scattered field measured in the direction* $\hat{\mathbf{r}}$ *from an illumination from the direction* $\hat{\mathbf{r}}_\mathbf{0}$ *is mapped to the point* $\Omega = k_0(\hat{\mathbf{r}}_\mathbf{0} - \hat{\mathbf{r}})$ *in the* $\mathbf{\Omega}$*-space.*

this assumption will be discussed in this section.

It was shown in the previous chapter for the forward scattering problem that the Born Approximation resulted in a one-to-one correspondence between the scattering amplitude and the spatial Fourier transform of the object function that was limited to an Ewald limiting disc of radius $2k_0$ shown in Figure 3.2. Equivalently the spatial periodicities of the object which are separated by less than $\lambda/2$ have no effect on the far-field operator in the forward scattering problem under the Born Approximation.

If the inverse scattering problem assumes the Born Approximation then the problem is to determine the object function from the measurements of the scattered field that provide the spatial frequencies within the Ewald limiting disc. The object function contains information outside of the Ewald limiting disc; this information is not accounted for under the Born Approximated model and as such must be dealt with. One possibility is to set the information outside the Ewald limiting disc to zero so that:

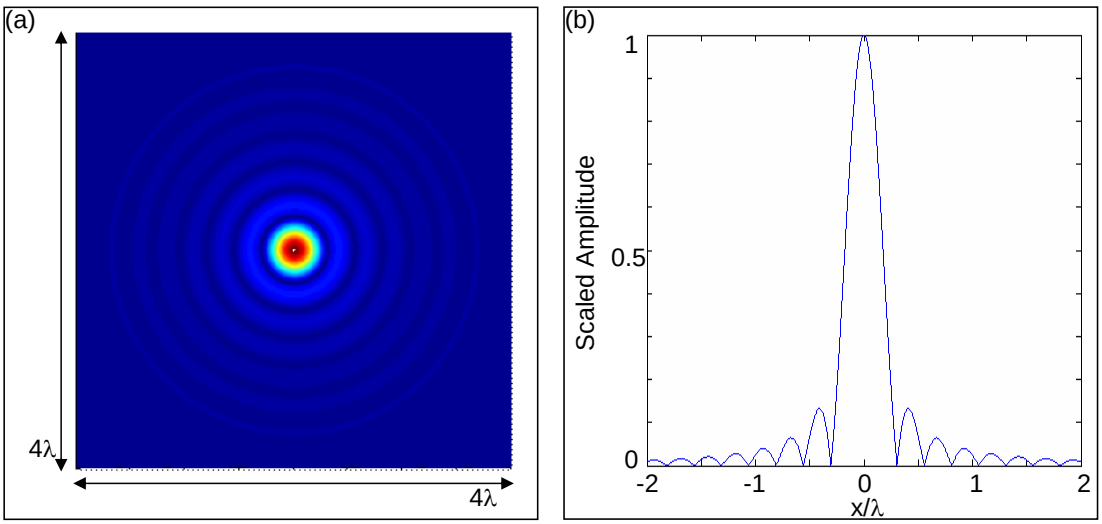

Figure 3.3: *Point spread function of the Born Approximation (a) Surface plot of the point spread function, (b) Cross section of the point spread function.*

$$\tilde{O}_{BA}(\mathbf{\Omega}) = \tilde{H}(\mathbf{\Omega})\tilde{O}(\mathbf{\Omega}), \tag{3.15}$$

where $\tilde{O}_{BA}$ is the Born Approximation of the object function $\tilde{O}$ in the frequency domain and $\tilde{H}$ is a low pass filter such that $\tilde{H}(\mathbf{\Omega}) = 1$ for $|\mathbf{\Omega}| \leq 2k_0$ and is zero otherwise. Equation 3.15 means that the function $\tilde{O}_{BA}(\mathbf{\Omega})$ is defined over the entire $\mathbf{\Omega}$-space, and as such the inverse Fourier transform of this function can be taken to obtain the Born Approximated image of the object function in the geometric space:

$$O_{BA}(\mathbf{r}) = \int_D d^2r' H(\mathbf{r} - \mathbf{r}')O(\mathbf{r}'). \tag{3.16}$$

The image of the object function given under the Born Approximation is a low pass filtered version of the actual object function without the spatial frequencies shorter than $\lambda/2$. This is represented in Equation 3.16 as the convolution of the actual object function with the point spread function H:

$$H(\mathbf{r}) = k_0 \frac{J_1(2k_0|\mathbf{r}|)}{\pi|\mathbf{r}|}, \tag{3.17}$$

where J_1 is the Bessel function of order one of the first kind, and the point spread function is shown in Figure 3.3.

The measured data under the Born Approximation is regularized by setting it to zero outside the Ewald limiting disc in the $\mathbf{\Omega}$-space. This regularization may appear to violate the uniqueness of the solution to the inverse scattering problem, as two object functions with the same representation in the Ewald limiting disc but different elsewhere in the $\mathbf{\Omega}$-space, would result in identical reconstructed images under the Born Approximation. However, $\tilde{O}(\mathbf{\Omega})$ is an analytic function, meaning that it can be determined over the entire $\mathbf{\Omega}$-space from knowledge over an arbitrarily small area. This implies that knowledge of the object function in the Ewald limiting disc uniquely determines the object function. Analytic continuation can be used to extrapolate the object function determined under the Born Approximation to points outside of the Ewald limiting disc; taking the inverse Fourier Transform of this data would lead to the exact object function being obtained (instead of the low pass filtered version) and unlimited resolution being achieved. However, it has been observed by several authors ([58], [59], [60], [43], [61] and [62]) that analytic continuation is not stable to noise and so does not provide a stable solution to the inverse scattering problem.

Another potential way of achieving super resolution under the Born Approximation, is to include information on the properties of the object. Information about the size, shape or material properties of the object combined with the regularized data can lead to super resolution being achieved. However in many applications this information is not known beforehand so this cannot be considered to be a feasible approach.

3.7 Summary

This chapter has provided an overview of the inverse scattering problem. The ill-posedness of the problem has been discussed and the conditions for a solution to exist have been outlined along with the issue of guaranteeing uniqueness. The instability

of the inverse scattering problem has been highlighted. The idea of regularization in order to deal with the ill-posed nature of the inverse scattering problem has also been introduced. Three strategies of solving the inverse scattering problem were then discussed; these were: iterative methods, point source methods and linear sampling methods, the latter of which will be used in this thesis to demonstrate the benefits of accounting for the effects of multiple scattering when building an image from the measured scattered field. A type of linear sampling method known as the Factorization method has been explored. In the absence of noise this method can provide unlimited resolution and has been shown to provide super resolution in experimental conditions. The Born Approximation has also been discussed; this transforms the non-linear problem into a linear problem which provides a one-to-one mapping between the object function and the measured scattered field. However it has been shown that the Born Approximation only provides a low pass filtered version of the object, that removes spatial periodicities shorter than $\lambda/2$. The next chapter will discuss how the far-field operator is measured experimentally by an array of discrete points and how the continuous case that has been considered thus far can be adapted to this discrete situation.

Chapter 4

Sampling of the far-field operator

4.1 Introduction

The illumination of an object by an incident wave and detection of any resulting scattered waves has thus far been considered in an idealised scenario, where detection and illumination can be carried out for every possible direction for a continuous time period. Experimentally the illumination of the object and detection of any subsequent scattered fields will be carried out at a discrete number of points dictated by the physical locations of the sensors. The next section will discuss the discrete sampling problem. A section on array technology will follow, which will discuss the basics of array technology as well as applications and some recent advances. The architecture of a general array system will then be discussed; this will detail the components required to generate incident fields and record any scattered fields experimentally. Finally, the discrete version of the far-field operator will be discussed and the effect this has on the Factorization Method that was discussed in the previous chapter will be explored.

4.2 The Sampling Problem

In the preceding chapters the governing equations of the scattering problem and the far-field operator were derived under a continuous framework. Physically this meant that the object could be illuminated from every possible direction and the resulting scattered field could be recorded from every possible direction continuously in time. Experimentally this is not possible either temporally or spatially.

Experimentally the system is illuminated from a discrete number of points which make up an array, and the resulting scattered field is recorded at a discrete number of points which also form the elements of an array. The illumination and detection arrays can be disjoint, however this thesis will only consider coincident arrays where each illumination point is also a detection point. The scattered field recorded at the array elements in the form of a temporal signal will also be sampled in a discrete fashion for a given time step.

The sampling problem is to determine the required sampling interval (both temporally and spatially) so that all of the information contained within the scattered field can be retrieved successfully. If the sampling interval is too large, information contained within the scattered field will be lost and reconstructions of the object based upon this data will suffer from artifacts. However, if the sampling interval is too small then redundant information will be recorded resulting in unnecessary hardware complexity.

It is known that in order to sample a time dependent signal effectively, the sampling frequency needs to be at least twice the maximum frequency f^M contained in the signal; this implies that the sampling interval Δt is given by:

$$\Delta t \leq \frac{1}{2f^M}, \tag{4.1}$$

this is known as the Nyquist or Shannon criterion as shown in [63]. Failure to meet the Shannon criterion leads to the phenomenon known as aliasing which will cause

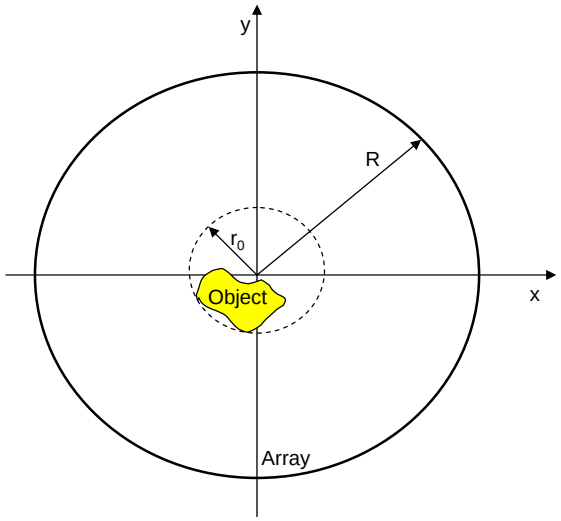

Figure 4.1: *Schematic of a full view array with a radius of R. The object is circumscribed by a circle of radius r_0.*

artifacts when analyzing the spectrum of the signal.

In a similar fashion to the temporal case, the distance between the spatial sampling points of a monochromatic wavefield are governed by criterion that if followed correctly will prevent the undersampling of the scattered field. Consider first of all the case of a full view or circular array. Simonetti et al. [64] showed that to avoid undersampling, the sampling distance Δr is given by:

$$\Delta r \leq \frac{\lambda R}{2r_0}, \tag{4.2}$$

where R is the radius of the array and r_0 is the characteristic size of the object which corresponds to the radius of a circle which is centred on the origin and circumscribes the object, as shown in Figure 4.1. Allowing the characteristic size of the object $r_0 \to R$ physically represents the case of a linear array giving the separation distance:

$$\Delta r \leq \frac{\lambda}{2}. \tag{4.3}$$

As in the temporal case, spatial undersampling can lead to artifacts known as grating lobes in the reconstructed image.

If an object is to be illuminated by an incident field of a known frequency and wavelength, then by using the sampling criterion an array can be designed to correctly measure the far-field operator. The available array technologies will be discussed in the next section.

4.3 Array Technology

In principle, a single transmitter and receiver pair can be used to measure the far-field operator by scanning them across a predetermined set of coordinates in order to illuminate the object from a variety of directions and to detect the scattered field from a number of directions. Providing the spatial sampling criterion is met for the distance between the different transmit and receive locations, such mechanical scanning can construct a valid far-field operator. The major disadvantage of mechanical scanning is the time that it takes to collect all the information. Having to manoeuver the elements in this way means that this method of collecting the data can be a lengthy process depending on the number of transmit and receive locations and the speed at which the elements can be moved. In many applications the properties of the object may not be constant in time, however it may be possible to define a time period t_c over which these properties can be considered constant. In order to construct a valid far-field operator all of the required measurements must be completed in a time period shorter than t_c. It is often unfeasible for mechanical scanning to complete all of the measurements in the time period t_c. For example imaging of the human heart requires all measurements to completed whilst the heart is at rest; if the average resting heart rate is approximately $60-100$ beats per minute then measurements must be made between heartbeats, in which case mechanical scanning is not practical and so another approach must be employed.

Advances in the fields of micro-machining, telecommunications and solid state electronics, has allowed an explosion in the development of array technology, meaning that arrays with thousands of elements can be constructed which can collect all of the required information on the scattered field in a fraction of a second. These ar-

rays consist of N transducers in a fixed configuration, and each element is capable of both transmission and detection. The elements are used in sequence to illuminate the object, and the resulting scattered field is then detected by all of the elements. This process continues until all N of the transducers has been used to illuminate the object. As all N of the elements can be used to measure the scattered field in parallel, this means that the system only needs to be illuminated N times in order to obtain the $N \times N$ required measurements. The electronic switching between different transmitters is much faster than the mechanical movement of the transmitter in mechanical scanning. Ultimately the speed at which measurements can be performed is limited by the velocity c_0 (m/s) of the waves in the medium. Therefore, even with an ideal array that can switch instantaneously between array elements, the measurement time will depend on the longest path from the transmitter to the receiver d_A, leading to a required time of Nd_A/c_0 seconds in order for all of the measurements to be taken, where N is the number of illuminating array elements.

Linear or partial view arrays are used when it is not possible to completely enclose the object. In this case the far-field operator will not contain information on the total scattered field. Partial view arrays are currently used in state-of-the-art technology in the fields of medical diagnosis, non-destructive testing, radio astronomy and geophysical mapping. Linear arrays can come in many different sizes and configurations depending upon the specific application and the wavelength of the signal that is being used. For example, hand held linear arrays used in medical ultrasound contain hundreds of elements, whereas the Very Long Baseline Array (VLBA) used in radio astronomy consists of 10 elements spread from Hawaii to the Virgin islands, each element is a 240 ton 25m diameter dish antenna. The reason for such large differences in size is related to the spatial sampling criterion such that for a linear array the elements must have a maximum separation distance of $\lambda/2$. So a system with a large wavelength such as radio astronomy can have a much greater distance between its elements than a medical ultrasound probe which uses a wavelength of $\sim 1mm$ or less.

The discussion thus far has dealt with illumination of the object via a plane wave

traveling in the direction $\hat{\mathbf{r}}_\mathbf{0}$. If the array is in the far field of the object it can be assumed that the wave generated at a point can be treated as planar in the vicinity of the object. However, using an array of transducers allows the possibility of illuminating the object from different directions at the same time by firing the transducers simultaneously. More importantly if the elements are fired with suitable phase delays, the incident wavefields produce a beam focused on a specific point in the background medium; this is known as phased array technology. Phased arrays are state-of-the-art technology which are used in many inspection systems to focus energy on specific points within a specimen; the resulting scattered field can then be interpreted to determine the properties of the object at that point. However, phased arrays are constrained by the Rayleigh limit; as such this thesis will not focus on phased array technology.

As a final note on array technology, consider the next generation of toroidal or circular arrays. These arrays provide the ideal configuration to measure the far-field operator in 2-D. These full view arrays enclose the object, which is then illuminated from every direction by a wave-field being generated at each element in turn directed towards the centre of the array; the scattered field resulting from interaction with the object is also measured in every possible direction as shown for example in [65], [66] and [67]. An example of this new generation of toroidal arrays as discussed by Duric et al. [66] and Simonetti et al. [68], contains 256 array elements. All of the 256×256 send receive combinations possible using this array can be measured in less than 0.1 seconds, meaning that these arrays could provide a fast and efficient means of interrogating systems that are not at rest.

4.4 Architecture of an Array System

This section will consider the components of the array system consisting of N transducers that will be used to generate the incident field and record any resulting scattered field, shown schematically in Figure 4.2. The description given is applicable to both partial view and full view arrays. An input signal is generated on a

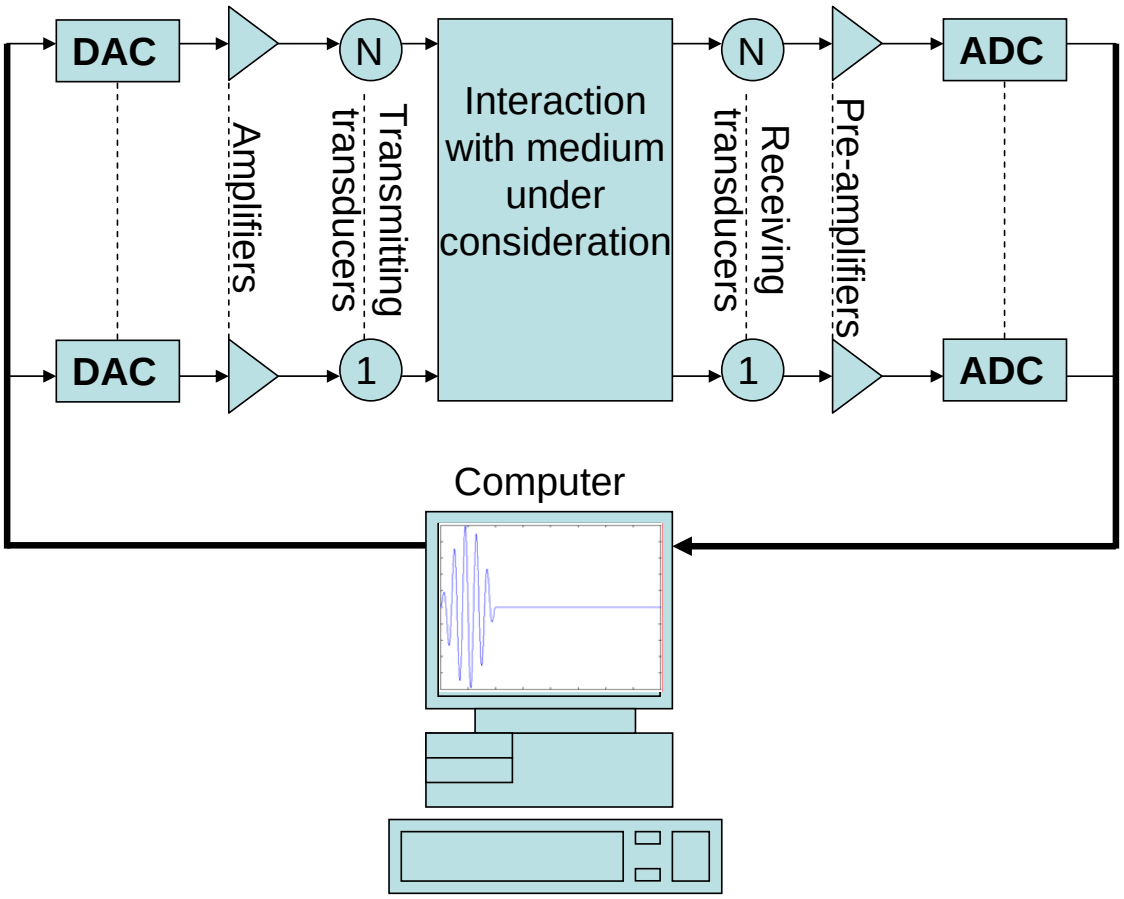

Figure 4.2: *Schematic of the architecture of a controller used to drive an array of transducers.*

computer, this digital signal is converted into a voltage signal via a DAC (digital to analog converter), and then the resulting signal is fed through an amplifier and used as the input on the j^{th} element of the array. The transducer responds to the electrical input by generating a pressure wave that radiates into the background medium. The pressure wave interacts with the object and is then scattered and subsequently detected by each transducer which will then produce a voltage output. Each output signal is then passed through a preamplifier before being converted into a digital signal via an ADC (analog to digital converter) which determines the temporal sampling of the signal which is finally recorded at a computer.

The architecture given above describes one of the most flexible systems that is available, but this is also one of the most expensive as every channel requires: a DAC, an amplifier, a pre-amplifier and an ADC. In order to reduce the costs of

the system, multiplexers can be used; these devices act as switches between the amplifiers (or pre-amplifiers) and the transducers, so that one amplifier (or pre-amplifier) can be used for several transducers. The multiplexer controls which of the transducers the signal is being sent to (or received from), the transducer under consideration can then be switched as required. This approach can drastically reduce the cost of the system, but it negates the possibility of using phased arrays and can increase the time taken to record all of the required signals.

A simplification of the architecture described by Figure 4.2 is to omit each of the DACs. The input signal is not a waveform but a voltage spike, approaching a delta function (which will be singular for an instant and zero otherwise); this is fed through an amplifier to the transmitting transducer. However, instead of transmitting a perfect delta function, the transducer, which is characterized by a particular frequency response, will demonstrate a phenomenon known as ringing; this causes a wave-packet to be produced by the transducer, the properties of which are dictated by the physical properties of the transducer and the width of the voltage spike. The shape of the incident signal can be investigated by probing a homogeneous background, which contains no objects and analysing the received incident signals. The advantage of using voltage spikes is that it simplifies the architecture of the probing system. However, as the properties of the signal are dictated by the transducers, varying the signal could involve changing the array elements.

4.5 Discrete Far-Field Operator

In the previous chapter the scattered field resulting from the interaction of a monochromatic incident field with the object was built into the far-field matrix operator $\mathbf{K}_\infty$. In practice, instead of a monochromatic wavefield being generated, a broadband signal is generated at and detected over the finite number of elements that make up the array. This section will demonstrate how the signals received will be built into a discrete version of the far-field operator known as the multistatic response matrix or $\mathbf{K}$ matrix.

Before considering the individual entries of the **K** matrix it is necessary to consider the typical signals that will be received at each array element. The received signals will not only consist of the scattered field but will also contain the incident field. The two approaches that will be considered in this thesis to extract the scattered field from the total field are gating and subtraction.

One of the advantages of using a wavepacket rather than a continuous wave to interrogate an object is that under certain conditions the incident signal and the scattered signal are contained in two separate wavepackets. If the distance between the transmitter and the receiver is much smaller than the total of the distance traveled by the incident wave from the transmitter to the object and the scattered wave from the object to the receiver, as shown in Figure 4.3 (a), then gating can be employed in order to extract the scattered signal. In this case the incident and scattered signals are received as completely separated wavepackets as shown in Figure 4.3 (b). If it is known that the distance between the array and the object is significantly greater than the distance between any two elements of the array, then the incident and scattered signals for every possible received signal will be well separated, in which case a gate can be calculated and applied to each of the received signals. The gate is calculated to be a time interval during which the received signals only contain the incident signal, and then the part of the received signals that fall within the gate are set to zero, leaving only the scattered signals.

If the distance between the transmitter and receiver is similar to the total distance between the object and the transmitter and receiver as shown in Figure 4.3 (c), then the incident signal can overlap the scattered signal as shown in Figure 4.3 (d). In this case gating cannot be used as the signals are not well separated, so the method of subtraction is used instead. For subtraction to work, a background medium with no object is probed by the array. In this case only the incident wave is received and no scattering occurs. The received incident signals are then subtracted from the total received field when an object is present, leaving only the scattered field to be processed. In order for the method of subtraction to be valid the background medium that is probed in the absence of the object must have the same properties

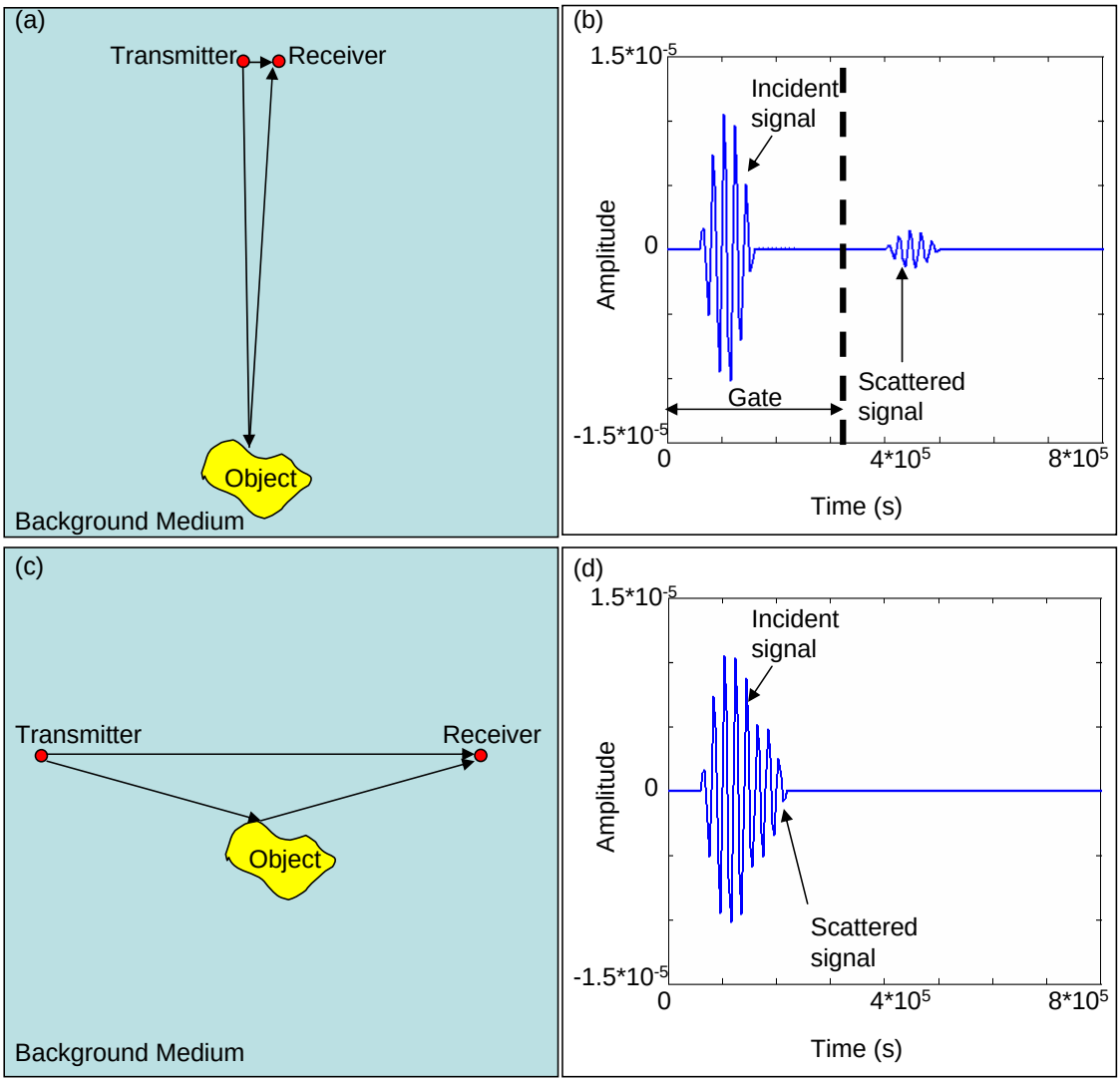

Figure 4.3: *Schematic of the illumination of an object. (a) The distance between the receiver and transmitter is much smaller than the total distance traveled by the incident wave to the object plus the distance traveled by the scattered wave from the object to the receiver; (b) A signal which is suitable for gating; (c) The distance between the receiver and the transmitter is similar to the total distance traveled by the incident wave to the object plus the distance traveled by the scattered wave from the object to the receiver; (d) A signal suitable for subtraction.*

as when the object is present. Small changes for example in the temperature of the medium can cause variations in the velocity of the wavefield, meaning the incident wave recorded in the absence of the object will not match that recorded when the object is present and so cause errors in retrieving the scattered signal.

Having separated the scattered signals from the incident signals by one of the methods described above, the $N \times N$ recorded signals are then used to build the multistatic response matrix, $\mathbf{K}$. The $(i,j)^{th}$ entry of the $\mathbf{K}$ matrix represents the response recorded at the array on the i^{th} element when the j^{th} element is fired. Due to reciprocity the matrix is symmetric, physically this means that the response measured on the i^{th} element when the j^{th} is fired is the same as when the roles are switched. In order to populate the $\mathbf{K}$ matrix, the Fourier transform of the $(i,j)^{th}$ received signal of the form shown in Figure 4.4 (a) is taken, leading to the spectrum shown in Figure 4.4 (b). The complex value of the Fourier transform at a predetermined frequency is then used as the $(i,j)^{th}$ entry in the $\mathbf{K}$ matrix.

As a polychromatic wave has been propagated, there is a wide frequency response as shown in Figure 4.4 (b). In this case the propagated signal had a central frequency of 100kHz, shown by the maximum at this frequency. In theory the $\mathbf{K}$ matrix could be constructed for any non-zero frequency response. However when measured experimentally the frequencies with a low amplitude will be masked by the presence of noise, so in practice the $\mathbf{K}$ matrix is created either at, or very close to the central frequency. In future chapters, unless stated otherwise, it will be assumed that the $\mathbf{K}$ matrix will be derived for the central frequency of the incident wave.

The factorization method that was derived under the continuous far-field operator $\mathbf{K}_\infty$ in the previous chapter can be easily adapted to the discrete $\mathbf{K}$ matrix. As with the far-field operator, the eigenvalues μ_j of the $\mathbf{K}$ matrix accumulate at zero. The continuous eigenfunctions v_j considered in Chapter 3 of the far-field operator $\mathbf{K}_\infty$ are replaced by discrete eigenvectors $\mathbf{v_j}$ of the $\mathbf{K}$ matrix. The continuous steering function $g_\infty(\hat{\mathbf{r}}, \mathbf{z})$ becomes the discrete steering vector $\mathbf{g}(\hat{\mathbf{r}}, \mathbf{z})$ which is used to project wavefields from the directions of the array elements to the position $\mathbf{z}$. The discrete version of Equation 3.14 is given by:

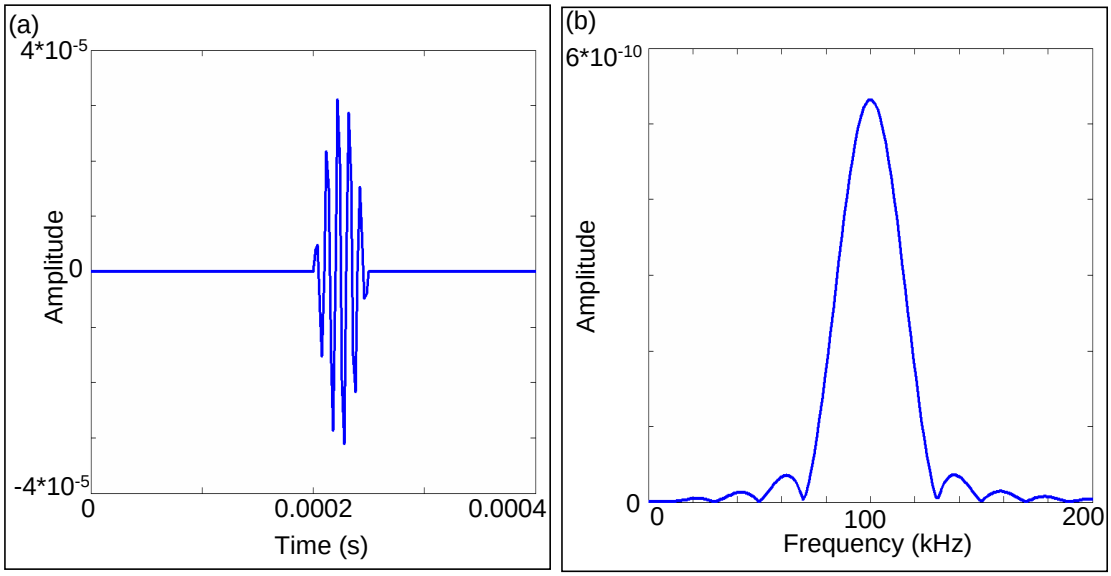

Figure 4.4: *Scattered signals. (a) A typical scattered signal (b) Amplitude of the Fourier transform of the scattered signal.*

$$FM(\mathbf{z}) = \frac{1}{\sum_{j=1}^{N} \frac{1}{\mu_j} |\langle \mathbf{g}(\mathbf{z}) | \mathbf{v}_j \rangle|^2}, \tag{4.4}$$

where the infinite sum used in the continuous case has been replaced by a finite sum limited by N, the number of the elements in the array.

4.6 Summary

This chapter has discussed the practical aspects of measuring the scattered field produced when an object to be imaged is probed with an incident wave. In general the scattered field is measured at a discrete number of detectors which form an array. The distance between these points is dictated by the wavelength of the interrogating wavefield and the size of the object. This thesis considers arrays which illuminate the object under consideration using every possible transmit-receive combination of array elements, following either gating of the incident field or its subtraction from the recorded signal. The resulting scattered signals are recorded in the **K** matrix. As discussed above, this matrix is a discrete version of the far-field operator

$\mathbf{K}_\infty$. It has been shown that the Factorization method can easily be adapted from the continuous case to the discrete case. In the following chapter further imaging methods will be described, and these will be derived in terms of a discrete system.

Chapter 5

Imaging methods for point-like scatterers

So far in this thesis no prior knowledge has been assumed about the properties of the object function, this chapter will examine imaging methods developed under the assumption that the object consists only of point scatterers. Although the imaging of point scatterers may not seem to be physically realistic, this is often a useful way to image objects which are small in comparison to the wavelength and so can be considered to be point-like, in this thesis these techniques will not only be applied to the case of point targets but also the case of finite objects. The imaging methods under consideration in this chapter were initially developed under the framework of a passive array system. In contrast with active array systems, passive systems do not actively illuminate the object but instead rely upon either the object emitting wavefields itself or illumination from an external source. This chapter will show how these methods can be adapted to the case of an active array system and will subsequently be used in future chapters.

The imaging techniques that have been developed for use with a passive array system assume that the data received at the array contains random noise, for this reason the next section will explain how noise affects the measured data and how noise can be modeled. This description of noise will then be incorporated into the model

which describes the data that would be recorded at a passive array system. The Bartlett, Maximum Likelihood and MUSIC imaging methods which were originally developed for use with a passive array system, will then be described. The link between the passive and active array systems will then be described and how the previously discussed imaging methods can be adapted to the active array system will be explained.

5.1 A Noise Model

As alluded to in previous chapters, in order for an imaging method to be applicable to real world situations it must be robust enough to cope with the effects of noise in the measured data. The reason for this robustness is that any experimental measurements will be contaminated by noise. In the measured scattered field, noise will represent random perturbations. Due to the random nature of the perturbations it is virtually impossible to completely remove the effects of noise from the measured field, a common assumption however is that the noise will have zero mean (see for example [69], [70] and [71]) and so taking the average of the received field over several realizations should reduce the effects of any noise. Averaging however, requires an increase in the total time in order to complete all of the measurements, this is only possible if the properties of the object and the background medium remain constant during the measurements. In some scenarios very few realizations can be taken before the properties of the system change and so averaging is not always practical.

For a monochromatic wavefield incident on an array of detectors it will be assumed that the noise distribution across the array elements at a particular instant in time can be considered as a single realization of noise. The statistics of this single realization across the array is modelled as a complex random variable with a zero mean. For a single array element, the statistics of noise as a function of time is assumed to be the same as that assumed for a single realization of noise across the array meaning that the random process is ergodic.

The random perturbation caused by noise is described as:

$$n_0 = \sigma A e^{iq\pi}, \tag{5.1}$$

where in the passive case A and q are real random variables and σ is the standard deviation of the noise. The random variable A has a Gaussian distribution with zero mean and standard deviation of 1. The variable q has a uniform distribution between $[-1\ 1]$, meaning that the phase of noise is uniformly distributed between $[-\pi\ \pi]$. The standard deviation σ is dependant on the noise level of the system relative to an average signal strength across the array and will be described below.

For a passive array consisting of N elements and M point sources, the recorded signals can be represented in an $(N \times 1)$ vector $\mathbf{p}$ (see for example [69], [72] and [70]) using the following model:

$$\mathbf{p}(t) = \mathbf{H}(\mathbf{a_1}, \mathbf{a_2}, .., \mathbf{a_N}, \mathbf{z_1}, \mathbf{z_2}, .., \mathbf{z_M})\mathbf{s}(t) + \mathbf{n_0}(t), \tag{5.2}$$

where $\mathbf{H}$ is an $(N \times M)$ matrix which represents the propagation of the signals from the locations of the M point sources (represented by $\mathbf{z_j}$ $j = [1..M]$) to the coordinates of the N array elements (given by $\mathbf{a_j}$ $j = [1..N]$). It will be assumed that the locations of both the array elements and the sources will remain constant in Equation 5.2 and so the dependance on these coordinates is taken as understood and dropped from further equations. It should be noted that the j^{th} column of the $\mathbf{H}$ matrix corresponds to the steering vector $\mathbf{g}(\hat{\mathbf{r}}, \mathbf{z_j})$ between the array elements and the j^{th} source. The $(M \times 1)$ column vector $\mathbf{s}(t)$ represents the wave fields emitted by the M sources. The $(N \times 1)$ column vector $\mathbf{n_0}(t)$ represents the noise present in the system, each entry of which is described by a realization of Equation 5.1. In this case the standard deviation of the noise for a given instant in time is given by:

$$\sigma = \frac{\|\mathbf{Hs}\|}{\sqrt{N}} c_N, \tag{5.3}$$

where $\|\mathbf{Hs}\| = \sqrt{\sum_{j=1}^{N}(\mathbf{Hs})_j}$ is the Frobenius norm of the noiseless system and c_N describes the level of the noise present.

In order to build an image, several realizations of $\mathbf{p}(t)$ are recorded and are then temporally averaged in order to construct the so-called covariance matrix $\mathbf{C_0}$ such that:

$$\mathbf{C_0} = E[\mathbf{p}\mathbf{p}^\dagger] = \mathbf{H}E[\mathbf{s}(t)\mathbf{s}^\dagger(t)]\mathbf{H}^\dagger + \mathbf{H}E[\mathbf{s}(t)\mathbf{n_0}^\dagger(t)] + \mathbf{H}^\dagger E[\mathbf{s}(t)^\dagger\mathbf{n_0}(t)] + E[\mathbf{n_0}(t)\mathbf{n_0^\dagger}(t)], \tag{5.4}$$

where $E[..]$ represents the expected or average value in time. It is assumed the noise is uncorrelated to the signals implying the cross terms vanish, such that:

$$\mathbf{C_0} = \mathbf{H}E[\mathbf{s}(t)\mathbf{s}^\dagger(t)]\mathbf{H}^\dagger + \sigma^2\mathbf{I}, \tag{5.5}$$

where σ^2 is the variance of the noise. The covariance matrix is central to passive imaging techniques used in the fields of astronomy and RADAR. The next section will examine how the covariance matrix can be manipulated in order to provide information about the sources present in the background medium.

5.2 Passive Imaging

This section will describe the Beamforming, Maximum Likelihood and MUSIC methods that have been developed for use with a passive array system. Each technique uses the covariance matrix in order to build an image of the region of interest to determine the presence of any point sources. Each of these methods will be transformed so that they can be used under an active array system later in this chapter.

5.2.1 Beamforming

Beamforming techniques were some of the earliest imaging methods developed in order to determine the location of point sources from the signals received at a passive array. Beamforming combines the covariance matrix $\mathbf{C_0}$ with a choice of weight vector $\mathbf{w}$ in order to scan the region of interest. The choice of weight vector $\mathbf{w}$ is crucial and will determine the resolution limit of the imaging technique. Beamforming techniques aim to maximize the quantity:

$$P(\mathbf{z}) = \mathbf{w}^{\dagger}(\mathbf{z})\mathbf{C_0}\mathbf{w}(\mathbf{z}), \tag{5.6}$$

which relates to the power output of the array. The Bartlett method based on the spectral analysis explored in [73] (also known as the conventional beamforming method) was developed in the early days of RADAR and takes the weight vector to be equal to the steering vector $\mathbf{g}(\hat{\mathbf{r}}, \mathbf{z})$ as shown in [69], [74], meaning that Equation 5.6 becomes:

$$BM(\mathbf{z}) = \mathbf{g}^{\dagger}(\hat{\mathbf{r}}, \mathbf{z})\mathbf{C_0}\mathbf{g}(\hat{\mathbf{r}}, \mathbf{z}). \tag{5.7}$$

An image is built by scanning the steering vector $\mathbf{g}(\hat{\mathbf{r}}, \mathbf{z})$ over the coordinates of the region of interest, producing a maximum when scanned over the location of a point source. The Bartlett imaging method is constrained by the Rayleigh resolution limit and so is not able to distinguish sources separated by less than $\lambda/2$.

An alternative beamforming method proposed by Capon [75] and also investigated in [74], [70], [72] and [69] takes the following weight function:

$$\mathbf{w} = \frac{\mathbf{C_0^{-1}}\mathbf{g}(\hat{\mathbf{r}}, \mathbf{z})}{\mathbf{g}(\hat{\mathbf{r}}, \mathbf{z})^{\dagger}\mathbf{C_0^{-1}}\mathbf{g}(\hat{\mathbf{r}}, \mathbf{z})}. \tag{5.8}$$

Inserting Equation 5.8 into Equation 5.6 yields:

$$CAPON(\mathbf{z}) = \frac{1}{\mathbf{g}(\hat{\mathbf{r}}, \mathbf{z})^{\dagger} \mathbf{C_0^{-1}} \mathbf{g}(\hat{\mathbf{r}}, \mathbf{z})}, \tag{5.9}$$

this method is capable of achieving super resolution, demonstrating that, depending upon the choice of weight vector, Beamforming techniques are not necessarily constrained by the Rayleigh resolution limit. Both of the Beamforming techniques discussed in this subsection provide information on the location of the sources but cannot be used to determine the signals $\mathbf{s}$ or the noise that is present in the system.

5.2.2 Maximum Likelihood

Unlike Beamforming methods, the Maximum Likelihood method considered in this thesis aims to determine not only the location of the point sources but also the nature of the signal vector $\mathbf{s}$ and the variance of the noise σ^2 as discussed in [69]. In order to achieve this, the Maximum Likelihood method uses sets of known parameters to construct the solutions to several forward problems and then compares the results to the measured data. The construction which most closely resembles the measured data is chosen and the corresponding parameters relating to the signal, source locations and noise level are taken as the most likely to have caused the measured data, resulting in super resolution being achieved.

In order for the Maximum Likelihood method to be successful it is crucial that the number of sources is known a priori. In the absence of noise, if the sources are uncorrelated then the rank of the covariance matrix equals the number of sources that are present. In the presence of noise none of the eigenvalues of the covariance matrix are zero however providing the noise level is not detrimentally large the number of eigenvalues with a dominant amplitude will equal the number of sources. The rest of the eigenvalues will have a much lower amplitude and so the number of sources can still be determined in the presence of noise. However, if the sources are correlated then the number of sources cannot be determined from the eigenvalues of the covariance matrix and so this information needs to be known beforehand. As such

it will be assumed that sources are uncorrelated and that the number of sources can be determined from the number of dominant eigenvalues of the covariance matrix.

Having determined the number of sources present, the inverse problem of finding the location and strength of the sources can be solved by constructing sets relating to the possible locations, signals and noise levels. The set relating to the locations of the sources will consist of every possible combination of M coordinates in the region of interest, each combination will be used to construct an $(2 \times M)$ matrix $\mathbf{Z_{ML}}$, the columns of which correspond to the possible coordinates of the sources (in 3D $\mathbf{Z_{ML}}$ would become a $(3 \times M)$ matrix). The coordinates of the sources given by $\mathbf{Z_{ML}}$ are used in conjunction with the known location of the array elements to construct $(N \times M)$ $\mathbf{H_{ML}}$ matrices which describes how the wave fields would propagate from the specific combination of source coordinates to the known coordinates of the array elements. The set of signals will consist of every possible $(M \times 1)$ column vector $\mathbf{s_{ML}}(t)$ that could have caused the measured data. The set based on the noise levels will consist of all possible values of the variance σ^2. Every combination of possible locations, signals and noise level are then combined to create a constructed covariance matrix $\mathbf{C_{ML}}(\mathbf{H_{ML}}, \mathbf{s}(t), \sigma^2_{ML})$ based upon Equation 5.5. The constructed covariance matrix that minimizes the quantity:

$$ML = \min_{\mathbf{Z_{ML}}, \mathbf{s_{ML}}(t), \sigma^2_{ML}} \|\mathbf{C_0} - \mathbf{C_{ML}}(\mathbf{H_{ML}}, \mathbf{s}(t), \sigma^2_{ML})\|^2, \tag{5.10}$$

is chosen as the most likely and the corresponding parameters taken as describing the properties of the forward problem.

The Maximum Likelihood method requires the solution to many forward problems to be calculated and as such is computationally intensive. In the active case the maximum likelihood method will be based upon slightly different parameters than those discussed here, this will be discussed after the derivation of the final imaging method that will be considered in this thesis.

5.2.3 MUSIC

MUltiple SIgnal Classification or MUSIC was initially developed as a method to determine the properties of multiple wave fields received at an array in a passive system as described by Schmidt [72]. The MUSIC algorithm uses a subset of the eigenvectors of the covariance matrix in order to locate the sources of the received signals. The M eigenvectors which relate to the M dominant eigenvalues of the covariance matrix create what is known as the signal space, the remaining eigenvectors form what is known as the noise space. The eigenvectors of the noise space are used to construct the $(N - M)$ columns of the matrix $\mathbf{C_{0N}}$, which is used by the MUSIC algorithm to scan the region of interest for point sources:

$$MUSIC(\mathbf{z}) = \frac{1}{\mathbf{g}^{\dagger}(\hat{\mathbf{r}}, \mathbf{z})\mathbf{C_{0N}}\mathbf{C}_{\mathbf{0N}}^{\dagger}\mathbf{g}(\hat{\mathbf{r}}, \mathbf{z})}. \tag{5.11}$$

Equation 5.11 uses the steering function $\mathbf{g}(\hat{\mathbf{r}}, \mathbf{z})$ in order to scan the region of interest by varying the quantity $\mathbf{z}$. The eigenvectors that make up the noise space are orthogonal to the those of the signal space, a linear combination of which relate to the locations of the point scatterers. As such the denominator of Equation 5.11 (which represents the projection of the noise space vectors to the coordinate $\mathbf{z}$) will be zero when scanned over the location of a point source due to orthogonality, hence Equation 5.11 will become unbounded at the coordinates of a point source. Like the Capon and Maximum Likelihood methods, this technique can also achieve super resolution.

5.3 Active Imaging

The imaging methods that have been discussed in this chapter have been derived under a passive array system, however, in order to be applied to an active array system as will be done in future chapters a link between the two systems must be explored as discussed in [70]. For this reason consider a system of N array elements

illuminating M point scatterers, the resulting scattered field would be measured in the $(N \times N)$ multistatic response matrix, which in the presence of noise can be described by:

$$\mathbf{K_0} = \mathbf{HDH^T} + \mathbf{N_0}. \tag{5.12}$$

The $(i,j)^{th}$ entry of the $\mathbf{K_0}$ matrix represents the frequency response that would be measured on the i^{th} element due to the illumination of the object from the j^{th} array element. In the active case $\mathbf{H}$ represents the propagation of the wave fields from the point scatterers to the array elements and due to reciprocity the propagation of the wave fields to the location of the point scatterers from the array elements is represented by $\mathbf{H^T}$, where $^\mathbf{T}$ represents the transpose of a matrix. The scattering caused by the presence of the point scatterers is represented by the matrix $\mathbf{D}$ and describes the scattering coefficients of the point scatterers and the effects of multiple scattering that may be present in the system see for example the paper by Marengo and Gruber [76].

The $(N \times N)$ matrix $\mathbf{N}$ represents any noise that is present in the system each entry of which is given by a realization of Equation 5.1. In the active case the standard deviation of the noise is given by:

$$\sigma = \frac{\|\mathbf{HDH^T}\|}{N} c_N, \tag{5.13}$$

note that in contrast to the passive case where the standard deviation is based upon the $(N \times 1)$ signal vector $\mathbf{Hs}$, in the active case the standard deviation is based upon the $(N \times N)$ matrix $\mathbf{HDH^T}$.

It can be observed that the self adjoint matrix $\mathbf{K_0 K_0^\dagger}$ has the form:

$$\mathbf{K_0 K_0^\dagger} = \mathbf{HDH^T H^* D^\dagger H^\dagger} + (\mathbf{H^* D^\dagger H^\dagger})\mathbf{N_0} + (\mathbf{HDH^T})\mathbf{N_0^\dagger} + \mathbf{N_0 N_0^\dagger}, \tag{5.14}$$

where * represents the conjugate of the matrix. The matrix $\mathbf{K_0 K_0^\dagger}$ is the Time Reversal operator $\mathbf{T_0}$ as defined by Prada [47], the structure of which is similar to that of the covariance matrix given by Equation 5.4. In particular in the absence of noise Equations 5.4 and 5.14 are of the form $\mathbf{HGH^\dagger}$, where $\mathbf{G} = E[\mathbf{s}(t)\mathbf{s}^\dagger(t)]$ in the passive case and $\mathbf{G} = \mathbf{DH^T H^* D^\dagger}$ in the active case.

From linear algebra the rank of the matrix $\mathbf{HGH^\dagger}$ is the same as the rank of $\mathbf{G}$. In the passive case the rank of $\mathbf{G}$ is equal to the number of point sources assuming the sources are uncorrelated. In the active case the rank of $\mathbf{G}$ is equal to the number of scatterers as demonstrated by Devaney [71]. This suggests that the role of different temporal realizations in passive imaging is replaced by multiple illumination directions in active imaging, as such in the noiseless case the imaging methods developed for a passive array system can be used with an active array system provided the covariance matrix is replaced with $\mathbf{K_0 K_0^\dagger}$. It was argued by Prada and Thomas [70] that the passive and active models are equal in the presence of noise, claiming that the cross terms of Equation 5.14 would vanish due to the noise and signals being uncorrelated. However, the terms do not necessarily vanish since they are not averaged over several realizations as in the passive case. It should also be noted that the final term in Equation 5.14, $\mathbf{N_0 N_0^\dagger}$, is not necessarily given by a diagonal matrix as in the passive case. Nevertheless, due to the dominant role of the $\mathbf{HGH^\dagger}$ matrix in Equation 5.14 the passive imaging methods should perform well in the case of an active system. The passive imaging methods that were previously discussed in this chapter will be adapted to be used with an active imaging system in the following subsections.

Finally it should be observed that while in the passive case the rank of $\mathbf{G}$ only provides the number of sources if they are uncorrelated. In the active case, the rank of $\mathbf{G}$ is always the same as the number of scatterers, this means that in the active case there is no need to know the number of scatterers beforehand.

5.3.1 Beamforming

Under an active array system, the covariance matrix in Equation 5.7 is simply replaced by the time reversal matrix, so the Bartlett imaging method under an active system is given by:

$$BM(\mathbf{z}) = \mathbf{g}^{\dagger}(\hat{\mathbf{r}}, \mathbf{z})\mathbf{K_0}\mathbf{K_0^{\dagger}}\mathbf{g}(\hat{\mathbf{r}}, \mathbf{z}). \tag{5.15}$$

or equivalently:

$$BM(\mathbf{z}) = \sum_{j=1}^{N} |\mu_j|^2 |\langle \mathbf{g}(\hat{\mathbf{r}}, \mathbf{z}) | \mathbf{v}_j \rangle|^2, \tag{5.16}$$

where μ_j and $\mathbf{v_j}$ $j = [1..N]$ are the eigenvalues and eigenvectors respectively of the $\mathbf{K_0}$ matrix derived from the singular value decomposition of $\mathbf{K_0}$ as discussed in Chapter 2. As in the passive case, the region of interest is scanned by varying the steering function, when scanned over the location of a point scatterer Equation 5.16 will produce a maximum. Equation 5.16 is equivalent to the first iteration in physical time reversal and represents the array emitting an incident field which will focus simultaneously on each of the locations of the point scatterers that are present in the background medium. In a similar fashion to the Factorization method this method will provide information on locations of the point scatterers but not their physical properties. When applied to finite objects, this method will provide information on the support of the object but not the index of refraction. Unlike the Factorization method the Bartlett imaging method is restricted by the Rayleigh resolution limit but will be used in this thesis to compare conventional imaging techniques with those that can achieve super resolution.

The Bartlett method in Equation 5.16 is similar to the DORT technique (in French, Décomposition de l'Opérateur de Retournement Temporel) see for example [47], in which case it is assumed that the eigenvectors corresponding to the dominant

eigenvalues each corresponds to the location of a single point target. However as explained by Devaney [71] if the distance between the targets is small then the eigenvectors do not correspond to the location of a single point scatterer but instead the locations are given by a linear combination of the eigenvectors. As such the DORT method breaks down as the distance between any point scatterers is reduced for this reason the DORT method will not be used in this thesis.

Adapting the Capon method to be used with an active array system by substituting the time reversal matrix for the covariance matrix in Equation 5.9 leads to a method which is equivalent to the Factorization method. It should be noted that although these methods are equivalent, they were derived independently. In particular the Factorization method was derived in the more general framework of extended objects.

5.3.2 Maximum Likelihood

As under the passive array system the Maximum Likelihood method under an active array system compares simulated data constructed from sets of known parameters to the received data. The constructed data is compared to the measured multistatic response matrix $\mathbf{K_0}$.

In the noiseless case the rank of the $\mathbf{K_0}$ matrix is equal to the number of point scatterers that are illuminated by the array. In a similar fashion to the passive system, when noise is introduced to the active system none of the eigenvalues will be zero but the M dominant eigenvalues will relate to the number of point scatterers. As in the passive case, a set consisting of all of the possible locations of the M point scatterers consisting of $2 \times M$ matrices $\mathbf{Z_{ML}}$ is created and used in conjunction with the known locations of the array elements to construct the $\mathbf{H_{ML}}$ matrix for every possible combination of M point scatterers. A set containing all possible combinations of the M scattering coefficients which are represented by an $M \times 1$ column vector $\tau_{\mathbf{ML}}$ is also constructed. The set of scattering coefficients is used in combination with the set of possible locations to construct forward scattering models

which are then compared to the measured data. The most likely combination of coordinates and scattering coefficients are those that minimize:

$$ML = \min_{\mathbf{Z_{ML}}, \tau_{\mathbf{ML}}} \|\mathbf{K_0} - \mathbf{K_{ML}}(\mathbf{Z_{ML}}, \tau_{\mathbf{ML}})\|^2, \tag{5.17}$$

where $\mathbf{K_{ML}}(\mathbf{Z_{ML}}, \tau_{\mathbf{ML}})$ is the simulated solution to the forward problem with properties defined by $\mathbf{Z_{ML}}$ and $\tau_{\mathbf{ML}}$.

It should be noted that the Maximum Likelihood method under an active array system can construct solutions to the forward problem assuming either the Born Approximation or Multiple Scattering models, this property will be investigated in the next chapter.

5.3.3 TR-MUSIC

Initial attempts to adapt the MUSIC algorithm described by Schmidt to the active case only worked when there was no correlation between the signals received at the array as discussed by Devaney [71]. It was Devaney who first suggested that analysis of the eigenspace of the $\mathbf{K_0}$ matrix or equivalently the time reversal $\mathbf{T_0}$ matrix would allow the MUSIC method to be adapted to an active array system, thus becoming known as the Time Reversal and MUSIC method (TR-MUSIC).

In a similar fashion to the MUSIC method under the passive array system, the TR-MUSIC method uses the eigenvectors of the noise space of the $\mathbf{T_0}$ matrix or equivalently $\mathbf{K_0}$ matrix to construct an image. If the columns of the $N \times (N - M)$ matrix $\mathbf{K_{0N}}$ correspond to the eigenvectors of the noise space then the TR-MUSIC algorithm is given by:

$$TRM(\mathbf{z}) = \frac{1}{\mathbf{g}(\hat{\mathbf{r}}, \mathbf{z}^\dagger)\mathbf{K_{0N}}\mathbf{K_{0N}^\dagger}\mathbf{g}(\hat{\mathbf{r}}, \mathbf{z})}, \tag{5.18}$$

or equivalently:

$$TRM(\mathbf{z}) = \frac{1}{\sum_{j=M+1}^{N} |\langle \mathbf{g}(\hat{\mathbf{r}}, \mathbf{z}) | \mathbf{v}_j \rangle|^2}, \tag{5.19}$$

where $|\mathbf{v_j}\rangle$ $j = [M+1..N]$ are the eigenvectors of the noise space. In the absence of noise, the eigenvectors of the noise space satisfy $\mathbf{K}|\mathbf{v_j}\rangle = \mathbf{0}$ $j = [M+1..N]$ which represents the far-field pattern detected at the array due to an excitation described by $\mathbf{v_j}$ as discussed in Chapter 2. As the far-field pattern in this case is zero the illumination of the object by the fields represented by the eigenvectors $\mathbf{v_j}$ $j = [M+1,..,N]$ do not cause any scattering. If the field is not scattered, this implies that the incident field is zero at the location of the scatterers. The Time Reversal and MUSIC algorithm investigates the magnitude of the wavefield in the region of interest due to an incident field generated at the array corresponding to the eigenvectors of the noise space. The steering function $\mathbf{g}(\hat{\mathbf{r}}, \mathbf{z})$ is used to scan the region of interest in order to determine the magnitude of the field at the point $\mathbf{z}$. The quantity $|\langle \mathbf{g}(\hat{\mathbf{r}}, \mathbf{z}) | \mathbf{v}_j \rangle|^2$ represents the wave field at the point $\mathbf{z}$ due to the incident field represented by the eigenvector $\mathbf{v_j}$, this will become zero when $\mathbf{z}$ corresponds to the location of a point scatterer, implying that Equation 5.19 will become unbounded in the absence of noise. When noise is present in the system none of the eigenvalues of the matrix $\mathbf{K_0}$ are zero. However, the noise and signal spaces can be determined by allowing the signal space to be defined by the eigenvectors with dominant eigenvalues, the remaining eigenvectors make up the noise space. It should be noted that for the case of point scatterers the Factorization and TR-MUSIC methods are equivalent as shown in [77]. In the presence of noise Equation 5.19 will not become unbounded when scanned across the location of a scatterer but will instead be large in comparison with any other points in the region of interest. In a similar fashion to the Factorization and Bartlett methods, the TR-MUSIC method provides information on the location of the scatterers but not their properties and when applied to the measured data for an extended object (one which cannot be considered to be point-like with respect to the wavelength) will provide information on the support of the object but not its index of refraction as discussed in [78], [79] and [80].

5.4 Summary

This chapter has looked at imaging methods that were initially developed for the detection of point sources under a passive array system. The model that describes the data that would be received at a passive array system due to illumination by point sources has been examined. The passive model included a description of the Gaussian noise model that will be used in this thesis in order to simulate the effects of noise. The Bartlett, Capon, Maximum Likelihood and MUSIC methods were then described under the passive array system. As this thesis is concerned with active illumination, a link between the active and passive array models was then described, this allowed the imaging methods to be adapted to be used under an active array system. In future chapters, the imaging methods discussed in this chapter will be applied to active array systems illuminating point scatterers and finite objects.

Chapter 6

Demonstration of super resolution for point scatterers

6.1 Introduction

This chapter will consider the scattering problem for the case of two subwavelength separated point scatterers. This problem can be evaluated analytically and so avoids the inclusion of any physical or numerical noise that would be present in experimental or numerical results and is a convenient way of evaluating the resolution limits of imaging methods. The analytical nature of the problem enables the physical model (which represents the analytical model used to create the scattered field and should not be confused with experimental results) to be described both with and without the effects of multiple scattering being considered. The forward problem will be investigated under both physical models in the next section, it will be shown that including the effects of multiple scattering in the physical model enriches the scattered field and encodes more information about the subwavelength structure of the object to the far field.

With respect to the inverse problem, it will be demonstrated that super resolution can be achieved under both the Born Approximation and when multiple scattering is considered. However, when noise is added to the physical model produced un-

der the Born Approximation, inversion techniques will be unable to resolve the two point scatterers, at lower noise levels than when Multiple Scattering is present in the forward scattering model. It is also shown that the imaging model (which is the scattering model an imaging method assumes is valid) must match the physical model that has created the measured data, otherwise any reconstructions will contain artifacts. Finally this chapter will apply the imaging techniques derived in previous chapters to experimental data obtained from probing two point-like scatterers.

6.2 Forward Problem

This section will investigate the consequences to the forward problem of illuminating two point scatterers under the physical models of the Born Approximation and Multiple Scattering. It will be shown that assuming a physical model which uses the Born Approximation produces a scattered field which is similar to that produced by a single point scatterer, whilst the scattered field produced under the Multiple Scattering physical model is more complex. It will also be shown that multiple scattering encodes more information about the subwavelength structure of the object to the far field than the Born Approximated physical model. The solutions to the forward problem produced by the two physical models under consideration will be used in the next section as part of the inverse problem to determine the location of the two point scatterers from the scattered field.

6.2.1 Far-field Patterns

This section will investigate the far-field patterns produced by illuminating two point scatterers under the Born Approximation and Foldy-Lax models. The Foldy-Lax model describes the effects of multiple scattering when the object consists of point scatterers [81]. Consider the description of the scattering amplitude that was given in Chapter 2 as:

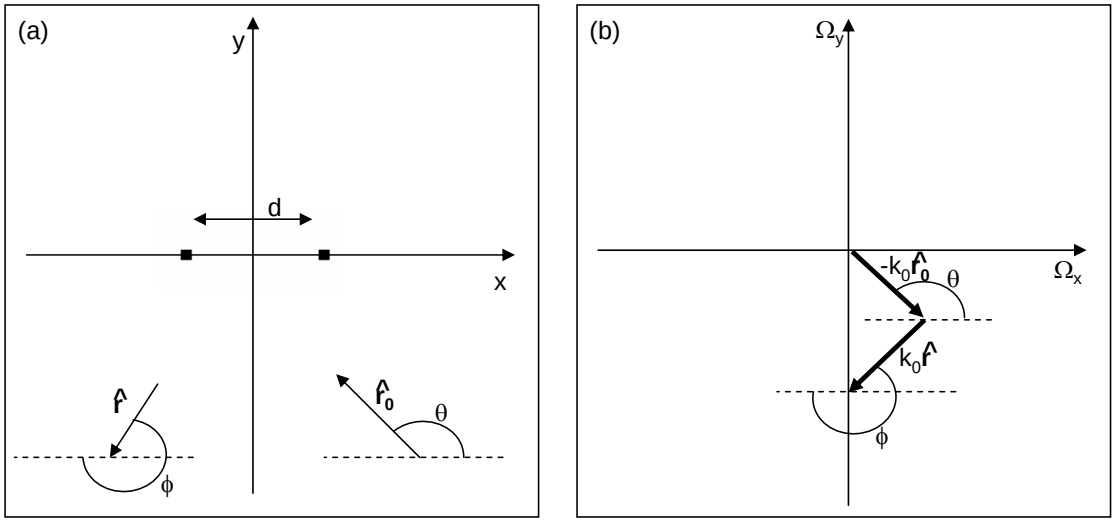

Figure 6.1: *The object is illuminated from the direction* $\hat{\mathbf{r}}_\mathbf{0}$ *the scattered field is detected for all* ϕ*. (a) 2D tomographic setup for the case of two point scatterers, (b)* $\mathbf{\Omega}$ *domain, the scattered field measured in the direction* $\hat{\mathbf{r}}$ *due to an illumination from the direction* $\hat{\mathbf{r}}_\mathbf{0}$ *is mapped to the point* $\Omega = 2\pi/\lambda(\hat{\mathbf{r}}_\mathbf{0} - \hat{\mathbf{r}})$*.*

$$f(k_0\hat{\mathbf{r}}, k_0\hat{\mathbf{r}}_\mathbf{0}) = \int_D d^2r' e^{-ik_0\hat{\mathbf{r}}\cdot\mathbf{r}'} O(\mathbf{r}')\psi(\mathbf{r}', k_0\hat{\mathbf{r}}_\mathbf{0}), \tag{6.1}$$

where the illumination and detection directions are given by $\hat{\mathbf{r}}_\mathbf{0}$ and $\hat{\mathbf{r}}$ as shown in Figure 6.1 (a). In the case of two point scatterers, the object function is given by:

$$O(\mathbf{r}) = \tau_1\delta(\mathbf{r} - \mathbf{z}_\mathbf{1}) + \tau_2\delta(\mathbf{r} - \mathbf{z}_\mathbf{2}), \tag{6.2}$$

where $\delta(\mathbf{r} - \mathbf{z})$ is the Dirac delta function which is singular when $\mathbf{r} = \mathbf{z}$ and zero otherwise. The locations of the scatterers are given by $\mathbf{z}_\mathbf{1} = (-d/2, 0)$ and $\mathbf{z}_\mathbf{2} = (d/2, 0)$, where d is the separation distance between the point scatterers as shown in Figure 6.1 (a). For simplicity it will be assumed that the scattering coefficients $\tau_1 = \tau_2 = \tau$, and that the scatterers are isotropic. It is also assumed that the scattering is elastic (so no dissipation of energy occurs), thus in order to satisfy the laws of energy conservation τ must satisfy:

$$\tau = 2(e^{ip} + i), \tag{6.3}$$

where $p \in [0, 2\pi]$ (as described in Appendix A).

Under the Born Approximation the scattered field ψ_s caused by the two scatterers is given by:

$$\psi_s^{BA}(\mathbf{r}, \hat{\mathbf{r}}_\mathbf{0}) = -\tau e^{ik_0 \hat{\mathbf{r}}_\mathbf{0} \cdot \mathbf{z_1}} G(\mathbf{r}, \mathbf{z_1}) - \tau e^{ik_0 \hat{\mathbf{r}}_\mathbf{0} \cdot \mathbf{z_2}} G(\mathbf{r}, \mathbf{z_2}) \tag{6.4}$$

where $G(\mathbf{r}, \mathbf{z_j})$ is the Green's function as defined in Chapter 2 between the points $\mathbf{r}$ and $\mathbf{z_j}$. The first term on the RHS of Equation 6.4 represents the scattered field if a scatterer located at $\mathbf{z_1}$ were to be considered in seclusion, likewise the second term represents the scattered field for a single scatterer located at $\mathbf{z_2}$. In contrast, the scattered field when multiple scattering is considered is given by the Foldy-Lax model as:

$$\psi_s^{MS}(\mathbf{r}, \hat{\mathbf{r}}_\mathbf{0}) = \frac{\tau}{1 - \tau^2 G_0^2} \sum_{j=1}^{2} (e^{ik_0 \hat{\mathbf{r}}_\mathbf{0} \cdot \mathbf{z_j}} G(\mathbf{r}, \mathbf{z_j}) - \tau G_0 e^{ik_0 \hat{\mathbf{r}}_\mathbf{0} \cdot \mathbf{z_k}} G(\mathbf{r}, \mathbf{z_k})) \tag{6.5}$$

where $k = 2$ if $j = 1$, $k = 1$ if $j = 2$, $G_0 = G(\mathbf{z_1}, \mathbf{z_2})$ is the Green's function which describes the propagation effect between the scatterers. The magnitude of G_0 increases as the separation distance d decreases. Equation 6.5 contains the description of the scattered field under the Born Approximation as well as the infinite reverberations caused by the scattering between the two point scatterers. Equations 6.5 and 6.4 already highlight the difference between the forward models for two point scatterers, however, how this difference affects the far field pattern is not yet clear and so further investigation is required.

If the asymptotic form of the Green's function is used in Equations 6.4 and the unit vectors of illumination and detection are expressed in terms of the angles θ and ϕ

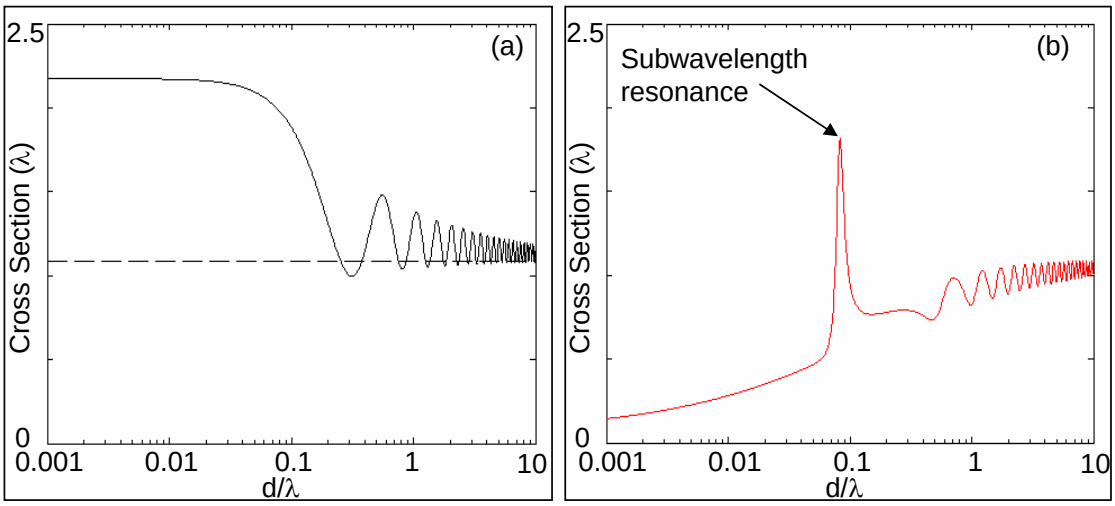

Figure 6.2: *The scattering and extinction cross sections for the two physical models for an incident angle $\theta = 0$ (a) The scattering cross section (solid line) and extinction cross section (dashed line) measured under the Born Approximation; according to energy conservation these should be identical, (b) The scattering cross section under the Multiple Scattering model; this is identical to extinction cross section in this case, a subwavelength resonance can be observed at $d/\lambda \approx 0.08$.*

as shown in Figure 6.1 then the scattering amplitude for the physical model under the Born Approximation is given by:

$$f_{BA}(\theta, \phi) = 2\tau cos[k_0 d/2(cos(\theta) - cos(\phi))]. \tag{6.6}$$

It should be noted that for any object function, the scattering amplitude under the Born Approximation will violate the laws of energy conservation [38]. For the case of the point scatterers this is illustrated by the scattering and extinction cross sections, which are shown in Figure 6.2 (a) as a function of d/λ with $\tau = 2(e^{i3\pi/4} + i)$, where in this case $p = 3\pi/4$. According to the optical theorem, these cross sections should be identical under elastic scattering, however, the scattering cross section is almost double the extinction cross section for $d \ll \lambda$. It should also be noted that as the separation distance increases the scattering cross section tends towards that of the extinction cross section.

In a similar fashion to Equation 6.6, the scattering amplitude under the multiple scattering physical model is given by substituting the asymptotic form of the Green's function into Equation 6.5 and representing the unit vectors in terms of the angles of illumination and detection such that:

$$f_{MS}(\theta,\phi) = \frac{2\tau}{1-\tau^2 G_0^2}\{cos[k_0 d/2(cos(\theta)-cos(\phi))]-\tau G_0 cos[k_0 d/2(cos(\theta)+cos(\phi))]\}. \tag{6.7}$$

The scattering amplitude produced under Foldy-Lax model is consistent with energy conservation laws as shown in [82] and so the scattering cross section shown for $\tau = 2(e^{i3\pi/4} + i)$ in Figure 6.2 (b) is identical to the extinction cross section. The scattering cross section of the scattering amplitude for the Multiple Scattering physical model produces resonances for certain subwavelength separation distances (depending upon the scattering coefficients) which can be observed in Figure 6.2 (b). This phenomenon corresponds to distances at which the effects of multiple scattering are maximised as $(1-\tau^2 G_0^2) \to 0$ in Equation 6.7. Note that G_0 describes the short range interaction between the scatterers. Subwavelength resonance phenomenon was predicted in the papers by Tolstoy [83], [84] and has also been investigated by Heller [85] and shown experimentally by Hersch and Heller in [86].

The amplitude and phase of the scattering amplitude measured for all detection angles ϕ for an illumination angle $\theta = 0$ (as shown in Figure 6.1) under both physical models are shown in Figure 6.3 for two scatterers with $\tau = 2(e^{i(3\pi/4)} + i)$ and a separation distance of $d = 0.1\lambda$ (chosen as it is close to the resonance of the scattering cross section and so should maximise the effects of multiple scattering in this model). There is a marked difference between the scattering amplitude of the field depending on whether or not multiple scattering is included in the scattering model. Under the Born Approximation the modulus of the scattering amplitude for the two point scatterers is similar to that of a monopole that would be measured for a single point scatterer located between the two scatterers, however when the effects of multiple scattering are considered the modulus is a hybrid between that

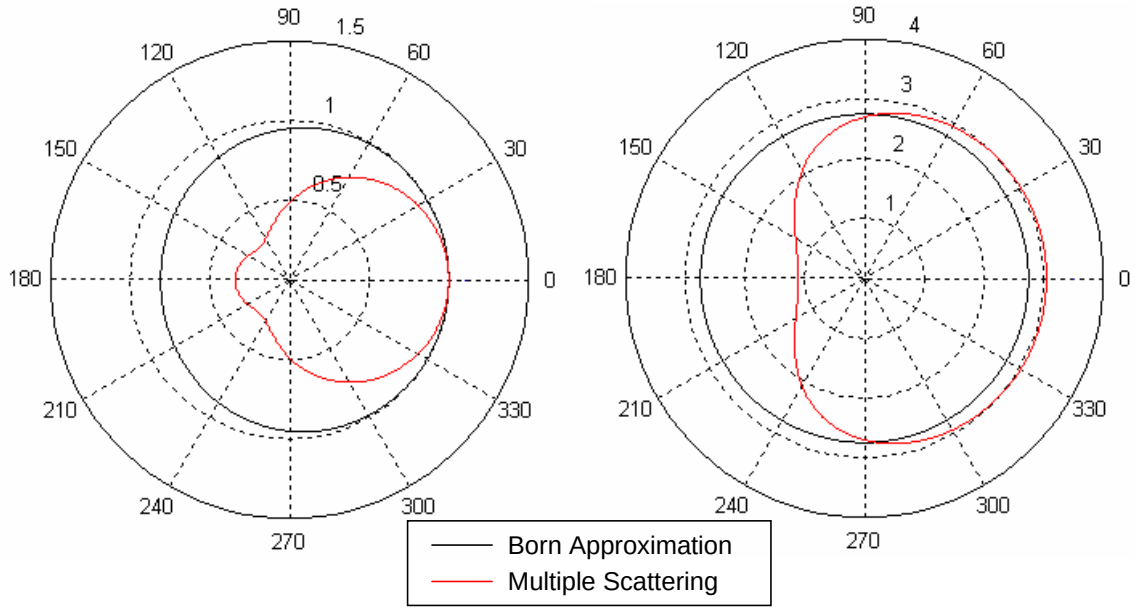

Figure 6.3: *Scattering amplitude measured for every detection angle ϕ due to an illumination angle $\theta = 0$, (a) the modulus of the scattering amplitude, (b) the phase of the scattering amplitude.*

of a monopole and a dipole. The phase of the scattering amplitude under the Born Approximation as shown in Figure 6.3 (b) is precisely that of the phase of a single point scatterer showing that the phase of the scattering amplitude under the Born Approximation does not contain any information about the presence of the two scatterers. The phase under the multiple scattering model, shown in red in Figure 6.3 (b) is dependent upon the angle of the scattered wave, implying that information on the subwavelength structure of the object is encoded in the phase when multiple scattering is considered.

6.2.2 Encoding Mechanism

Having discussed the scattering amplitude under the different physical models, this subsection will discuss the encoding of subwavelength information to the far field achieved by these models. Since it has been determined that the phase of the scattering amplitude under the Born Approximation contains no information on the subwavelength structure of the object, the information that is encoded into the

modulus of the scattering amplitude will be investigated instead. Consider the case when the angles of illumination and detection are chosen so that the frequency vector $\mathbf{\Omega} = k_0(\hat{\mathbf{r}}_\mathbf{0} - \hat{\mathbf{r}})$ spans either the Ω_x axis or the Ω_y axis in the $\mathbf{\Omega}$ domain as shown in Figure 6.1 (b). Consider first f^x which describes the scattering amplitude when $\theta = \cos^{-1}(-\Omega_x/2k_0)$ and $\phi = \pi - \theta$ meaning the frequency vector spans the Ω_x axis, then an information parameter E^x can be defined as:

$$E^x = \frac{1}{\bar{f}^x} \sup \left\{ \left| \frac{\partial f^x}{\partial \Omega_x} \right| \right\}, \tag{6.8}$$

The information parameter E^x describes the maximum gradient of f^x relative to its average amplitude given by $\bar{f}^x$ and can be thought of as estimating the information content of the scattering amplitude in the far field. A large E^x implies that it will be easier to measure fluctuations of f when there is noise present in the measured data. In a similar fashion the information parameter can also be calculated for the scattering amplitude f^y which spans the Ω_y axis, in which case $\theta = \sin^{-1}(-\Omega_y/2k_0)$ and $\phi = -\theta$. The information parameter is then given by:

$$E^y = \frac{1}{\bar{f}^y} \sup \left\{ \left| \frac{\partial f^y}{\partial \Omega_y} \right| \right\}. \tag{6.9}$$

The scattering amplitude along the Ω_x axis under the Born Approximation and Multiple Scattering models are given by:

$$f^x_{BA} = 2\tau cos(\Omega_x d/2) \approx 2\tau[1 - \frac{1}{2}(\Omega_x \frac{d}{2})^2], \tag{6.10}$$

and

$$f^x_{MS} = \frac{2\tau}{1 - \tau^2 G_0^2}[cos(\Omega_x d/2) - \tau G_0] \approx \frac{2\tau}{1 - \tau^2 G_0^2}[1 - \tau G_0 - \frac{1}{2}(\Omega_x \frac{d}{2})^2], \tag{6.11}$$

where in both equations the approximations are valid when $d \ll \lambda$. Similarly the scattering amplitudes along the Ω_y axis are:

$$f^y_{BA} = 2\tau, \tag{6.12}$$

and

$$f^y_{MS} = \frac{2\tau}{1-\tau^2 G_0^2}\{1-\tau G_0 cos[k_0 d\sqrt{}(1-\frac{\Omega_y^2}{4k_0^2})]\} \approx \frac{2\tau}{1-\tau^2 G_0^2}[1-\tau G_0+\frac{\tau G_0 k_0^2 d^2}{2}(1-\frac{\Omega_y^2}{4k_0^2})]. \tag{6.13}$$

Equations 6.10- 6.13 can then be used in order to determine the related information parameters:

$$E^x_{BA} = \frac{1}{2}k_0 d^2, \tag{6.14}$$

$$E^x_{MS} = \frac{1}{2}k_0 d^2 \frac{1}{|1-\tau G_0|}, \tag{6.15}$$

$$E^y_{BA} = 0, \tag{6.16}$$

$$E^y_{MS} = \frac{1}{2}k_0 d^2 \frac{|\tau G_0|}{|1-\tau G_0|}. \tag{6.17}$$

The information parameters E^x and E^y are larger when multiple scattering is considered than under the Born Approximation. It should also be noted that E^y_{MS} is larger than E^x_{BA} for $d < \lambda$ as shown in Figure 6.4 which compares E^y_{MS} with E^x_{BA}

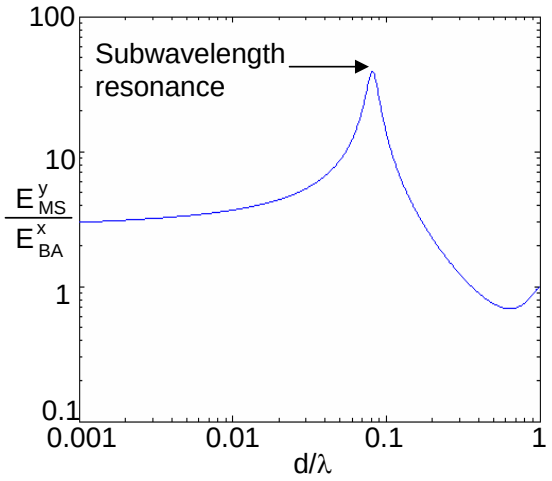

Figure 6.4: *Comparison between the information factors including the effects of multiple scattering and under the Born Approximation for different separation distances for* $\tau = 2(e^{i3\pi/4} + i)$.

relative to the separation distance between the scatterers. It should be noted that as $d \rightarrow \lambda$ the approximations in Equations 6.10- 6.13 are no longer valid which explains why the ratio is smaller than 1.

The extra content of the information parameters shows that the scattered field is enriched by inclusion of multiple scattering in the physical model. The extra information included in the information parameter under the multiple scattering model depends upon G_0 which is representative of the subwavelength interaction between the scatterers, it is this information that will make super resolution achievable in practice. It should also be noted that the maximum observed in Figure 6.4 occurs at the subwavelength resonance, thus demonstrating that multiple scattering is responsible for the encoding of the additional information. The magnitude of the information parameter implies that the physical model which includes the effects of multiple scattering should be more robust to noise as will be shown in the next section.

6.3 Inverse Problem

This section will examine the inverse problem of determining the location of the two point scatterers from the scattered field measured on the elements of an array. The aim of this section is to highlight two main results; firstly that multiple scattering improves resolution; and secondly that if the imaging model is incorrect the imaging method will not be able to reconstruct the object function correctly.

In order to prove the first result the physical model for two point scatterers will be simulated both under the Born Approximation and when multiple scattering is considered. Noise will be added to the simulated data to determine at what point the two point scatterers are no longer resolvable under the two physical models. The multistatic response matrices will be simulated as described in Chapter 5:

$$\mathbf{K_{BA}} = \mathbf{H}\mathbf{D_{BA}}\mathbf{H^T} + \mathbf{N_{0BA}}, \tag{6.18}$$

under the Born Approximation and when multiple scattering is considered:

$$\mathbf{K_{MS}} = \mathbf{H}\mathbf{D_{MS}}\mathbf{H^T} + \mathbf{N_{0MS}}. \tag{6.19}$$

The scattering matrix $\mathbf{D_{BA}}$ describes the scattering considered in the Born Approximated physical model and in this case is a (2×2) diagonal matrix whose entries are given by the scattering coefficients:

$$\mathbf{D_{BA}} = \begin{pmatrix} \tau & 0 \\ 0 & \tau \end{pmatrix}. \tag{6.20}$$

When the physical model includes the effects of multiple scattering, the scattering matrix $\mathbf{D_{MS}}$ not only contains the scattering coefficients but also describes the infinite reverberations of the scattered field between the two point scatterers:

$$\mathbf{D_{MS}} = \begin{pmatrix} \frac{\tau}{1-(\tau G_0)^2} & \frac{\tau^2 G_0}{1-(\tau G_0)^2} \\ \frac{\tau^2 G_0}{1-(\tau G_0)^2} & \frac{\tau}{1-(\tau G_0)^2} \end{pmatrix}. \tag{6.21}$$

The complex entries of the noise matrices $\mathbf{N_{0MS}}$ and $\mathbf{N_{0BA}}$ have a random Gaussian amplitude and a random phase with a uniform distribution between $[-\pi, \pi]$ as described in the previous chapter. The entries of both matrices are scaled by the variance of the noise such that:

$$\sigma_{BA} = \frac{\|\mathbf{H D_{BA} H^T}\|}{N} c_N, \tag{6.22}$$

under the Born Approximation and:

$$\sigma_{MS} = \frac{\|\mathbf{H D_{MS} H^T}\|}{N} c_N, \tag{6.23}$$

when the effects of multiple scattering are considered, so that they are comparable to the noiseless matrices of the respective physical models, the parameter c_N is then used to choose the noise level relative to the signal level. By varying the noise levels in the two physical models it will be shown that the multiple scattering physical model is more robust to noise than the same model under the Born Approximation model.

In this section, the scattered field produced by the array and point scatterer configuration shown schematically in Figure 6.5 will be considered. In this case a circular array with 36 equally spaced elements and a radius of 15λ is used to illuminate two point scatterers at the centre of the array which are separated by $\lambda/10$. The point scatterers are illuminated by an incident wave with a central frequency of $100kHz$ and the background medium has a velocity $c_0 = 1500m/s$, giving $\lambda = 0.015m$. The $\mathbf{K}$ matrix is constructed by considering the central frequency response of the recorded signals for every possible send and receive combination for the 36 array elements.

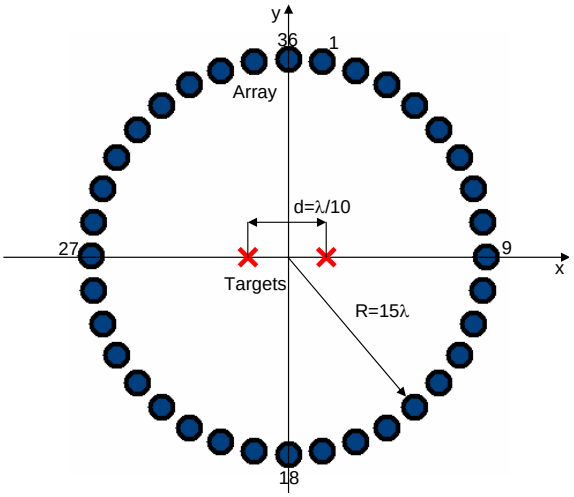

Figure 6.5: *Schematic of the array and target configuration, the array elements are equally spaced around the perimeter of a circle with a radius of* 15λ*, the point scatterers are separated by* $\lambda/10$*.*

6.3.1 Robustness to noise

In order to show that multiple scattering improves the resolution, the Factorization method will be used to process the simulated data. The advantage of this method is that its treatment of the measured scattered field is independent of the forward scattering model and so can be used to offer an unbiased comparison of the images produced under different physical models. The results from processing the simulated noiseless data for the two physical models are shown in Figure 6.6, which shows a cross section of the results produced by the Factorization method taken through the locations of both targets along the x axis (as shown in Figure 6.5). The scattered fields under both the Born Approxmation and Multiple Scattering models in this case would be distinct from those of a single point scatterer as is shown in Figure 6.3 for the continuous case. In this discrete case the measured scattered fields are still distinct from that of a single point scatterer under both models and so the location of the targets can be determined under both the Born Approximation and when multiple scattering is considered.

The effects of introducing noise to the physical models will now be investigated. The noisy data will be modeled as described by Equations 6.18 and 6.19, the Factorization

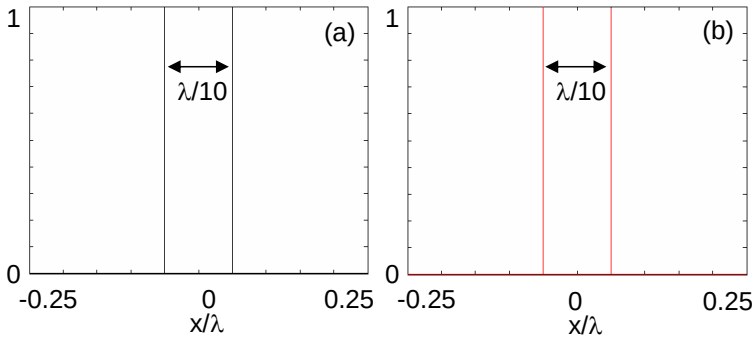

Figure 6.6: *Cross sections of the Factorization method imaging results based (a) Results based upon the Born Approximated physical model, (b) Results based upon the Multiple Scattering physical model.*

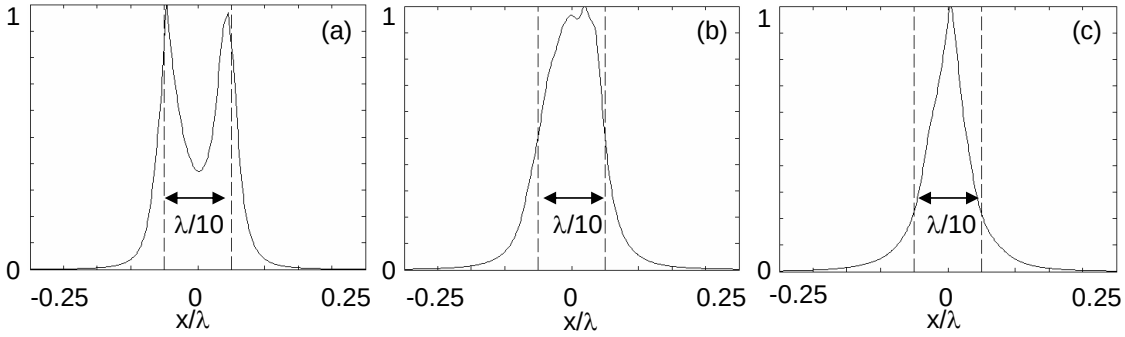

Figure 6.7: *Cross sections of the Factorization results based upon the Born Approximation model for various noise levels (a)* $c_N = 0.05$*, (b)* $c_N = 0.1$*, (c)* $c_N = 0.15$*.*

method will then be applied to the noisy data to determine whether or not the presence and location of the two point scatterers can be determined from the noisy data. Consider first of all the noisy data produced under the physical model built on the Born Approximation, in this case fifty realizations of noise were created and scaled to levels $c_N = 0.05$, $c_N = 0.1$ and $c_N = 0.15$. Each of the fifty noisy matrices were processed by the Factorization method for the different noise levels, the results were averaged over the fifty realizations and are shown in Figure 6.7. It can be seen that the targets are unresolvable for a noise level larger than $c_N = 0.1$, the resulting image tends towards that of a single point scatterer located between the two point scatterers that are present.

In a similar fashion, fifty realizations of noise were also added to the simulated data created assuming a model which accounts for the effects of multiple scattering, the

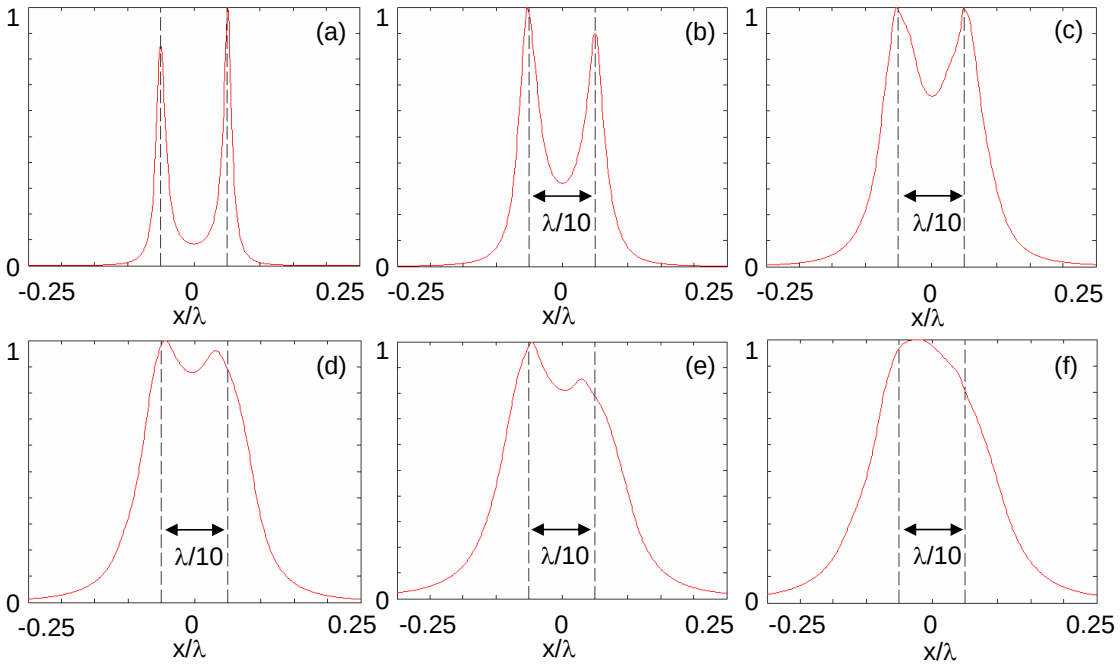

Figure 6.8: *Cross sections of the Factorization results based upon the Multiple Scattering model for various noise levels (a)* $c_N = 0.2$*, (b)* $c_N = 0.4$*, (c)* $c_N = 0.6$*, (d)* $c_N = 0.8$*, (e)* $c_N = 1$*.*

average of the results for each noise level are shown in Figure 6.8. It appears that the targets are resolvable up to a noise level of approximately $c_N = 1$ this is ten times the level achieved by the Born Approximation and implies that the multiple scattering model is much more robust to noise. This result complements those in [76] which showed that in several cases the error estimation for locating two point scatterers was lower when the effects of multiple scattering where considered than under the Born Approximation, implying that greater subwavelength information is provided by multiple scattering.

6.3.2 Importance of the correct imaging model

This section will use the Maximum Likelihood method in order to emphasize the importance of basing an imaging method upon the correct scattering model. The Maximum Likelihood method constructs simulated **K** matrices based upon all of the possible combinations of locations and scattering coefficients of the point scat-

terers in the region of interest, as such the constructed matrices can be based upon either the Born Approximation or Multiple Scattering models. Essentially using the Maximum Likelihood methods allows the effects of multiple scattering to be turned on or off in the imaging model.

It is common for imaging methods to assume a Born Approximated imaging model due to the direct link that exists between the object function and the scattered field, as shown in previous chapters. However, experimentally the physical model will contain the effects of multiple scattering, this extra information will not be accounted for by imaging methods based upon an imaging model which assumes the Born Approximation and so can lead to artifacts in the reconstructed image or a breakdown of the imaging method.

As in the previous subsection, the measured data will be simulated from the illumination of two point scatterers separated by $\lambda/10$ located at the centre of a circular 36 element array with radius 15λ as shown in Figure 6.5. Physical models will be simulated under both the Born Approximation and Multiple Scattering models for this array and object configuration. However, in this subsection it will be assumed that no noise is present in the system, as such both models produce multistatic response matrices with 2 nonzero eigenvalues and so the Maximum Likelihood method will assume the object consists of 2 point scatterers.

The Maximum Likelihood method which assumes the Born Approximated imaging model will be applied to the data obtained from the Multiple Scattering physical model (this will be referred to as Case 1). In order to speed up the processing time required it is assumed that the scattering coefficients are known and so the Maximum Likelihood method needs only to determine the location of the two point scatterers. The region of interest in this case as in the previous subsection will be given as a cross section through the location of the two scatterers ranging from $-\lambda/4$ to $\lambda/4$. The most likely coordinates are given in Table 6.1.

The relative error is defined as the difference between the predicted and actual distances of the scatterers from the origin relative to the actual distance to the origin,

-	$\mathbf{z_1}$	Relative error (%)	$\mathbf{z_2}$	Relative error (%)
Actual location	$(-\lambda/20, 0)$	N/A	$(\lambda/20,0)$	N/A
Case 1	$(-3\lambda/20, 0)$	200	$(3\lambda/20, 0)$	200
Case 2	$(-3\lambda/40, 0)$	50	$(3\lambda/40, 0)$	50

Table 6.1: Locations of the point scatterers $\mathbf{z_1}$ and $\mathbf{z_2}$ as predicted by the Maximum Likelihood method for Case 1 and Case 2.

this quantity is multiplied by 100 to give the percentages in Table 6.1. The relative errors for the most likely coordinates in Case 1 is 200% for both point targets. This example shows that even in this simple scenario, if the incorrect forward scattering model is chosen by the imaging method this will lead to incorrect results even in the absence of noise. In more complicated models when the effects of multiple scattering are more pronounced and in the presence of noise the assumption of the incorrect imaging model would lead to severe errors in reconstructed object.

In a similar fashion the data obtained using a physical model assuming the Born Approximation was applied to the Maximum Likelihood method assuming a multiple scattering imaging model (this will be referred to as Case 2), the most likely coordinates are given in Table 6.1, where the same region of interest has been used as in Case 1. The Maximum Likelihood method has failed to locate the point scatterers in this case, this again highlights that in order for the results produced by an imaging method to be valid, the correct forward scattering model must be assumed. It should be noted that Case 2 is not a physically realistic model, as although the effects of multiple scattering can be removed from the imaging model (as in Case 1) they cannot be removed from the physical model in practice. In both of these cases the assumption of the incorrect scattering model has acted as a form of noise causing the incorrect solution to be returned.

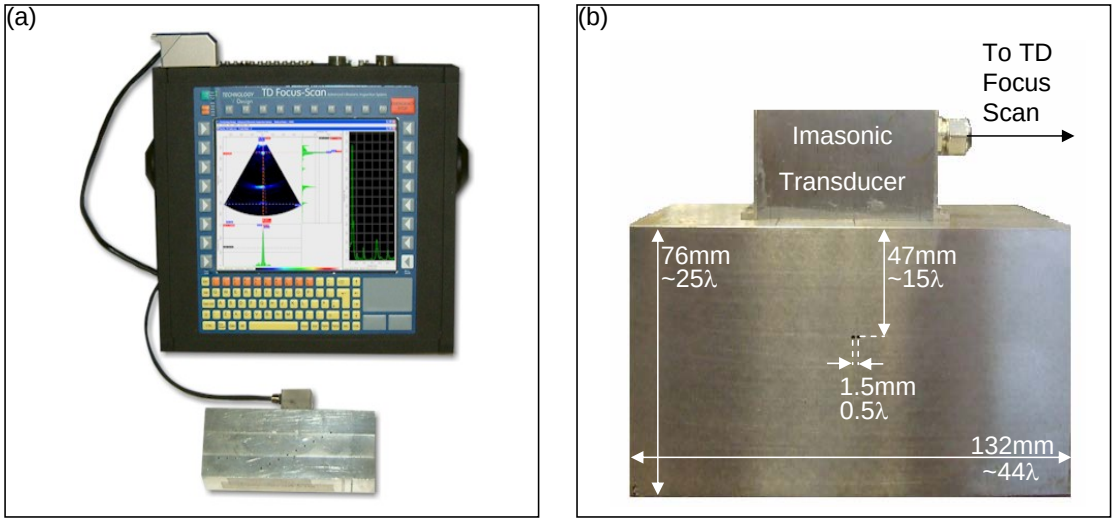

Figure 6.9: *Experimental setup for the steel block experiments (a) State-of-the-art phased array system (TD Focus Scan) which is used to illuminate the steel block and record any subsequent scattered fields, (b) Position of the transducer array relative to the geometry of the steel block.*

6.4 Experimental Results

So far this chapter has considered simulated results that would be obtained from the ideal scenario of illuminating two point scatterers with a circular array. This is a difficult scenario to recreate experimentally as objects which are only small in comparison to the wavelength instead of actual points can be created. As pointed out in previous chapters there are often cases when circular arrays cannot be used due to the geometry of the system; in this section a linear array will be used to probe two subwavelength separated point-like objects which are small in comparison to the wavelength. In this case a 32 element Imasonic transducer array with a central frequency of $2MHz$ was placed on top of a steel block with background velocity $c_0 = 5960m/s$ giving a central wavelength of $\lambda \approx 0.003m$. The steel block has two 1mm diameter holes drilled through the thickness, the centres of the holes are separated by 1.5mm which is approximately half the wavelength of the probing wave. The setup of the experiment is shown in Figure 6.9 (a). The dimensions of the steel block are shown in Figure 6.9 (b), and were chosen so that the received signals could be gated to remove the incident field and any reflections from the edges of the block.

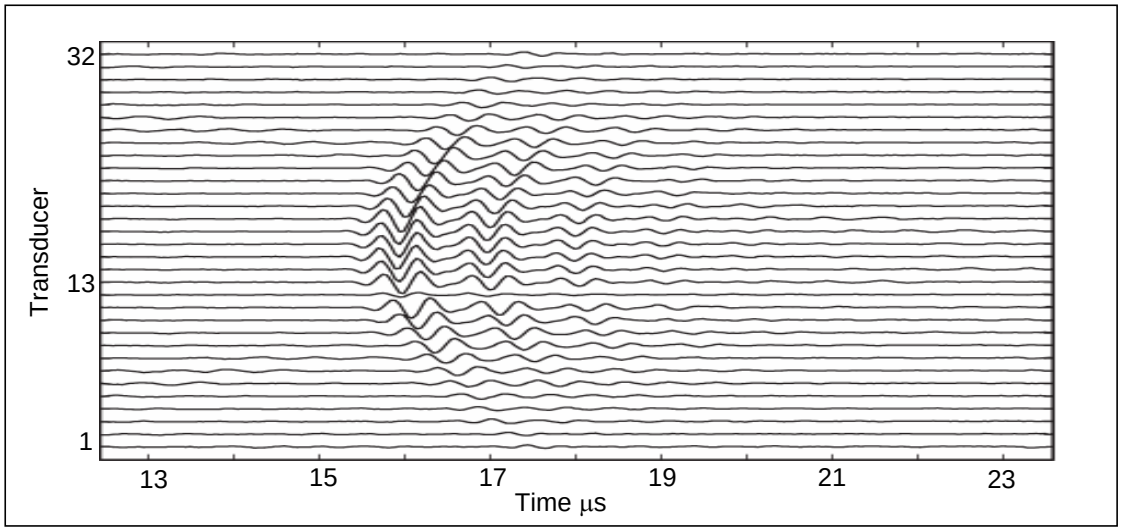

Figure 6.10: *Pulse Echo time traces recorded on the 32 elements of the Imasonic transducers for the setup shown in Figure 6.9. The time trace recorded on the* 13^{th} *element is a much lower amplitude than that of the surrounding elements.*

The Imasonic transducer array was used to excite incident fields into the specimen and receive the subsequent scattered fields, the timetraces of which were recorded via the TD Focus Scan (which is a specialized imaging computer, shown in Figure 6.9), the frequency response of this data at $2MHz$ was used to populate the **K** matrix as described in Chapter 4. The pulse echo time traces (which are those received when the send and receive transducers are identical) from each of the 32 transducers are shown in Figure 6.10. The signals on the central transducers due to the scattered field caused by the interaction of the incident field with the holes can easily be identified as arriving at about $15.5\mu s$. It should be noted that the signal on the 13^{th} transducer is much lower than its closest neighbours, it was determined that this was due to a defective transducer. No efforts were made to compensate the signals received on the 13^{th} transducer as this would aid in testing the stability of the imaging methods being used. The amplitude of the **K** matrix is shown in Figure 6.11 (a). The effects of the defective transducer can be seen as the amplitude of the 13^{th} row and column is much lower than that recorded on the surrounding elements. The amplitude of the **K** matrix can be seen as roughly symmetric as would be expected. The phase of the **K** matrix is shown in Figure 6.11 (b); it does

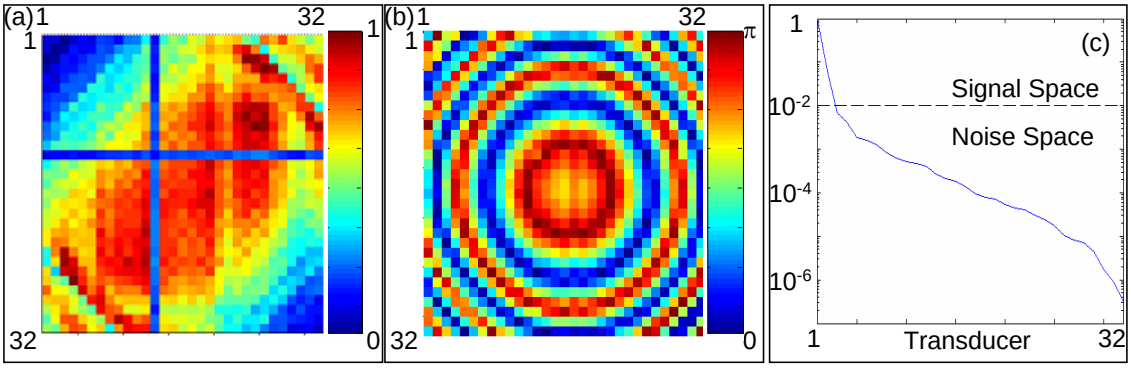

Figure 6.11: *The amplitude, phase and eigenvalues of the experimental data measured at* $2MHz$*, (a) Amplitude of the measured* $\mathbf{K}$ *matrix normalised to the maximum value, (b) Absolute value of the phase measured on the* 17^{th} *array element, (c) Eigenvalues of the measured data normalised with respect to the maximum, the distinction between the noise and signal spaces is shown by the dashed line.*

not appear that the phase has been unduly affected by the defective 13^{th} transducer. The eigenvalues of the received data are shown in Figure 6.11 (c). The signal space in this case is taken as the eigenvectors corresponding to the first two eigenvalues, giving a noise space of 30 eigenvectors.

One advantage of using the TD Focus Scan is that it has built in phased array capabilities. As discussed in Chapter 4, phased arrays focus the incident field at specified points within the medium. In this case, the array focused on a set of points which described a line bisecting the two holes, interpreting all of the scattered fields from each of the phased array configurations produces Figure 6.12 (a). This is a polychromatic image that uses the entire frequency content in the bandwidth of the received signal. The region of interest in this case was given by a two dimensional area centred on the two holes and so the results are given as a surface; the regions in red represent the most likely areas for the inhomogeneities and those in blue the least likely. The location of the two holes in Figure 6.12 are shown in white; the transducer array is located 15λ above the location of the holes but is not shown in the figure. A cross section through the centre of the two holes is shown in Figure 6.12 (b); the dashed red lines in this figure represent the edges of the holes. It can be seen from Figure 6.12 that the presence of an inhomogeneity can be determined but

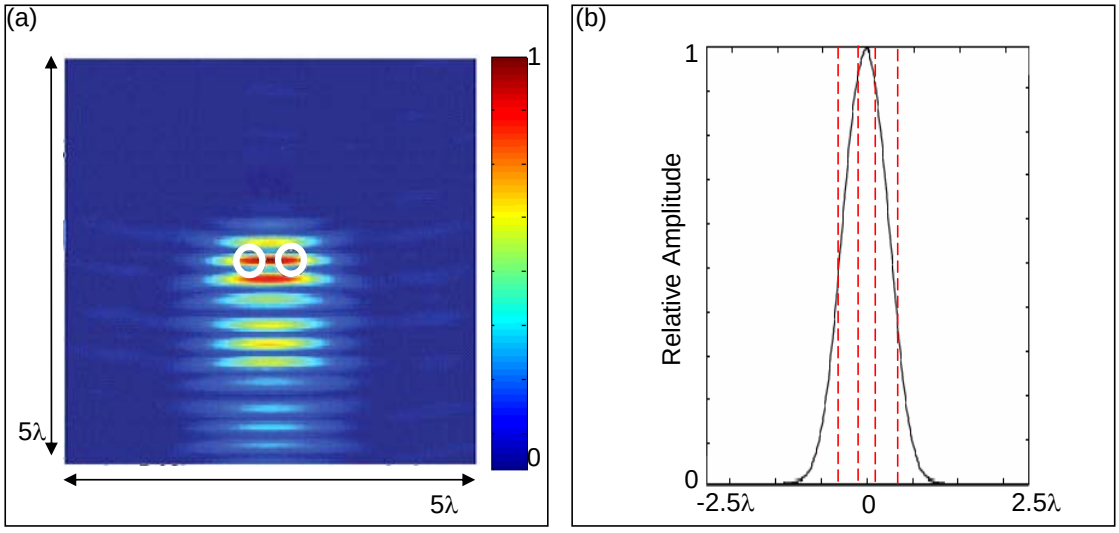

Figure 6.12: *Images produced with the TD Focus Scan using the phased array technology. (a) Surface plot of results obtained from the phased arrays, the locations of the holes in the steel block are shown in white, the array is centred with respect to the midpoint between the two holes and located* 15λ *above them as shown in Figure 6.9. (b) Cross section through the location of the holes, the extremities of the holes being shown by the red dashed lines.*

the holes themselves are not resolved. This result is consistent with the Rayleigh criterion, which in this limited view case gives a minimum resolvable distance of $1.32\lambda = 3.93mm$ as described in [87]. This is more than twice the actual distance between the holes.

Processing the experimental data from the steel specimen using the Factorization method produces the image and cross section shown in Figures 6.13 (a) and (b) respectively. The presence and location of the two point scatterers can be determined from these results. The results produced by processing the same data with the TR-MUSIC method are shown in Figures 6.13 (c) and (d) using the noise space of 30 eigenvectors indicated in Figure 6.11 (c). The TR-MUSIC method also determines the presence and location of the two holes and produces better results than those produced by the Factorization method. This is due to the choice of noise space which acts to regularize the data, effectively reducing the effects of the noise.

As a comparison to the experimental super resolved images, the conventional Bartlett imaging method was applied to the experimental data. The results for the Bartlett

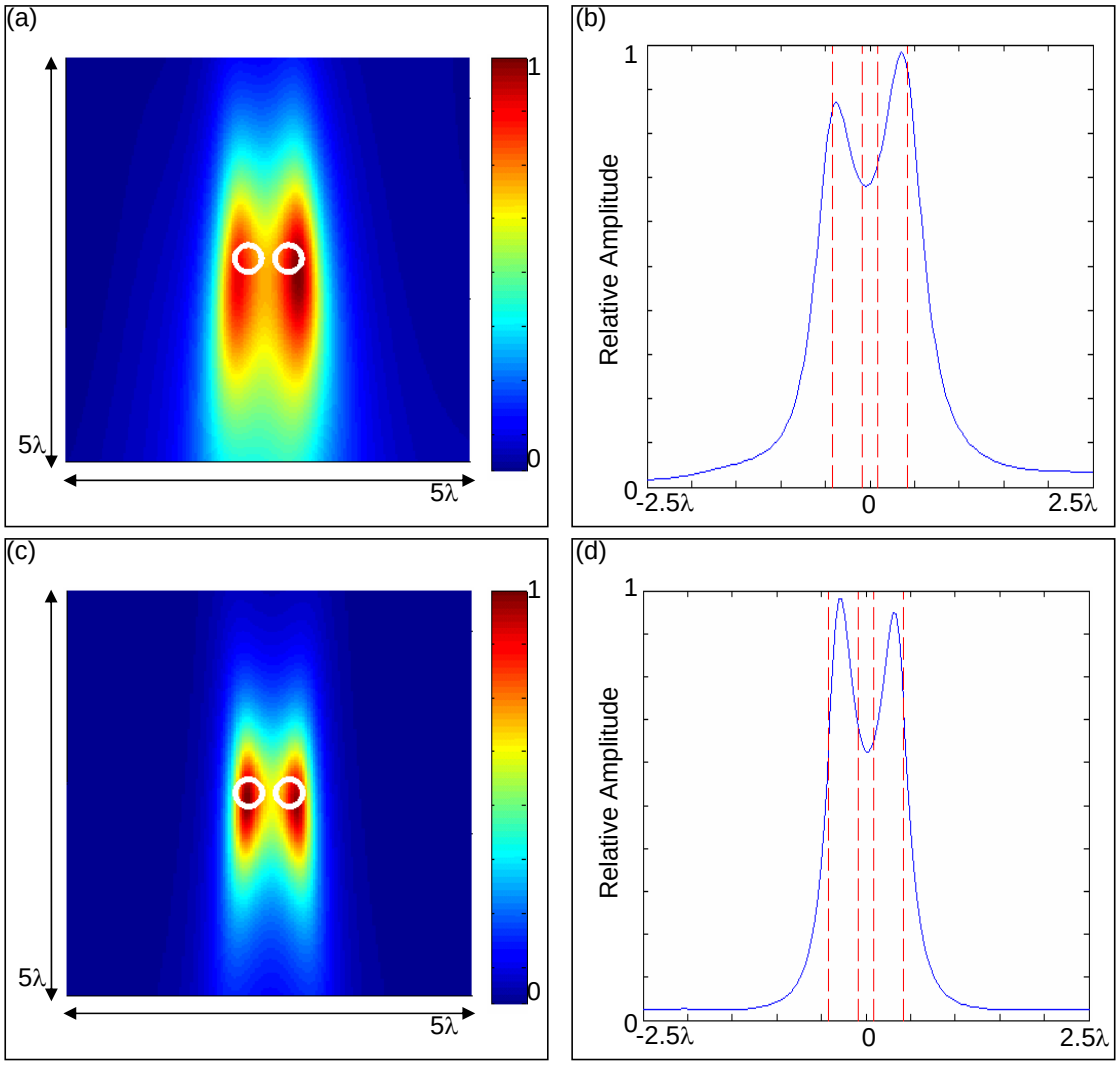

Figure 6.13: *Results of processing the multistatic response matrix measured with the setup shown in Figure 6.9. (a) Image obtained using the Factorization method, the location of the holes are shown in white, (b) Cross section of the Factorization method through the location of the drilled holes, the extremities of the holes are shown by the red dashed lines, (c) Image obtained using the Time Reversal and MUSIC method, the location of the holes are shown in white, (d) Cross section of the Time Reversal and MUSIC method through the location of the drilled holes, the extremities of the holes are shown by the red dashed lines.*

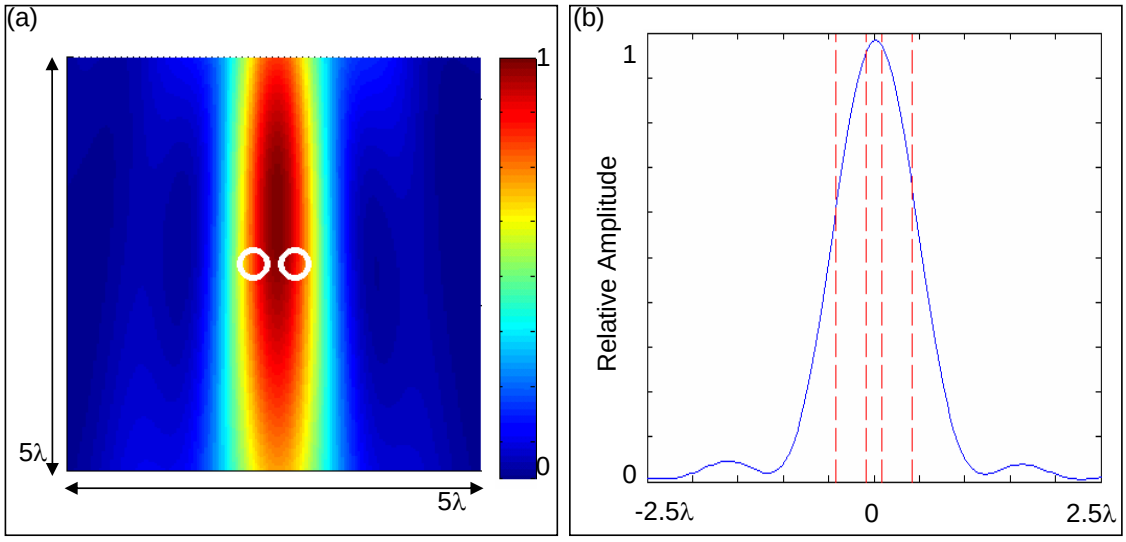

Figure 6.14: *Conventional imaging technique applied to the experimental data (a) The surface plot obtained using the Bartlett imaging method, (b) Cross section through the location of the holes using the Bartlett imaging method.*

method are shown in Figure 6.14 (a); this image is very similar to that produced when only a single point scatterer is present in the model meaning the locations of the two holes cannot be resolved from this image. It can be shown that the image shown in Figure 6.14 is equivalent to the results that would be obtained from a monochromatic phased array.

The maximum likelihood method was also applied to the experimental data, however the method failed and was unable to locate the holes in this case. This is not surprising as not only were the scattering coefficients of the holes unknown but also the fact that the objects in this case were not points but finite objects (which were only small in comparison with the wavelength) would act as a form of noise further disrupting the attempts of the Maximum Likelihood method to determine the location and nature of the inhomogeneities.

6.5 Summary

This chapter has examined the role of multiple scattering in the scattering problem resulting from the illumination of two subwavelength separated point scatterers. Although this model is not physically realistic it is a simple way of examining the scattering problem and the effects of multiple scattering. With regards to the forward scattering problem it was shown that neglecting the effects of multiple scattering led to a scattered field that was similar to that of a single point scatterer; the phase of the scattered field in this case was identical to that of a single point scatterer. However when the effects of multiple scattering were included in the physical model there was a marked difference between both the amplitude and phase of the scattered field when compared to that produced for a single point scatterer.

When considering the inverse problem it was shown that in the absence of noise super resolution was possible under both the Born Approximation and Multiple Scattering models. In the presence of noise however multiple scattering led to super resolution being achieved for a noise level approximately ten times larger than that achieved under the Born Approximation, this suggests that more information is encoded to the far field by multiple scattering.

It has also been shown that the presence of multiple scattering in the measured data can be detrimental to imaging methods which base their imaging model on the Born Approximation. The extra information encoded to the far field by multiple scattering is interpreted as a form of noise in this case. When the incorrect imaging model was used with the Maximum Likelihood method errors were produced in the simple case of the object consisting of two point scatterers, in more complicated models the effects of multiple scattering can become dominant and so the choice of imaging model becomes crucial.

These findings have been confirmed experimentally by probing a steel block with a linear array. The steel block contained two holes of subwavelength diameter and separation distance. It was shown that only the Factorization and TR-MUSIC methods could determine the location of the two targets in this case, providing

better results than the conventional imaging method and the state-of-the-art phased array technology. Importantly the results presented in this chapter demonstrate that super resolution is possible in practice.

Chapter 7

Application of Imaging methods to Extended Objects

7.1 Introduction

This chapter will demonstrate that the imaging techniques discussed previously in this thesis are still applicable when reconstructing extended objects. In order to generate the scattered field produced by the illumination of extended objects the simulation by Finite Element analysis will be introduced. Finite Element analysis is a numerical method used to simulate the response of a mechanical model to a given input. This thesis will use Finite Element analysis to simulate the scattered field resulting from the interaction of an incident field with an extended object. In order to demonstrate the accuracy of finite element analysis for this application, this chapter will include a study on how accurately the simulation can model a propagating acoustic wavefield and a scattered acoustic wavefield. Finite element analysis will then be used to simulate the scattered field resulting from the illumination of a sound soft (Dirichlet boundary conditions) square and a sound soft cylinder. The Factorization, Bartlett and TR-MUSIC imaging algorithms will be applied to this data to determine whether these methods are capable of imaging extended objects. The simulated data will then be corrupted by additive noise as described in previous

chapters to determine what effects the presence of noise has on the results produced by the imaging algorithms when processing data from extended objects.

7.2 Introduction to Finite Element Modeling

In many cases the scattered field produced by an object cannot be described analytically and so finite element analysis allows the scattered field from such objects to be investigated in the absence of noise which would be present if the scattered field was determined experimentally.

For a given mechanical system, finite element analysis creates an idealised model which consists of an assembly of elements described as a mesh, that approximates the geometry of the system under consideration see for example [88]. Each element represents a finite portion of the model and is described by the connection of a finite number of node points, each of which is a point in space. Elements are connected to each other by shared node points. The number of elements per wavelength will be denoted by E_λ and is used to describe the density of the mesh. For a static system the response at each node point to a given input is calculated as the solution to a set of simultaneous equations determined from the material properties of the elements and any boundary conditions that may be present. In the case of a dynamic system the excitation and response will be time dependent and can be described by:

$$\mathbf{F}\ddot{\mathbf{u}}(t) + \mathbf{E}\mathbf{u}(t) = \mathbf{R}(t), \tag{7.1}$$

as shown in [88], where $\mathbf{u}$ describes the displacement of the nodes and their acceleration is given by $d^2\mathbf{u}/dt^2 = \ddot{\mathbf{u}}$, $\mathbf{E}$ describes the material properties of the elements (sometimes referred to as the stiffness matrix), $\mathbf{F}$ describes the mass of the elements and $\mathbf{R}$ describes the external forces that are applied. Given the excitation $\mathbf{R}(t)$, the response of the system can be calculated for each instant in time by solving the set of simultaneous equations described by Equation 7.1.

The complexity of Equation 7.1 is determined by the number of elements used to describe the system, the greater the number of elements that are used, the greater the accuracy of the response given by Equation 7.1 at each node point should become. A classic problem in finite element analysis is to determine the minimum number of elements required to successfully describe a mechanical system. If too few elements are used then the calculated response will be inaccurate. If too many are used then the calculated response will be accurate but will require more intense computation. It should be noted that there are many commercial finite element platforms that allow the user to: generate a finite element mesh, solve the resulting simultaneous equations and view the response of the system. In this thesis the finite element software Abaqus, will be utilised for this task.

Finite element analysis will be used to generate the pressure response due to the introduction of an acoustic wavefield into a medium which contains inhomogeneities. The finite element method can be used to simulate a variety of objects by altering the material properties or boundary conditions for given elements. The resulting scattered field can then be recorded at any point within the discretised model, as such an array will be defined as a collection of node points from which the object can be illuminated and any resulting scattered field detected.

7.3 Validity of the finite element model

Having described the concept of finite element analysis in the previous section, this section will investigate the validity of using finite element analysis to model the propagation and scattering of a wavefield in an acoustic medium. In order to test the accuracy of simulations, a homogeneous finite element model will be created, and the field produced by a point source calculated. The results, will subsequently be compared to the analytical expression for a point source in a homogeneous medium. An analytical model which describes the scattered field produced when a sound soft cylinder is illuminated will be used to determine the accuracy of the scattered field produced by finite element analysis when describing the same system. If finite

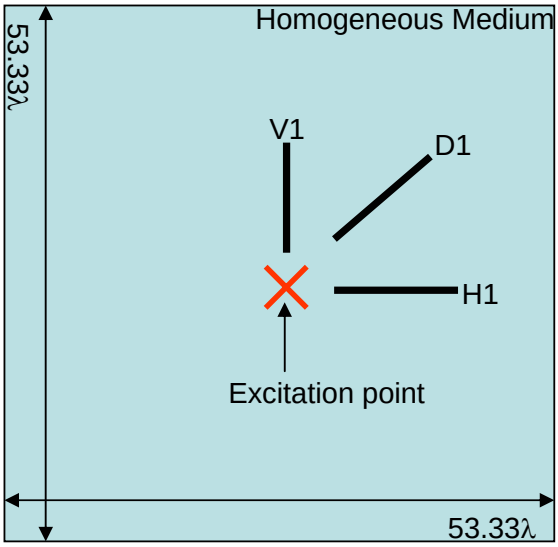

Figure 7.1: *Schematic of the finite element model used to check the accuracy of the simulation of the propagation of a wavefield.*

element analysis can successfully model the propagation and scattering of an acoustic wavefield then it will be assumed that it can be used to determine the scattered field for a variety of object and array configurations.

7.3.1 Wave propagation

A model with a relatively coarse mesh (meaning a small E_λ) and regular elements will be used to model the wave propagation. This model will be used to define the minimum mesh density that will be used in this thesis to model wave propagation. As the accuracy of the results from finite element analysis increases with the mesh density, it follows that if the wave propagation is correctly modeled with relatively coarse elements then the propagation will also correctly modeled by finer elements. Models consisting of finer elements (meaning a large E_λ) will be used in later examples in order to accurately describe the geometry of specific arrays and objects.

The finite element model in this case describes a 2-D square as shown in Figure 7.1 with the material properties of water, giving a theoretical background velocity of $c_0 = 1500m/s$. A 5 cycle Hanning toneburst with a central frequency of $100kHz$

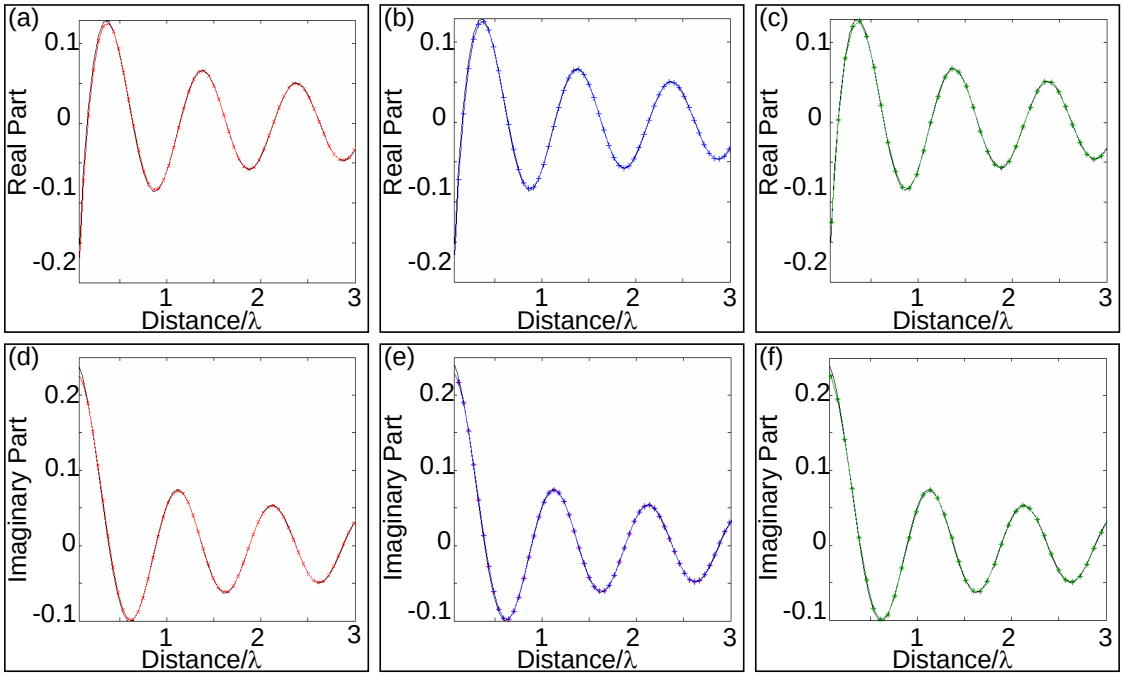

Figure 7.2: *Real and imaginary parts of the frequency response of the recorded signal at various distances measured from the excitation point. The finite element results are shown by the coloured lines in each case and the theoretical results obtained from the 2-D Green's function are shown in black. (a) The real part of the frequency response measured along the line H1. (b) The real part of the frequency response measured along the line V1. (c) The real part of the frequency response measured along the line D1. (d) The imaginary part of the frequency response measured along the line H1. (e) The imaginary part of the frequency response measured along the line V1. (f) The imaginary part of the frequency response measured along the line D1.*

was introduced into the model at a central node point (to avoid reflections from the edges) giving an interrogating wavelength of $\lambda = 0.015m$. The model was discretised into regular right angled isosceles triangular elements with $E_\lambda = 18.75$. The propagating wave resulting from the initial excitation was monitored at points along the horizontal ($H1$), vertical ($V1$) and diagonal ($D1$) lines as shown in Figure 7.1. The velocity of the propagating wavefield was determined from the arrival times of the signals and compared to the theoretical value as shown in Table 7.1. The frequency response of the recorded signals at the centre frequency was also determined and compared to the predicted frequency response (which corresponds to the 2-D Green's function as described in Chapter 2) as shown in Figure 7.2.

Monitoring Point	Velocity (m/s)	Percentage Error with respect to theoretical value
$H1$	1492.2	0.5
$V1$	1492.2	0.5
$D1$	1513.7	0.9

Table 7.1: Velocity of the simulated propagating wavefield monitored along the lines H1, V1 and D1 and the corresponding errors with respect to the theoretical value

It can be seen from Table 7.1 that the error in the velocity measured at each of the monitoring points is less than 1% of the theoretical value; this implies that the velocity of the wavefield can be regarded as being accurately modeled by the finite element analysis. The frequency responses shown in Figure 7.2 closely match the Hankel function, which describes the propagation of a wave produced by a point source in 2-D. The difference between the periods of the Hankel function and those described by the frequency responses recorded along each of the monitoring directions was less than 1.2%, implying that the propagation of the wavefield can be judged to be accurately modeled by the finite element analysis. It can be concluded from this study that a finite element model with a mesh density of $E_\lambda \geq 18.75$ can be regarded as accurately modeling the propagation of an acoustic wavefield.

7.3.2 Scattering

Having determined that finite element analysis provides a valid model for the propagation of a wave in the previous subsection, this subsection will determine whether the scattered field resulting from the interaction of a propagating wave and an object is correctly modeled by the finite element method. A finite element model will be created to simulate the scattered field resulting from the illumination of a cylinder at the centre of a circular array. An analytical expression exists for the scattered field in this case (as described in Appendix B) and will be used to determine the validity of the simulated results.

As in the previous section, the finite element model was given the material properties

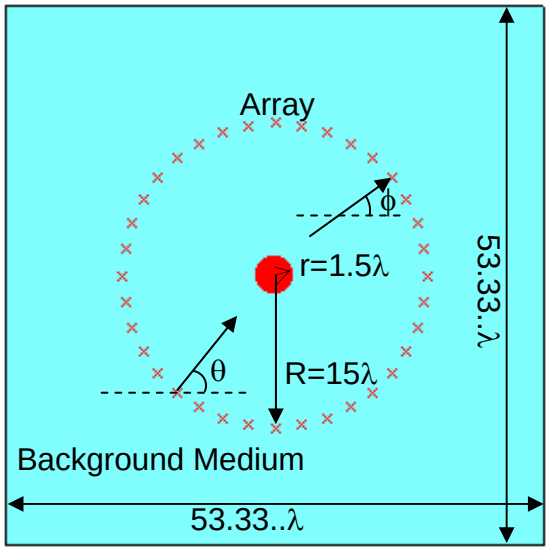

Figure 7.3: *Schematic of the finite element model used to simulate the measurements performed by a circular array (the elements of which are indicated by the crosses) when an sound soft cylinder (shown in red), is illuminated by a wavefield with a direction dictated by the angle θ, the resulting scattered field is measured at each array element, giving an angle of detection of ϕ.*

of water and a Hanning toneburst with a central frequency of $100kHz$ was used in order to illuminate the object. The array as shown in Figure 7.3 consists of 36 elements which are equally spaced on the circumference of a circle with a radius $R = 15\lambda$, the cylinder in this case was modeled to be sound soft (Dirichlet boundary conditions) and had a radius $r = 1.5\lambda$, the cylinder and the array were part of a square geometry with sides of length 53.33λ. Triangular elements with $E_\lambda \approx 30$ were used to discretise the model, the mesh was chosen so that the elements conformed to the shapes of the cylinder and the array thus providing an accurate description of the required geometry.

The scattered field resulting from the illumination of the cylinder was recorded on each of the node points that represent the array elements, the frequency response of the recorded signals was then calculated, the amplitude and phase of which are shown for every detection angle in Figure 7.4. By illuminating the cylinder from every array position, the multistatic response matrix was constructed, the eigenvalues of which are shown in Figure 7.5 (a). The results in Figures 7.4 and 7.5 (a)

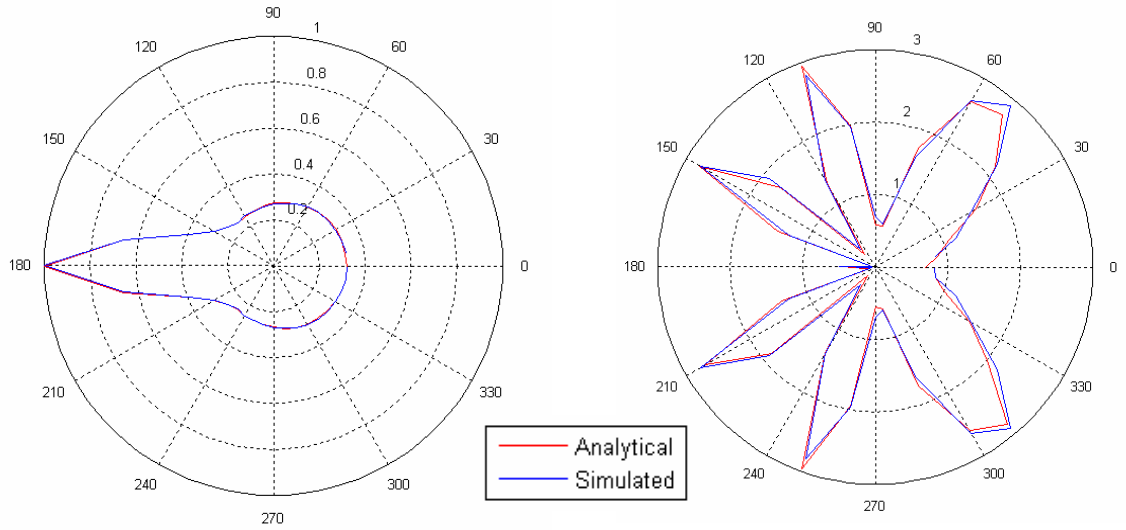

Figure 7.4: *Polar plots of the scattered field resulting from the illumination of the cylinder for each detection angle; the analytical results are shown in red and the simulated in blue. (a) The amplitude of the scattered field, (b) The phase of the scattered field.*

indicate that the finite element model produces a scattered field in this case which is extremely similar to that predicted by the analytical model, this suggests that the finite element model provides an accurate approximation of the scattered field in this case. The next section will apply imaging algorithms to the simulated scattered field for the case of an sound soft cylinder and an sound soft square, to study the performance of the imaging methods discussed in the previous chapters.

7.4 Application of Imaging Methods to Finite Element Data

The aim of this section is to apply the Factorization, TR-MUSIC and Bartlett imaging methods to the scattered fields obtained from the finite element simulations of extended objects. Two extended objects will be considered, the first will be an sound soft cylinder, and the second will be an sound soft square. In the first case the cylinder has a radius of 1.5λ producing a scattered field as discussed in the previous section. For the second case the square which is located at the centre of the array

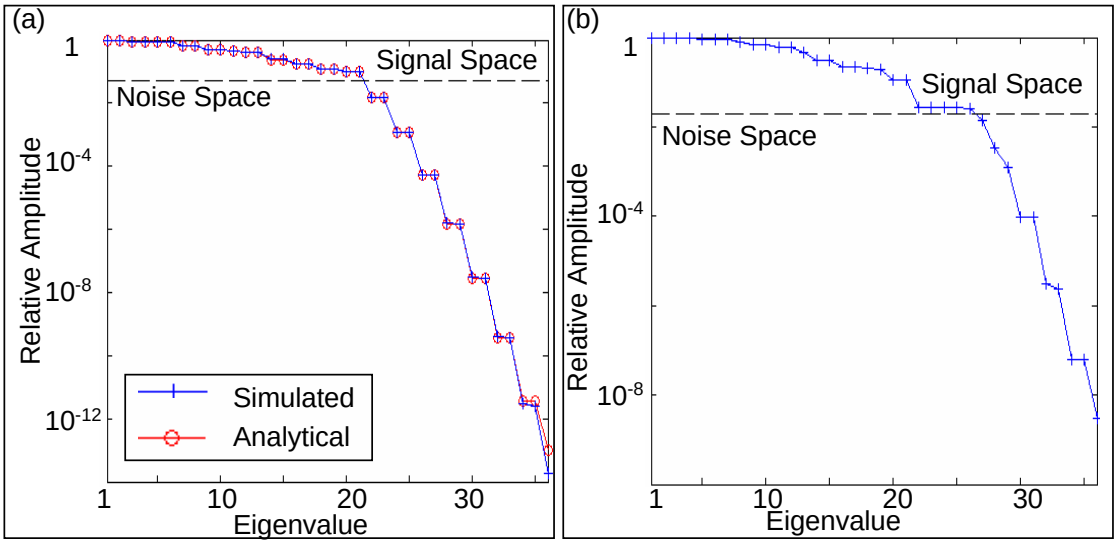

Figure 7.5: *Eigenvalues of the multistatic response matrix constructed from the scattered field resulting from the illumination of the extended objects by a 36 element circular array, (a) the eigenvalues resulting from the illumination of the sound soft cylinder; the simulated results are shown in blue and the analytical values are shown in red, (b) the eigenvalues resulting from the illumination of the sound soft cylinder.*

has a side length of 3λ, the eigenvalues of the resulting multistatic response matrix are shown in Figure 7.5 (b). In both of these cases a 36 element circular array with a radius of $R = 15\lambda$ is used to illuminate the object, which is located at the centre of the array.

As discussed in the previous section, the finite element method provides a valid approximation of the scattered field of an sound soft cylinder with $r = 1.5\lambda$. The results from processing the simulated scattered field in this case are shown in Figure 7.6 and the results from processing the scattered field from the case of the sound soft square are shown in Figure 7.7. The results produced by the Factorization method for the case of the sound soft cylinder (shown in Figure 7.6 (a) and (d)) provide a strong indication of the location of the object. It can be seen from the cross section that the Factorization method rapidly becomes non-zero at the boundary of the cylinder meaning that the shape, size and location of the object can be easily determined from these results. The results shown in Figures 7.7 (a) and (d) demonstrate that the Factorization method is also successful when applied to the

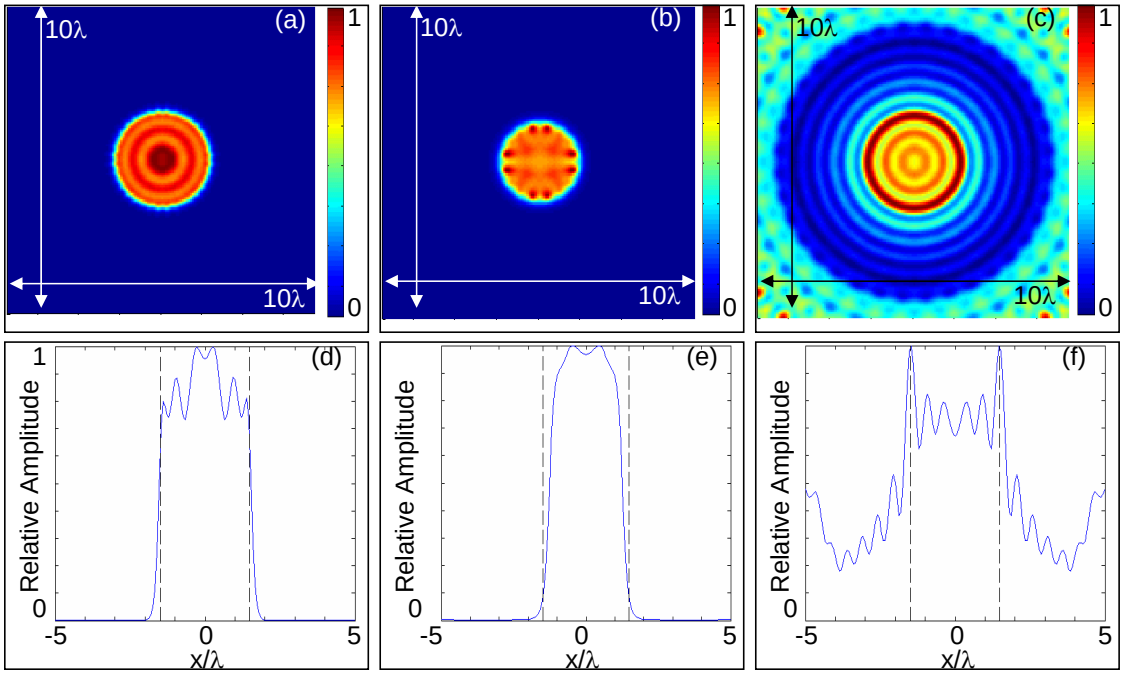

Figure 7.6: *Reconstruction of the sound soft cylinder based upon the scattered field generated via finite element analysis. (a) Surface reconstruction using the Factorization method (b) Surface reconstruction using the TR-MUSIC method (c) Surface reconstruction using the Bartlett method, the corresponding cross sections through the centre of the cylinder for figures (a)-(c) are shown in (d)-(f) with the boundary of the cylinder shown by the dashed lines.*

case of the sound soft square, as in the case of the cylinder, the results rapidly increase at the boundary of the square providing an obvious indication of the shape, size and location of the object.

Before processing the simulated scattered fields with the TR-MUSIC method it is necessary to determine the eigenvectors that would make up the noise and signal spaces from the eigenvalues of the multistatic response matrices. In the case of point scatterers the signal space was determined by the eigenvectors corresponding to the non-zero eigenvalues, however in the case of finite objects, all of the eigenvalues are non-zero and so a different strategy to determine the noise and signal spaces is required. It is by examining the structure of the eigenvalues that the signal and noise spaces can be determined in these cases. The eigenvalues of the multistatic response matrix obtained from the scattered field of the cylinder are shown in Figure 7.5

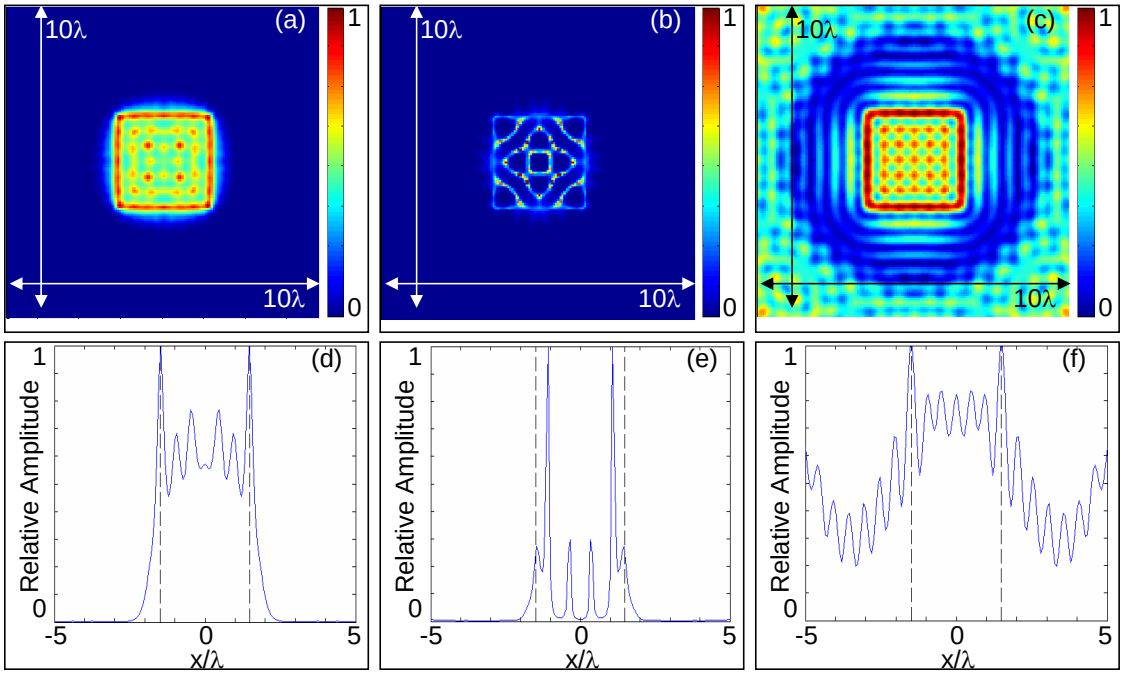

Figure 7.7: *Reconstruction of the sound soft square based upon the scattered field generated via finite element analysis. (a) Surface reconstruction using the Factorization method (b) Surface reconstruction using the TR-MUSIC method (c) Surface reconstruction using the Bartlett method, the corresponding cross sections through the centre of the square for figures (a)-(c) are shown in (d)-(f) with the boundary of the square shown by the dashed lines.*

(a). It can be seen that the amplitude of the first 21 eigenvalues decrease roughly linearly (with respect to the log scale), after the 21^{st} eigenvalue the amplitude of the remaining eigenvalues rapidly decreases. All of the eigenvalues up to the point at which the amplitude rapidly decreases are taken as defining the signal space which is populated by the corresponding eigenvectors, the remaining eigenvectors are used to populate the noise space. Examining the structure of the eigenvalues corresponding to the sound soft square as shown in Figure 7.5 (b), the signal space is constructed from the eigenvectors corresponding to the first 26 eigenvalues and the noise space consists of the remaining 10 eigenvectors, using the same arguments as in the case of the cylinder.

The results of applying the TR-MUSIC method to the simulated scattered field for the case of the sound soft cylinder are shown in Figure 7.6 (b) and (e), from which it

can be seen that as in the case of the Factorization method there is a rapid increase in the results produced by TR-MUSIC at the boundary of the cylinder meaning that the object is successfully reconstructed. Similarly the object can be correctly determined from the scattered field resulting from the sound soft square as shown in Figure 7.7 (b) and (e).

The results produced by applying the Bartlett beamforming method to the simulated scattered fields produced by the illumination of the sound soft cylinder and square are shown in Figures 7.6 and 7.7. Although the boundary of the cylinder and the square are identifiable from the results produced by the Bartlett method there are significant sidelobes present in both cases, meaning these results are not as 'clean' as those produced by the Factorization and TR-MUSIC methods. As such if other objects were present in the neighbourhood of the cylinder or the square, their presence could be lost in the sidelobes when using the Bartlett method.

This section has demonstrated that each of the imaging methods under consideration can successfully determine the shape, size and location of the sound soft cylinder and square from the information encoded in their respective simulated scattered fields. The next subsection will investigate how robust these results are to the effects of noise.

7.4.1 Robustness to Noise

The scattered fields that were processed in the previous subsection can essentially be regarded as noiseless, under experimental conditions however the scattered fields would contain the effects of random noise. This subsection will introduce additive noise to the simulated scattered fields produced by the illumination of the square and the cylinder to determine if objects in either case can still be successfully reconstructed from the noise corrupted scattered fields.

As in Chapters 5 and 6, the (36×36) multistatic response matrices, which describe the scattered fields for the respective objects, will be corrupted by the addition of a (36×36) complex random noise matrix $\mathbf{N_0}$ which is scaled by the constant c_N

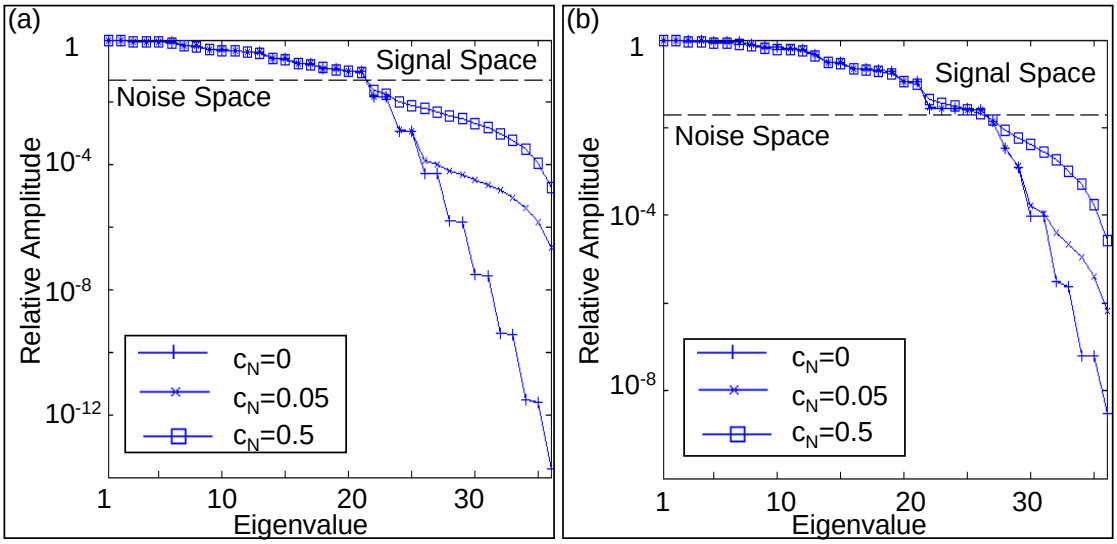

Figure 7.8: *Eigenvalues of the scattered field for various noise levels (a) The eigenvalues for sound soft cylinder, (b) The eigenvalues for the sound soft square.*

so that it is of a comparable level to the noiseless matrix. As in Chapter 6, several realizations of noise will be considered as the results from a single random realization of noise will not be representative of the effects of noise for a given c_N. In this case, 50 realizations of random noise were created, each of the realizations were scaled and added to the required multistatic response matrix. In this Chapter two separate noise levels will be considered; a relatively low level of $c_N = 0.05$, and a relatively high level of $c_N = 0.5$, unlike the study in the previous chapter, the resolution of the image is not being tested (since there is only a single object present). The average eigenvalues of the multistatic response matrices are shown in Figure 7.8 for both objects and for both levels of noise.

The average of the results produced by the imaging algorithms when a noise level of $c_N = 0.05$ is introduced into the scattered field produced by the sound soft cylinder and square are shown in Figures 7.9 and 7.10 respectively. The results for a noise level of $c_N = 0.5$ are shown in Figure 7.11 and 7.12. It can be observed that the introduction of noise with $c_N = 0.05$ has only had a slight effect on the results produced by the Factorization method, causing the estimated width of the cylinder to be slightly broadened, however the object can still be considered to have been successfully reconstructed from these results. It can be seen from Figure 7.11 (a)

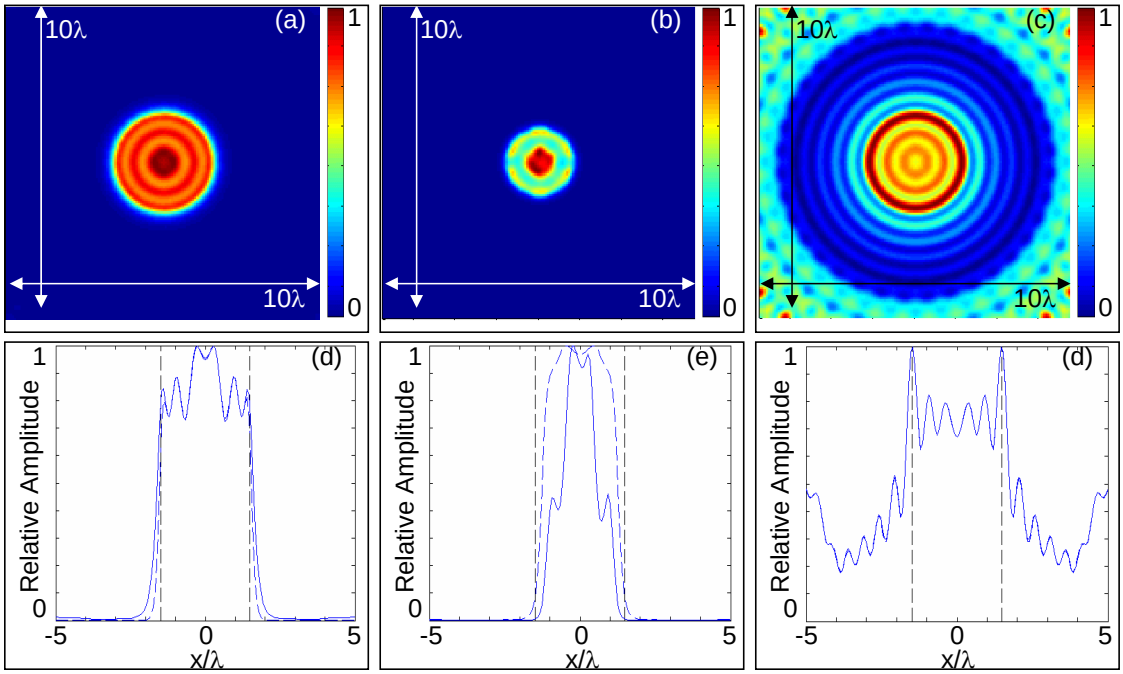

Figure 7.9: *Average of the reconstructions of the sound soft cylinder based upon the scattered field generated via finite element analysis corrupted with a noise level* $c_N = 0.05$ *(a) Surface reconstruction using the Factorization method (b) Surface reconstruction using the TR-MUSIC method (c) Surface reconstruction using the Bartlett method, the corresponding cross sections through the centre of the cylinder for figures (a)-(c) are shown in (d)-(f) with the boundary of the cylinder shown by the black dashed lines and the noiseless case shown by the blue dashed lines.*

and (d) that when the noise level is increased to $c_N = 0.5$ it has a more significant effect on the results produced by the Factorization method. The noise in this case has once again caused a broadening of the estimated width of the cylinder and has also meant that the results corresponding to areas outside the cylinder are now non-zero. Even with this high level of additive noise however, the cylinder is reconstructed successfully by the Factorization method. Similar results are observed when the Factorization method is applied to the noise corrupted data obtained from the sound soft square as shown in Figures 7.10 and 7.12. In both of these cases the square can be considered to have been successfully reconstructed by the imaging algorithm. The introduction of noise however, has caused the contrast between the area that represents the square and that which represents the background medium to

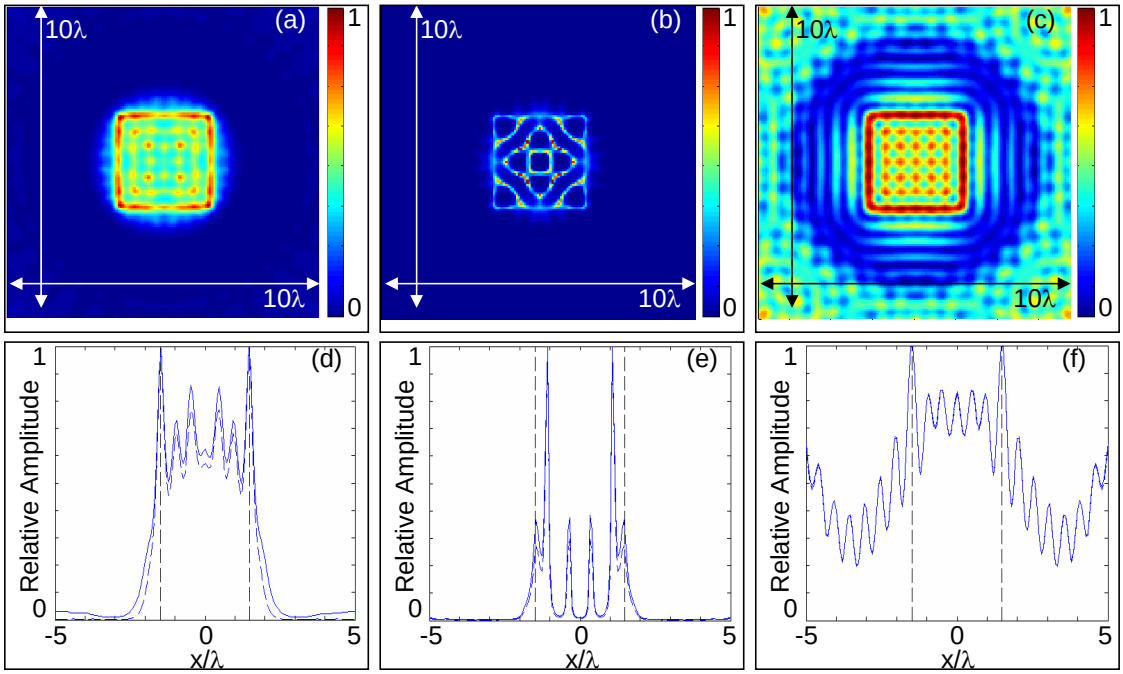

Figure 7.10: *Average of the reconstructions of the sound soft square based upon the scattered field generated via finite element analysis corrupted with a noise level* $c_N = 0.05$ *(a) Surface reconstruction using the Factorization method (b) Surface reconstruction using the TR-MUSIC method (c) Surface reconstruction using the Bartlett method, the corresponding cross sections through the centre of the square for figures (a)-(c) are shown in (d)-(f) with the boundary of the square shown by the black dashed lines and the noiseless case shown by the blue dashed lines.*

be less distinctive, this is most obvious when the higher level of noise is considered.

In order to process the noisy multistatic response matrices using the TR-MUSIC method, the structure of their eigenvalues as shown in Figure 7.8 must be considered. For both levels of noise and for both the cylinder and square models it can be seen that the eigenvalues follow the structure of the noiseless eigenvalues up to a certain point after which they diverge. This implies that the introduction of noise has a greater relative effect on the eigenvalues with lower amplitudes. Since the structure is similar to that of the noiseless case, the signal spaces are defined as consisting of the eigenvectors that relate to the first 21 eigenvalues and the first 26 eigenvalues for the cylinder and square spaces respectively, and the noise spaces consist of the remaining eigenvectors, for each of the 50 noise realizations.

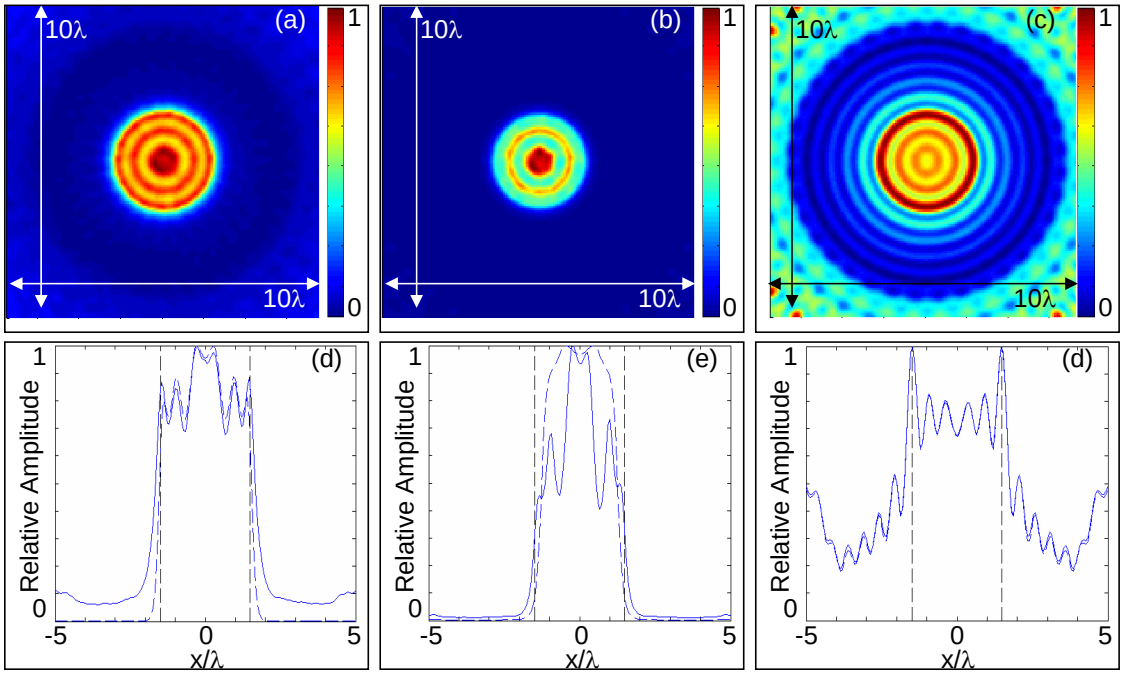

Figure 7.11: *Average of the reconstructions of the sound soft cylinder based upon the scattered field generated via finite element analysis corrupted with a noise level* $c_N = 0.5$ *(a) Surface reconstruction using the Factorization method (b) Surface reconstruction using the TR-MUSIC method (c) Surface reconstruction using the Bartlett method, the corresponding cross sections through the centre of the cylinder for figures (a)-(c) are shown in (d)-(f) with the boundary of the cylinder shown by the black dashed lines and the noiseless case shown by the blue dashed lines.*

The averaged results for the case of TR-MUSIC being applied to the noisy data obtained from the illumination of the cylinder are shown in Figure 7.9 for the case of $c_N = 0.05$ and Figure 7.11 for the case of $c_N = 0.5$. It can be seen from these noisy images, that the results produced by the TR-MUSIC method have been significantly affected by the introduction of noise, however the cylinder can still be successfully estimated from both cases. In the case of the sound soft square, it can be seen from Figure 7.10 (b) and (e) that the introduction of noise with $c_N = 0.05$ has only had a slight effect on the results produced by the TR-MUSIC method, meaning the square can be successfully reconstructed. From Figure 7.12 (b) and (e), it can be seen that the introduction of noise with $c_N = 0.5$ has had a more significant effect on the results produced by the TR-MUSIC method, however the square can

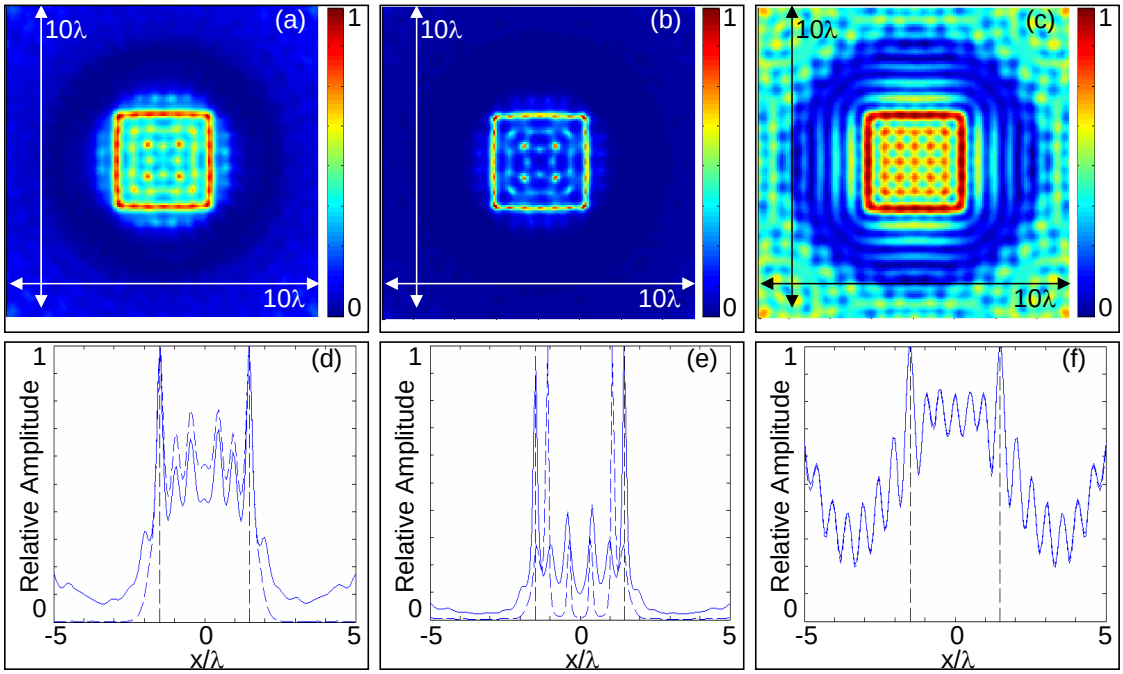

Figure 7.12: *Average of the reconstructions of the sound soft square based upon the scattered field generated via finite element analysis corrupted with a noise level* $c_N = 0.5$ *(a) Surface reconstruction using the Factorization method (b) Surface reconstruction using the TR-MUSIC method (c) Surface reconstruction using the Bartlett method, the corresponding cross sections through the centre of the square for figures (a)-(c) are shown in (d)-(f) with the boundary of the square shown by the black dashed lines and the noiseless case shown by the blue dashed lines.*

still be considered to have been successfully reconstructed. In a similar fashion to the results produced by the Factorization method, the contrast between the area of the object and that of the background medium in the results produced by the TR-MUSIC method are less distinctive when noise is introduced, for both the square and the cylinder.

The results produced by the Bartlett method for the sound soft cylinder (Figure 7.9 (c) and (f) and Figure 7.11 (c) and (f)) show very little sensitivity to the level of noise inroduced to the system as both results are very similar to those produced in the noiseless case. Similar results are obtained when noise is introduced to the case of the sound soft square (shown in Figure 7.10 (c) and (f) and Figure 7.12 (c) and (f)) where the introduction of noise with levels of $c_N = 0.05$ and $c_N = 0.5$

respectively has had little effect on the results produced by the Bartlett method when compared to the noiseless system.

7.5 Summary

This chapter has introduced the use of finite element analysis as a method for simulating the scattered field for extended objects. It was shown by considering the velocity and propagation of an acoustic wave, that finite element analysis could be considered as a valid method for simulating a propagating wave. It was also determined by considering the analytical model that describes the scattered field for the case of a sound soft cylinder that the scattered acoustic field can also be successfully modeled by finite element analysis. The finite element model was then used to generate the scattered fields for the case of a circular array illuminating an sound soft square and cylinder, imaging algorithms were applied to the resulting scattered fields. The Factorization and TR-MUSIC method reconstructed the objects successfully. Although the object was identifiable in the results produced by the Bartlett method, the presence of strong sidelobes means that the contrast between the background and the object is not as strong in this case. The results produced when the simulated data was corrupted by noise, indicate that an extended object can be reconstructed even in the presence of quite a high level of noise distortion, each imaging algorithm was still able to reconstruct the objects with $c_N = 0.5$. This chapter has shown that the TR-MUSIC and Bartlett imaging algorithms which were derived in Chapter 5 for the case of point scatterers can successfully be applied to the scattered fields produced by the illumination of extended objects and that finite element analysis is a valid tool to simulate the scattered fields in this case. The next chapter will examine the scattered field produced by subwavelength extended objects in order to determine if super resolution is possible in this case and will examine the validity of using finite element analysis for this scenario.

Chapter 8

Demonstration of super resolution for extended objects

8.1 Introduction

The aim of this chapter is to demonstrate that super resolution can be achieved when considering extended objects. Chapter 6 showed that super resolution was achievable in the case of point scatterers, however, prior knowledge about the point-like nature of the scatterers was used in this case. This chapter will demonstrate that super resolution is achievable without any prior knowledge of the object. Chapter 7 has shown that imaging techniques can be successfully applied to reconstruct extended objects which are larger than the interrogating wavelength; it will be shown in this chapter that subwavelength extended objects can still be successfully reconstructed.

This chapter will employ a semi-analytical model to generate the scattered field produced by the illumination of two subwavelength separated cylinders each with a subwavelength radius. This model will allow the scattered field to be generated under the Born Approximation and when multiple scattering is considered. As in Chapter 6 the robustness to noise of the two models will be tested, and it will be demonstrated that the inclusion of multiple scattering within the forward scattering model allows super resolution to be achieved at higher noise levels than under the

Born Approximation.

Finally in this chapter the semi-analytical results will be compared to the results obtained from finite element analysis. It will be shown that the finite element analysis does not appear to correctly model scattering at the subwavelength scale, which leads to errors in any reconstructions based upon the simulated scattered field. It will be argued that these errors are due to problems in simulating the multiple scattering of evanescent waves, this will be demonstrated by considering a finite element simulation of Frustrated Total Internal Reflection.

8.2 Forward Problem

This section will use a semi-analytical model to investigate the forward scattering problem of a circular array illuminating two cylinders located at its centre, as shown in Figure 8.1 (a). It will be shown that there is a significant difference between the scattered fields produced by the Born Approximation and Multiple Scattering models. The solutions to the forward scattering problem under the two physical models will be used as part of the inverse scattering problem in the next section to determine if the cylinders can be successfully reconstructed from the scattered field.

In the previous chapter the analytical solution to the forward scattering problem for a single cylinder was employed to verify the validity of the finite element model. For the case of two cylinders (shown schematically in Figure 8.1 (a)) there is no analytical solution to describe the scattered field due to a lack of rotational symmetry. There is however a semi-analytical model as described in [86] which can be used in order to give a valid approximation of the scattered field:

$$\psi_s = \sum_{n=-n_{max}}^{n_{max}} A_n^1 H_n(k_0 r_1) e^{in\phi_1} + A_n^2 H_n(k_0 r_2) e^{in\phi_2}, \tag{8.1}$$

where ϕ_1 and R_1 are the angle and distance respectively of the observation point from the centre of the first cylinder as shown in Figure 8.1 (b). In a similar fashion

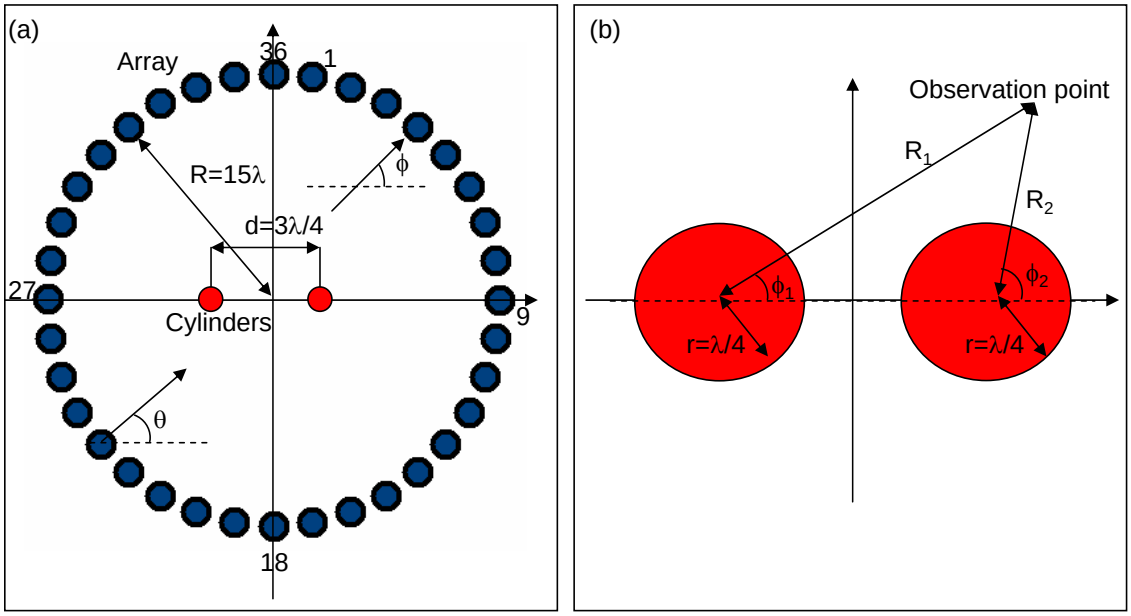

Figure 8.1: *Schematic of the array and object configuration. (a) The* 36 *array elements are equally spaced around the perimeter of a circle with a radius of* 15λ*, the two cylinders are located at the centre of the array, the centres of the two cylinders are separated by* $3\lambda/4$*. The object is illuminated by a wavefield traveling in the direction given by the angle of incidence* θ*. (b) The two cylinders at the centre of the array both have a radius of* $\lambda/4$*. The angle of observation,* ϕ_1*, and the distance* R_1 *are measured with respect to the centre of the first cylinder, similarly* ϕ_2 *and* R_2 *are given with respect to the centre of the second cylinder.*

ϕ_2 and R_2 are measured with respect to the centre of the second cylinder. The scattering at the cylinders is considered at $2n_{max}+1$ equally spaced points on each of the cylinders' circumference, an exact solution for the scattered field would require $n_{max} \to \infty$. However, as will be described below, the coefficients A_n^1 and A_n^2 rely upon the inversion of an $(4n_{max}+2) \times (4n_{max}+2)$ matrix $\mathbf{M}$ which can become singular as the value of n_{max} increases. The unknown coefficients A_n^1 and A_n^2 are determined by the $4n_{max}+2$ entries of the vector $\mathbf{a}$, the first $2n_{max}+1$ entries of which describe the coefficients A_n^1, the remaining entries describe A_n^2. For sound soft cylinders $\mathbf{a}$ is given by:

$$|\mathbf{a}\rangle = \mathbf{M^{-1}}|\mathbf{b}\rangle, \tag{8.2}$$

where $\mathbf{b}$ is a vector with $(4n_{max}+2)$ entries, the first $(2n_{max}+1)$ entries of which describe the incident field at the $(2n_{max}+1)$ points that describe the first cylinder, the remaining $(2n_{max}+1)$ entries describe the incident field at the $(2n_{max}+1)$ points that describe the second cylinder. The matrix $\mathbf{M}$ (the inverse of which is used in Equation 8.2) relates to the scattering caused by the cylinders. This matrix can be described by four quadrants $\mathbf{M_1}, \mathbf{M_2}, \mathbf{M_3}, \mathbf{M_4}$ each of which is made up of $(2n_{max}+1)$ rows and columns as shown below:

$$\mathbf{M} = \begin{pmatrix} \mathbf{M_1} & \mathbf{M_3} \\ \mathbf{M_2} & \mathbf{M_4}. \end{pmatrix} \tag{8.3}$$

The quadrants $\mathbf{M_1}$ and $\mathbf{M_4}$ describe the scattering at the first and second cylinders respectively when they are considered in seclusion. The quadrant $\mathbf{M_1}$ is independent of the whether or not the Born Approximation or Multiple Scattering models are used to describe the scattered field, the $(k,j)^{th}$ entry of this quadrant is given by:

$$\mathbf{M_1}(k,j) = H_{j-(n_{max}+1)}(k_0 r) e^{\{[j-(n_{max}+1)][2\pi/(2n_{max}+1)]k\}}, \tag{8.4}$$

where r is the radius of the first cylinder. In a similar fashion the $(k,j)^{th}$ entry of $\mathbf{M_4}$ is given by:

$$\mathbf{M_4}(k,j) = H_{j-(n_{max}+1)}(k_0 r) e^{\{[j-(n_{max}+1)][\pi+2\pi/(2n_{max}+1)]k\}}. \tag{8.5}$$

The quadrant $\mathbf{M_2}$ describes the scattering at the first cylinder due to the presence of the second cylinder, similarly the quadrant $\mathbf{M_3}$ describes the scattering at the second cylinder due to the presence of the first cylinder. Under the Born Approximation the entries of the quadrants $\mathbf{M_2}$ and $\mathbf{M_3}$ are all equal to 0, since the interaction between the scattered field and the cylinders is not considered. In order to describe the entries of these quadrants under the Multiple Scattering model consider the $(2n_{max}+1)\times 1$

column vector $\mathbf{r_{12}}$, the entries of which describe the distance between the centre of the first cylinder and the $(2n_{max}+1)$ points that describe the points on the circumference of the second cylinder; the corresponding angles are recorded in the vector $\theta_{\mathbf{12}}$, in which case the $(j,k)^{th}$ entry of the quadrant $\mathbf{M_2}$ is given by:

$$\mathbf{M_2}(k,j) = H_{j-(n_{max}+1)}(k_0\mathbf{r_{12}}(k))e^{\{[j-(n_{max}+1)]\theta_{\mathbf{12}}(k)\}}, \tag{8.6}$$

similarly the $(k,j)^{th}$ entry of the third quadrant is given by:

$$\mathbf{M_3}(k,j) = H_{j-(n_{max}+1)}(k_0\mathbf{r_{21}}(k))e^{\{[j-(n_{max}+1)]\theta_{\mathbf{21}}(k)\}}, \tag{8.7}$$

where $\mathbf{r_{21}}$ describes the distance between the centre of the second cylinder and the points that make up the circumference of the first cylinder and $\theta_{\mathbf{21}}$ are the corresponding angles. Once the entries of the four quadrants have been determined the $\mathbf{M}$ matrix can be constructed and the inverse (if it exists) can be calculated to determine the coefficients A_n^1 and A_n^2 in Equation 8.2 under either the Born Approximation or Multiple Scattering models. It was shown in [86] that an accurate scattered field could be generated with n_{max} as small as 5; this thesis will use $n_{max} = 16$ which offers a high level of accuracy, and it has been observed that the matrix $\mathbf{M}$ does not become singular for the cases considered.

The amplitude and phase of the scattered field resulting from the interaction of an incident wave with two cylinders both with a radius $r = \lambda/4$, whose centres are separated by $3\lambda/4$ is shown in Figure 8.2. As in the case of the two point scatterers presented in Chapter 6, there is a marked difference between amplitude and phase of the scattered field under the two physical models. In contrast with the case of two point scatterers the amplitude and phase of both models are more complicated. Under the Born Approximation the amplitude and phase of the scattered field is dependent upon the angle of the scattered wave; this angular dependence is due to the finite size of the objects and the larger overall size relative to λ. The amplitude

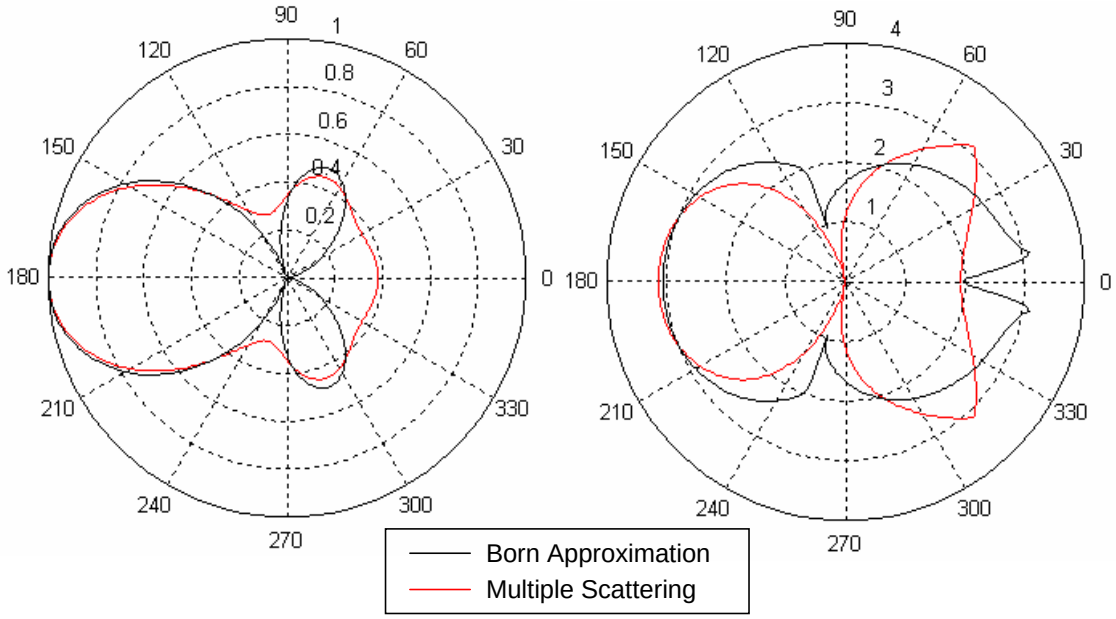

Figure 8.2: *Scattering amplitude of two cylinders for every detection angle ϕ due to an illumination angle $\theta = \pi$, shown for both the Born Approximation and Multiple Scattering physical models, (a) the modulus of the scattering amplitude, (b) the phase of the scattering amplitude.*

and phase of the scattered field, under the Multiple Scattering model, are also both dependent upon the angle of detection. The difference between the two scattering patterns is due to multiple scattering. In particular the multiple scattering of evanescent waves (in addition to propagating waves) which should encode subwavelength information to the far field. The next section will use the Factorization method to solve the inverse scattering problem based upon the scattered fields derived in this section.

8.3 Inverse Problem

This section will determine whether the presence of two subwavelength cylinders can be determined from the scattered fields discussed in the previous section under the Born Approximation and Multiple Scattering models. The aims of this section are to firstly show that the cylinders can be successfully reconstructed from the

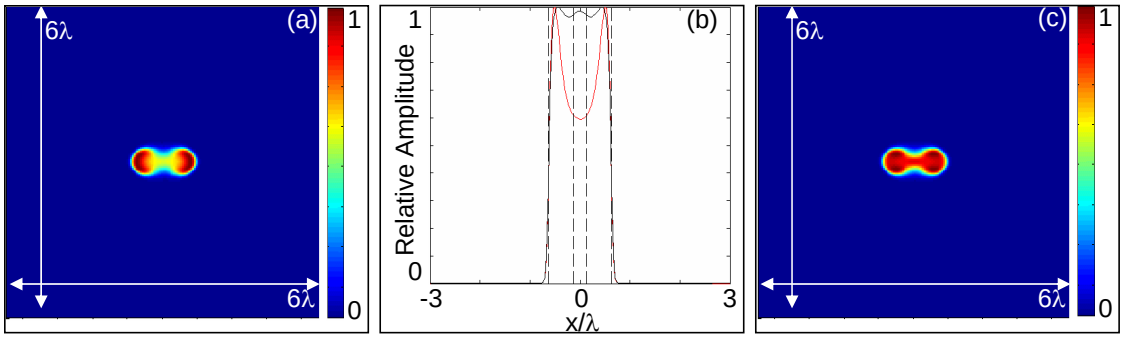

Figure 8.3: *Results produced by the Factorization method when applied to noiseless data obtained from the scattered field of two subwavelength cylinders, (a) Surface plot of the results obtained under the Multiple Scattering model, (b) Cross sections of the results for both physical models taken through the centre of both cylinders. The Multiple Scattering results are shown in red, the Born Approximation results are shown in black and the edges of the cylinders are shown by the dashed lines. (c) Surface plot of the results obtained under the Born Approximation model.*

scattered field and then to demonstrate that the inclusion of multiple scattering in the scattered field improves the robustness of the physical model. In a similar fashion to the case of point scatterers shown in Chapter 6, noise matrices will be: constructed, scaled to a level comparable to the computed scattered field for the two cylinders, and added to the multistatic response matrices for the respective physical models.

The Factorization method is used in this section in order to reconstruct the object as it provides an unbiased comparison of the images produced under both physical models. The results of applying the Factorization method to the scattered fields in the absence of noise are shown in Figure 8.3. The cross sections in Figure 8.3 (b) are taken through the centre of both cylinders and indicates that the cylinders have been resolved under both physical models, although the resolution is poorer under the Born Approximation. This result demonstrates that super resolution is possible in the case of extended objects. Due to numerical noise in the solution to the forward scattering problem, the results produced by the Factorization method under the Multiple Scattering model are better than those obtained under the Born Approximation model.

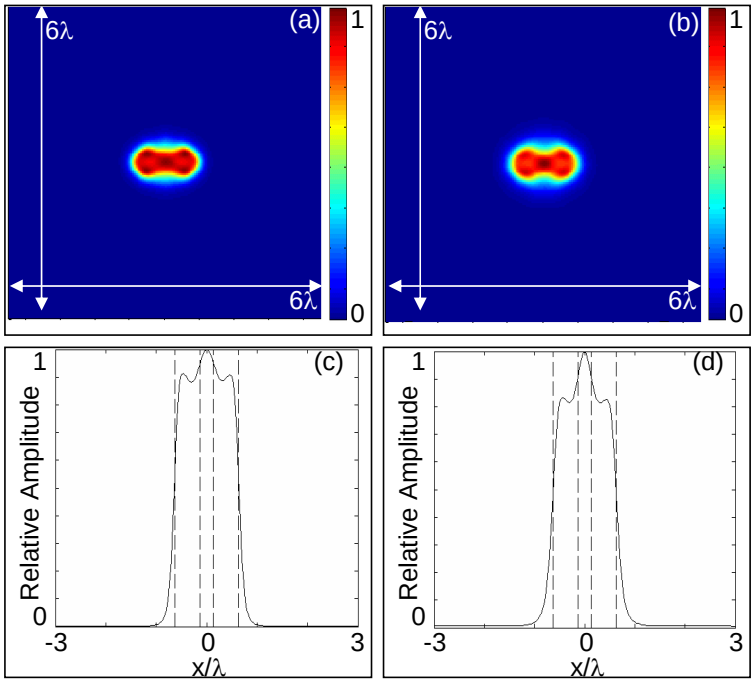

Figure 8.4: *Average Factorization method results for the case of two subwavelength cylinders based upon the Born Approximation model for various noise levels: (a) Surface plot for* $c_N = 0.01$*, (b) Surface plot for* $c_N = 0.1$*, (c) Cross section for* $c_N = 0.01$*, (d) Cross section for* $c_N = 0.1$*.*

In order to test the robustness of the physical models the effects of introducing additive random noise to the respective multistatic response matrices was investigated. The Born Approximated model was considered first. Fifty noise realizations were created and scaled to levels of $c_N = 0.01$ and $c_N = 0.1$; each realization was added to the semi-analytical Born Approximation model for the two cylinders. The noisy data for each noise realization was processed using the Factorization method, and the 50 results for each noise level were then averaged and are shown in Figure 8.4. Comparing the noisy results shown in Figure 8.4 with the noiseless results in Figure 8.3 (b) and (c) it can be seen that with a noise level as low as $c_N = 0.01$ the maximum at the centre of the cross sections becomes dominant, implying that the two cylinders can no longer be considered to be resolved. The dominance of the central maximum increases with the noise level implying that the image is tending towards that of a single extended object centred between the two cylinders (in a similar fashion to the case of two point scatterers).

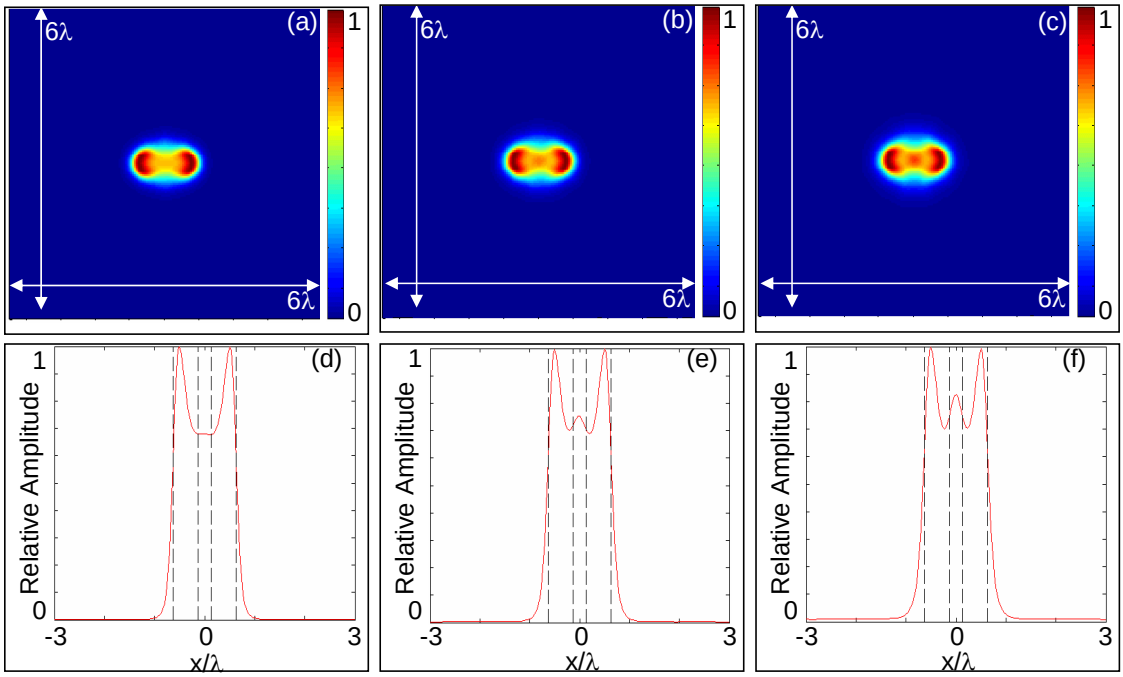

Figure 8.5: *Average Factorization results for the case of two subwavelength cylinders based upon the Multiple Scattering model for various noise levels: (a) Surface plot for* $c_N = 0.01$*, (b) Surface plot for* $c_N = 0.05$*, (c) Surface plot for* $c_N = 0.15$*, (d) Cross section for* $c_N = 0.01$*, (e) Cross section for* $c_N = 0.05$*, (f) Cross section for* $c_N = 0.15$*.*

The average results from processing the noisy data under the Multiple Scattering model with the Factorization method are shown in Figure 8.5. Unlike the results under the Born Approximation, the results when Multiple Scattering is considered appear to be able to cope with small perturbations to the ideal data. The cylinders in Figure 8.5 can be determined for noise levels from $c_N = 0.01$ to $c_N = 0.15$, however from the noise level of $c_N = 0.05$ a central maximum has started to develop. These results imply that multiple scattering encodes more information to the far field, thus the presence of two cylinders can be detected for higher noise levels than under the Born Approximation. This result complements that given in Chapter 6 for the case of point scatterers and the experimental results reported in [68].

8.4 Comparison with Finite Element Data

Having determined in the previous section that super resolution is achievable in the case of extended objects, this section will determine if this result can be reproduced using finite element simulations. If the model of two subwavelength cylinders can be successfully reproduced, this will imply the simulated scattered fields for objects of similar sizes can also be investigated using finite element analysis.

The geometry of the finite element model was based upon that given by Figure 8.1, a 5 cycle Hanning toneburst with a central frequency of $100kHz$ was used to illuminate the system, and the material properties of the background medium were defined to give a background velocity of $c_0 = 1500m/s$. The geometry was discretised using triangular elements with $E_\lambda \approx 30$ in order to provide an accurate description of the required geometry. The array was represented by 36 node points equally spaced the circumference of a circle with $R = 15\lambda$. The two cylinders were modeled with Dirichlet boundary conditions and as both having a radius of $r = \lambda/4$ with their centres' separated by $d = 3\lambda/4$. A blank model was also created where the cylinders were absent from the model; the signals recorded in this case were subtracted from those recorded when the cylinders were present in order to obtain only the signals caused by the scattering of the incident field by the two cylinders.

Having determined the scattered signals for every send and receive combination of the nodes that make up the array, the corresponding multistatic response matrix was constructed. The amplitude and phase of this matrix are shown in Figure 8.6 for an illumination angle of $\theta = \pi$. The corresponding results for the semi-analytical Multiple Scattering model are also shown. Since the effects of multiple scattering will be present in the finite element model the results shown in Figure 8.6 should be identical to those given by the semi-analytical Multiple Scattering model. The amplitude of the scattered field given by the finite element model is a good approximation of the results produced by the semi-analytical model, however, the phases given by the two models are completely different. The discrepancy in the phase of the finite element model implies that the scattered field in this case is not simulated

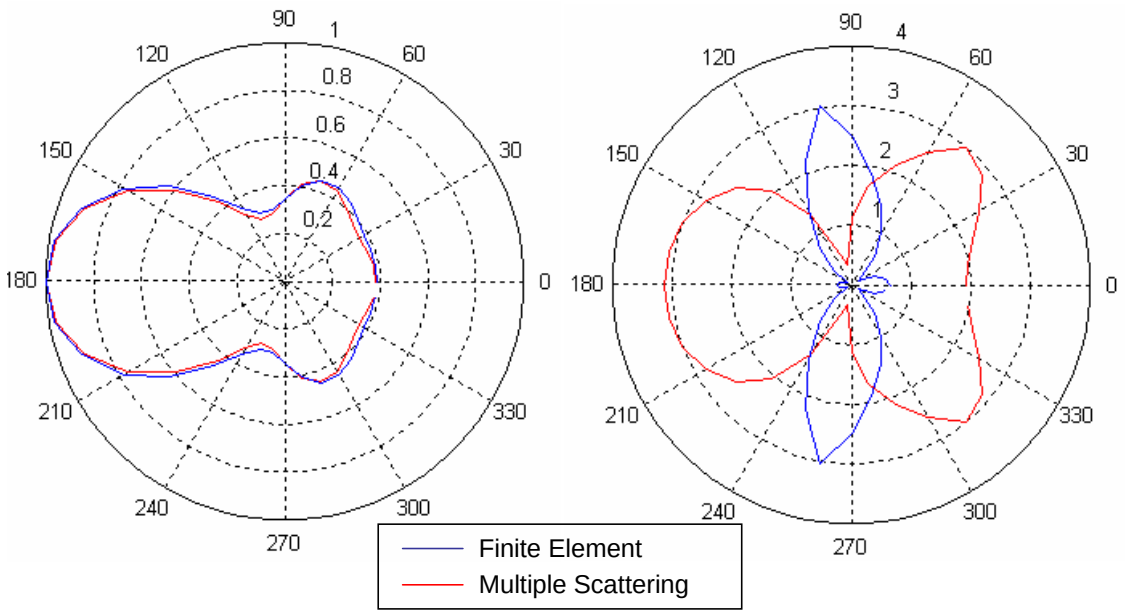

Figure 8.6: *Scattering amplitude of two cylinders for every detection angle ϕ due to an illumination angle $\theta = \pi$, shown for both the finite element simulation and the multiple scattering model, (a) the modulus of the scattering amplitude, (b) the phase of the scattering amplitude.*

correctly. Further differences in the multistatic response matrices are highlighted by examining their respective eigenvalues as shown in Figure 8.7. It can be seen that although the first 15 eigenvalues of both models follow the same trend, the remaining eigenvalues of the finite element model diverge from those given by the semi-analytic model. This effect on the eigenvalues is similar to that observed in the previous chapter when noise was introduced to the data obtained from the simulated models.

The results of applying the Factorization method to the scattered field produced by the finite element model are shown in Figure 8.8; the results for the semi-analytical Multiple Scattering model are also shown as a reference. It can clearly be seen that the results obtained from the finite element analysis completely fail to resolve the two cylinders. The presence of an object at the location of the two cylinders can be implied from the results, however the subwavelength structure of the object has been completely lost. This result leads to the conclusion that the scattered field in this case is not being correctly modeled by the finite element analysis of the

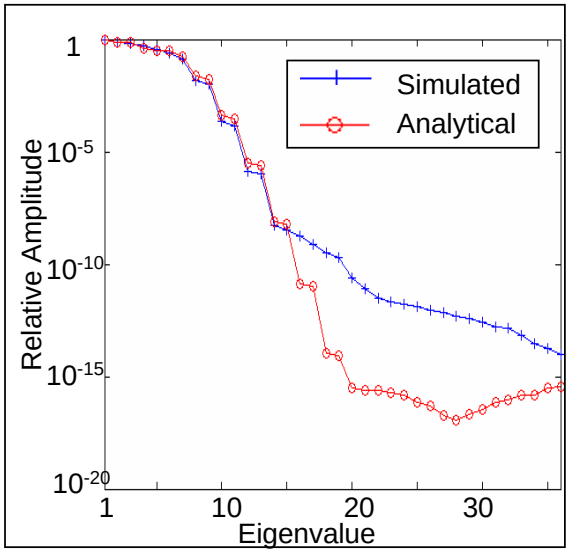

Figure 8.7: *Eigenvalues of the multistatic response matrices for the case of two subwavelength cylinders separated by a subwavelength distance. The semi-analytical results are shown in red and the finite element results are shown in blue.*

problem. One possible explanation for this error is that the multiple scattering of the evanescent waves is not being modeled correctly, this possibility will be investigated in the next subsection.

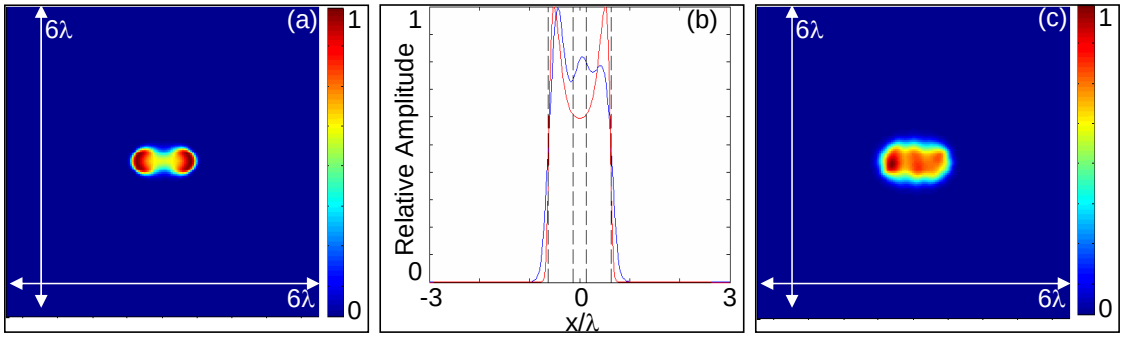

Figure 8.8: *Results produced by the Factorization method when applied to noiseless data obtained from the scattered field of two subwavelength cylinders, (a) Surface plot of the results obtained under the Multiple Scattering model. (b) Cross sections of the results for the Multiple Scattering model (shown in red) and the results produced using finite element analysis (shown in blue); the edges of the cylinders are shown by the dashed black lines. (c) Surface plot of the image obtained from the finite element analysis.*

8.5 Frustrated Total Internal Reflection

In Chapter 7 the validity of the finite element model to simulate propagating wavefields and the propagating scattered wavefields was demonstrated. However, it was shown in the previous section that the finite element model failed to correctly model the scattered field for two subwavelength separated objects. As it has been shown that the propagating waves are being modeled correctly, it is argued in this section that the scattering of evanescent waves are not being correctly modeled.

In most cases it is not possible to separate the scattered fields generated by the scattering of the propagating waves and those generated by the scattering of the evanescent waves. However, in the case of Frustrated Total Internal Reflection (FTIR) it is possible to study the scattering of the propagating and evanescent waves independently. An application of this phenomenon is multi-touch sensitive screens such as those used by Apple on the iphone and itouch hardware [89]. In order to explain FTIR, it is necessary to first consider the case of Total Internal Reflection (TIR).

With reference to Figure 8.9 (a), if a propagating wave traveling through Medium 1 with a velocity of c_1 encounters a boundary beyond which is Medium 2 which has a velocity of $c_2 > c_1$, then part of the energy that is present in the wave will be reflected back into Medium 1 and the rest will be transmitted into Medium 2. The reflection and transmission coefficients, which describe how much energy is reflected and transmitted with respect to the incident wave are dependent upon the material properties of the two media and the angle of incidence, φ_1, with respect to the normal of the boundary. The angles of incidence and refraction, φ_1 and φ_2 respectively, as shown in Figure 8.9 (a) are governed by Snell's law, which states that $sin(\varphi_1)/sin(\varphi_2) = c_1/c_2$. If $\varphi_1 > \varphi_c = \sin^{-1}(c_1/c_2)$, where φ_c is termed the 'critical angle', then φ_2 becomes complex and no energy is transmitted into the second medium. In this case the amplitude of the reflection coefficient is 1 with respect to the incident wave and the transmission coefficient is 0, this is known as TIR. Although no energy is transmitted, evanescent waves are produced in the

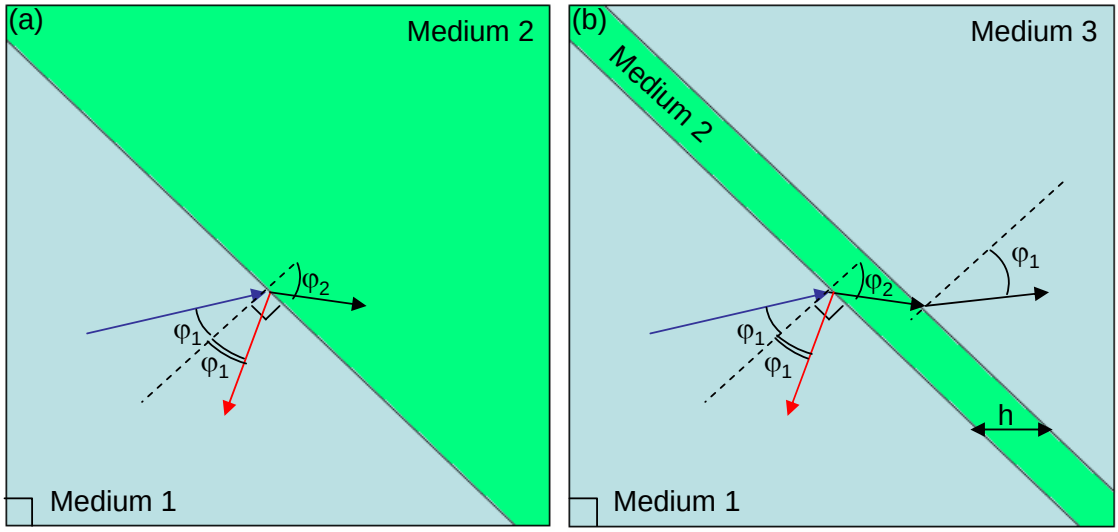

Figure 8.9: *(a) Schematic of a setup resulting in Total Internal Reflection. The path of the incident wave is shown in blue and the path of the reflected signal is shown in red, (b) Schematic of a setup resulting in Frustrated Total Internal Reflection, as previously the path of the incident and reflected waves are shown in blue and red, the path of the transmitted waves are shown in black.*

second medium.

FTIR occurs when a third medium (Medium 3) is introduced. It will be assumed that Medium 3 has the same velocity and material properties as Medium 1. In this case Medium 2 is sandwiched between Medium 1 and Medium 3. If $\varphi_1 > \varphi_c$ the evanescent waves produced at the boundary between Medium 1 and Medium 2 will be scattered by the boundary between Medium 2 and Medium 3, producing a second evanescent wave in Medium 2 and a propagating waves in Medium 3. Although each evanescent wave in Medium 2 does not radiate energy in the direction perpendicular to the layer, the superposition of two evanescent waves causes energy radiation.

The reflection and transmission coefficients in the case of FTIR as shown in Figure 8.9 (b) (see for example [90] and [91]) are given as:

$$R^c_{(FTIR)} = \frac{R^c_{12} + R^c_{12} e^{i\beta}}{1 + R^c_{12} R^c_{23} e^{i\beta}}, \tag{8.8}$$

and the transmission coefficient is given by:

$$T^c_{(FTIR)} = \frac{T^c_{12} + T^c_{12} e^{i\beta}}{1 + R^c_{12} R^c_{23} e^{i\beta}}, \tag{8.9}$$

where the constant $\beta = -(2\pi/\lambda)2h\cos(\varphi_1)/c_1$, and h is the thickness of the second medium. The reflection and transmission coefficients between Medium 1 and Medium 2 are given by R^c_{12} and T^c_{12} and are defined as:

$$R^c_{12} = \frac{(\cos(\varphi_1)/c_1) - (\cos(\varphi_2)/c_2)}{(\cos(\varphi_1)/c_1) + (\cos(\varphi_2)/c_2)}, \tag{8.10}$$

and

$$T^c_{12} = \frac{2(\cos(\varphi_1)/c_1)}{(\cos(\varphi_1)/c_1) + (\cos(\varphi_2)/c_2)}, \tag{8.11}$$

the transmission and reflection coefficients between Medium 2 and Medium 3 (R^c_{23} and T^c_{23} respectively) are calculated in a similar fashion. Equations 8.8 and 8.9 can be used to predict the reflection and transmission coefficients for a range of frequencies in the case of FTIR, and will be used to determine whether or not the reflection and transmission coefficients in the finite element model are being simulated correctly.

In order to generate FTIR using finite element analysis, a model with a square geometry, consisting of three parts, as shown in Figure 8.10 (a) was created. An incident wave was generated along one side of Part 1 as shown in Figure 8.10 (a), giving an angle of incidence of $\varphi_1 = \pi/4$ with respect to the normal of the boundary in this case. This model was considered for three cases; the first case corresponded to TIR, the second was concerned with FTIR and the final case was a blank model which was used to remove the incident signals from the scattered signals. In each model a plane like wave with a central frequency of 100kHz was introduced into

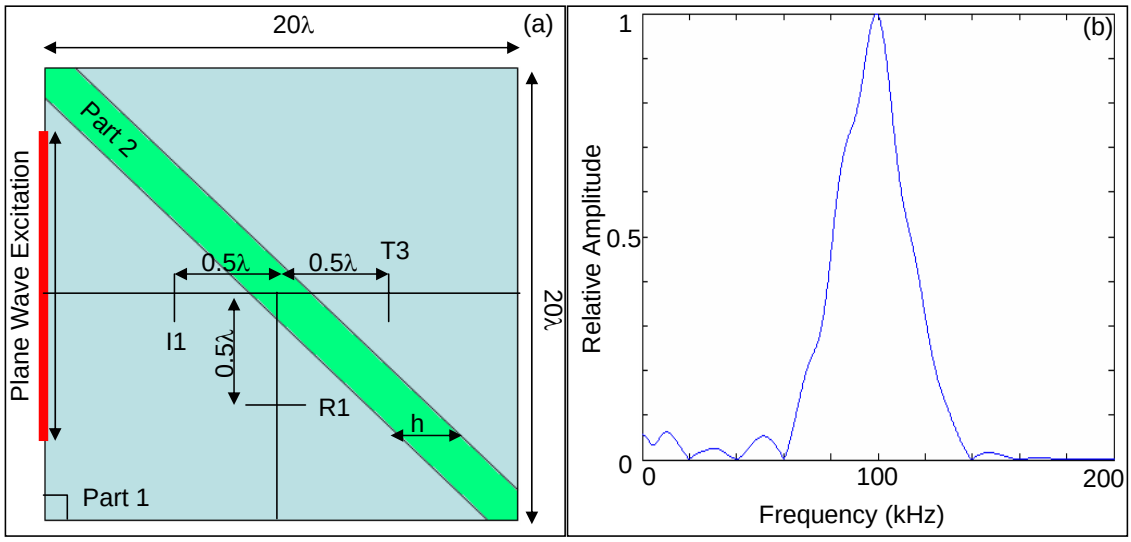

Figure 8.10: *Finite element model used to simulate Frustrated Total Internal Reflection (a) Schematic of the model dimensions, (b) Amplitude of the frequency response of the incident plane wave used in the simulation.*

the background medium of Part 1. The frequency spectrum of this signal is shown in Figure 8.10 (b). The main lobe of the frequency spectrum lies between 60 and 140kHz, as such the reflection and transmission coefficients will be calculated in this frequency range. The monitoring points $I1$, $R1$ and $T3$ were created in Parts 1 and 3, as shown in Figure 8.10 (a), in order to monitor the: incident, reflected and transmitted signals respectively. In order to calculate the reflection and transmission coefficients the frequency response of the signals recorded at the points $R1$ and $T3$ were compared with the frequency response of the incident signal recorded at $I1$.

In the first case, Part 1 has the material properties of water with $c_1 = 1500m/s$ and Parts 2 and 3 possess the same density as the first part but the background velocity for both parts is $c_2 = c_3 = 3000m/s$, giving a critical angle of $\varphi_c = \pi/6$. Since $\varphi_1 > \varphi_c$, TIR should be observed in this case and a reflection coefficient of 1 should be generated by the simulated data. The reflection coefficient from the simulated data is shown in Figure 8.11 (a). Although not exactly 1 it is a good approximation, especially around the central frequency of $100kHz$.

In the case of FTIR the first and third parts have the material properties of water and a background velocity of $c_1 = c_3 = 1500m/s$ whereas the second part has a

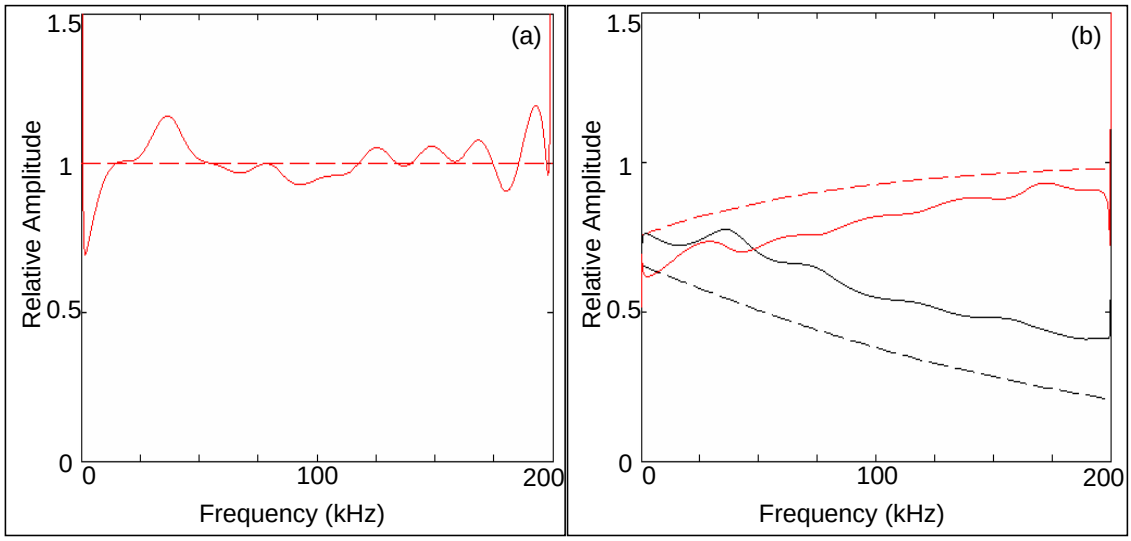

Figure 8.11: *Reflection and Transmission coefficients recorded from the finite element simulations (a) Reflection coefficient for the case of Total Internal Reflection (b) Reflection coefficient (shown in red) for the case of Frustrated Total Internal Reflection. The theoretical values are shown by the dashed line, the corresponding Transmission coefficients are shown in black.*

velocity of $c_2 = 3000m/s$. Once again the incidence angle $\varphi_1 = \pi/4 > \varphi_c$ and so FTIR should take place. The reflection and transmission coefficients recorded from the finite element model in this case are shown in Figure 8.11 (b); the theoretical values being shown by the dashed lines. It can be observed that although the reflection and transmission coefficients follow the trend of the theoretical values, the simulated reflection coefficients are consistently lower than the theoretical values and the simulated transmission coefficients are consistently higher than the theoretical values. The results shown in Figure 8.11 strongly imply that the reflection and transmission coefficients are not being correctly simulated by the finite element model, meaning the scattering of evanescent fields are not correctly simulated by the finite element model.

8.6 Summary

This chapter has outlined the semi-analytical model that describes the scattered field for the case of a circular array illuminating two cylinders at its centre. It was shown that there was a marked difference between the scattered field produced under the Born Approximation and when the effects of multiple scattering were considered. When the Factorization method was applied to the scattered fields it was shown that super resolution could be achieved under both physical models. This result demonstrates that super resolution is theoretically possible in the case of extended objects without the use of prior knowledge. When random noise was introduced to the scattered fields it was shown that under the Born Approximation the cylinders could not be resolved even when relatively low levels of noise are introduced to the scattered fields. It was shown that the inclusion of multiple scattering leads to a model which is more robust to the effects of noise, as the cylinders were resolvable for higher levels of noise than under the Born Approximation.

Finite element analysis was then used in order to model the case of two subwavelength cylinders, however, it was shown that the finite element model produced errors in the scattered field. The errors in the simulated scattered field led to a breakdown of the Factorization method which was unable to resolve the cylinders in this case. It has been argued that the finite element model is not able to simulate the scattering of the evanescent fields correctly which subsequently leads to the errors in the simulated scattered field. The case of Frustrated Total Internal Reflection was simulated using finite element analysis to demonstrate that the resulting simulated reflection and transmission coefficients were not consistent with the theoretical values, implying that scattering of evanescent waves is incorrectly modeled by finite element analysis. The subsequent errors in the scattered field acts as a form of noise, causing a breakdown of imaging methods applied to the data.

Chapter 9

Discussion and Conclusions

9.1 Thesis Summary

This thesis has investigated the possibility of achieving super resolution from the scattered field of an object measured in the far field. As discussed in Chapter 1, the well established technique of Near-field Scanning Optical Microscopy exploits the scattering of evanescent fields detected within one wavelength of an object in order to achieve super resolution. However, in many applications access to the near field of an object is not feasible and so being able to achieve super resolution in the far field is an attractive prospect. In order to achieve super resolution in the far field this thesis has argued that the effects of multiple scattering between objects needs to be considered.

The forward scattering problem, which is concerned with the prediction of the scattered field for a prescribed object and incident field was outlined in Chapter 2. It was demonstrated through the Lippmann Schwinger equation that the spatial harmonics of the object shorter than $\lambda/2$ do not affect the scattered field under the Born Approximation. In contrast, this is not true when multiple scattering is included in the forward scattering model.

The inverse scattering problem of deriving the object from the measured scattered

field was outlined in Chapter 3. It was demonstrated that this problem is non-linear and ill-posed in the sense of Hadamard. It was shown that the Born Approximation offers a linear solution to the inverse problem, however, the lack of higher spatial frequencies described by the scattered field under the Born Approximation (as discussed in Chapter 2) limits the resolution achievable. The approach of linear sampling techniques, which attempt to solve the inverse problem by reconstructing the boundary of an object from the scattered field rather than the object itself, was also outlined in this chapter. Linear sampling methods allow the effects of multiple scattering present in the scattered field to be taken into account in the reconstruction of the object. The Factorization method which is theoretically capable of achieving unlimited resolution and is itself a linear sampling method was also discussed.

In Chapter 4, the practical aspects of illuminating an object and measuring the resulting scattered field with an array of transducers were discussed. This involved an examination of the temporal and spatial sampling criterion and an outline of the methods of subtraction and gating to remove the incident field from the measured scattered field. It was also shown in this chapter, how the Factorization method derived in Chapter 3, could be adapted to be used when the scattered field is measured at a discrete number of points that make up an array.

The Bartlett, Time Reversal and MUSIC and Maximum Likelihood imaging methods were introduced in Chapter 5; each of these methods were originally derived under a passive array system to detect point sources. However, a link between the active and passive array systems was discussed thus allowing these methods to be adapted to be used with an active array system. This chapter also outlined how random noise which is always present in experimental measurements could be modeled in order to test the robustness of the imaging techniques.

The case of two subwavelength separated point scatterers was considered in Chapter 6, the scattered field under both the Born Approximation and Multiple Scattering models was examined. It was demonstrated that more information relating to the subwavelength structure of the object was encoded to the far field when the effects of multiple scattering were considered. The effects of introducing noise into the scat-

tered fields for both physical models was investigated by applying the Factorization method to noise corrupted data. It was shown that the scattered field produced under the Born Approximation was less robust than that produced when the effects of multiple scattering were considered. It was also shown, by application of the Maximum Likelihood method, that assuming the incorrect forward scattering model when reconstructing the object from the scattered field can lead to significant errors in the solution. The imaging algorithms were applied to the experimental data obtained from the illumination of a steel block with two holes which were regarded as being point-like. It was shown that unlike the Bartlett and state-of-the-art phased array methods, the Time Reversal and MUSIC and Factorization methods were able to resolve the scatterers in this case, demonstrating that super resolution is achievable experimentally.

Chapter 7 demonstrated that the Bartlett, Factorization and Time Reversal and MUSIC imaging methods that were used in the previous chapter in order to reconstruct point scatterers from the scattered field, could also be used to reconstruct extended objects which were larger than the interrogating wavelength. In order to generate the data in this case, the idea of finite element analysis was introduced. The validity of this method to simulate the propagation of acoustic waves and the scattered field caused by a sound soft cylinder were investigated. The finite element data obtained from the illumination of a sound soft cylinder and a sound soft square were then applied to each of the algorithms, each of which provided successful reconstructions of the objects. Random noise was then introduced to the finite element data, the effect that noise has on the eigenvalues of the multistatic response matrix was presented. It was shown that the objects could be reconstructed even when high levels of noise were added to the finite element data.

Having demonstrated that the sampling techniques could be successfully applied to the data obtained from extended objects in the previous chapter, Chapter 8 investigated whether super resolution could still be achieved in the case of extended objects. In a similar fashion to Chapter 6, it was shown that super resolution for two subwavelength cylinders separated by a subwavelength distance could be achieved

when considering the scattered field produced under the Born Approximation and when the effects of multiple scattering were considered. It was also demonstrated that the forward scattering model under the Born Approximation was highly sensitive to noise whereas the Multiple Scattering model was more robust and able to resolve the cylinders for higher levels of additive noise.

The scattered field produced by the two cylinders under the Multiple Scattering model was compared to the field obtained under finite element analysis. It was shown that there were significant differences between the two models and that the reconstruction based on the finite element data could not resolve the cylinders in this case. It was argued that the difference in the models was due to the scattering of the evanescent fields being incorrectly modeled in the finite element analysis. This argument was backed up by considering the reflection and transmission coefficients produced by the finite element analysis of Frustrated Total Internal Reflection which were inconsistent with the theoretical values.

9.2 Main Results

The first five chapters of this thesis have introduced the theoretical framework behind super-resolution imaging. This thesis has brought together arguments from several fields of study and adapted them in order to describe the phenomenon of super resolution. This work not only describes the theory behind super resolution but also describes how measurements should be performed in practise as well as outlining imaging methods that can be applied to the measured data.

The simple case of two subwavelength separated point scatterers discussed in Chapter 6, demonstrated the importance of including the effects of multiple scattering in both the forward and inverse scattering problems. In the case of the forward scattering problem it was demonstrated that under the Born Approximation, the far-field measurements were similar to those produced by a single scatterer. Although the point scatterers could be resolved under the Born Approximation in the absence of noise, it was observed that the targets could no longer be resolved when a noise

level of $c_N \approx 0.1$ was introduced to the system. On the other hand, the inclusion of multiple scattering in the forward model produced a more complicated scattered field than that obtained under the Born Approximation. It was observed that this model was more robust to noise and that the point scatterers could be resolved for noise levels approximately ten times that achieved by the Born Approximation. The result demonstrates that multiple scattering is a key aspect of super resolution imaging.

It was also shown in Chapter 6 that assuming the incorrect forward scattering model could be detrimental to the reconstruction of the object from the scattered field. It was observed that processing the scattered field produced by a model which included the effects of multiple scattering, with an imaging method which assumed the Born Approximation would produce errors in the reconstruction. The effects of multiple scattering are treated as a form of coherent noise when its presence is not accounted for by the imaging method and thus has a detrimental effect on the images produced. This result implies that imaging methods which assume the Born Approximation will be unable to achieve super resolution in practise as the effects of multiple scattering will be present in any scattered field measured experimentally. Thus in order to achieve super resolution experimentally, the effects of multiple scattering must be taken into account. These results have been published in $[P1, P2]$.

The results presented in Chapters 7 and 8, not only demonstrate that the imaging methods that were derived in previous chapters under the assumption of point scatterers are also applicable to the scattered field obtained from extended objects, but also that super resolution is achievable in the case of extended objects. In a similar fashion to the work done on the case of two point scatterers, it was shown that including the effects of multiple scattering in the forward scattering model resulted in a scattered field that was robust to the effects of noise. Under the Born Approximation it was shown that scattered field was highly sensitive to the effects of noise. These results concur with those given for the case of point scatterers in Chapter 6 and imply that in order for super resolution of extended objects to be achieved in practice, the effect of multiple scattering must be accounted for.

The scattered fields that were processed by the imaging methods in Chapter 7 were the results of simulations carried out using finite element analysis. It appears for the case of the sound soft cylinder and square, that finite element analysis is a valid method for simulating the scattered fields. However, in Chapter 8 it was shown that the finite element analysis of two subwavelength cylinders produced errors in the simulated scattered field; thus it was demonstrated that the scattering of evanescent waves is not being correctly modeled by finite element analysis. It can be concluded from this study that finite element analysis is a powerful technique that can be used to successfully model the scattered field resulting from the illumination of an object with features larger than the interrogating wavelength.

9.3 Future work

This thesis has demonstrated that Linear Sampling methods that achieve super resolution can successfully be applied to reconstruct extended objects from their scattered field. The scattered field in this case was obtained by enclosing the object in a circular array, however as mentioned in Chapter 1, there are situations when only a limited view is feasible and so the object cannot be enclosed. As such it would be useful to conduct an investigation into the validity of the results produced by the imaging methods, when processing the scattered field of an extended object from a linear or partial view array.

The finite element model that was used in Chapter 8 does not appear to model the scattering of evanescent fields correctly, further investigations could be conducted to determine if this is solely due to the finite element method or if further refinements to the model could improve the modeling of evanescent waves. Due to the super oscillatory nature of the evanescent waves, the finite element mesh may need further refinements in order to model the scattered field correctly. It should be noted however, that the number of elements per wavelength used in this model was the maximum achievable using a computer with 16 Gigabytes of RAM. Further refinements of the mesh would require a significant increase in computing capabilities.

If however, as implied by the results in Chapter 8, finite element analysis does not model the scattering of evanescent fields correctly it would still be beneficial to be able to utilise numerical methods to simulate the scattered field generated by the illumination of subwavelength characteristics, this would allow the scattered field for a variety of objects with complicated geometries to be examined in the absence of noise. An alternative approach to simulating the scattered field, would be to use boundary element methods, which only require the discretisation of the boundary of the object rather than discretisation of the object and the background medium. Another possible approach would be to use Embedded formulae [92] which allows the scattered field which is dependent upon the various angles of illumination and detection to be decomposed into fewer angular variables, resulting in a problem which is less computationally expensive.

All of the sampling methods presented in this thesis rely upon the interpretation of the scattered field at a single frequency. Information on the structure of the object is encoded into the different frequencies that make up the scattered field. It is possible that exploiting the information included in the different frequencies of the scattered field could be extremely beneficial to object reconstruction. If feasible, this approach could be used to compensate for the lack of information obtained from limited view arrays, allowing images that are better resolved than those obtained from a single frequency to be obtained.

Super resolution has been demonstrated in this thesis for Linear Sampling methods which reconstruct the boundary of an object based upon the measured scattered field. In many applications the shape, size and location of the object given by the boundary is all that is required. However, in other cases information on the material properties of the object is desirable, as such the linear sampling methods described in this thesis will be unable to provide such information. As such, imaging methods which can achieve super resolution in the far field and provide information on the material properties of the object would further improve upon the results presented in this thesis. An iterative approach to solving the inverse problem which incorporates the effects of multiple scattering could be a way of achieving this.

Appendix A

The scattering coefficient

This appendix derives the expression for the scattering coefficient for an elastic point scatterer which is consistent with energy conservation, as used in Chapter 6. In two dimensions the optical theorem is given by:

$$\sigma_T = \sqrt{\frac{8\pi}{k_0}} Im[e^{-i\pi/4} f(\hat{\mathbf{r}}_\mathbf{0}, \hat{\mathbf{r}}_\mathbf{0})], \tag{A.1}$$

where σ_T is the total cross section (scattering plus absorption cross sections) and $Im[.]$ refers to the imaginary part of the argument. For elastic scattering, the total cross section equals the scattering cross section; therefore the scattering cross section is equal to the extinction cross section [93]. Thus the scattering amplitude for a single point scatterer must satisfy the condition:

$$|f|^2 = \sqrt{\frac{2}{\pi k_0}} Im[e^{-i\pi/4} f], \tag{A.2}$$

as such for an elastic point scatterer:

$$f = -\frac{1}{\sqrt{4\pi k_0}}(1 - i - \sqrt{2}e^{ip}), \tag{A.3}$$

where $p \in [0, 2\pi]$. The scattering coefficient is related to the scattered field ψ_s and the Green's function G via:

$$\psi_s = -\tau G. \tag{A.4}$$

Using the asymptotic form of the Green's function together with Equation A.3, the scattering coefficient becomes:

$$\tau = 2(e^{ip} + i), \tag{A.5}$$

where the coefficient p is dependant upon the geometrical and material properties of the scatterer. In general p is a function of frequency so as to describes the dispersion of the scattering coefficient and accounts for its resonances.

Appendix B

The scattered field produced by a cylinder

This appendix will outline the analytical expression that describes the scattered field resulting from the illumination of a cylinder. This expression was used in Chapter 7 to determine the accuracy of the finite element analysis of the illumination of a cylidner. It will be assumed that the cylinder has a radius r, and that it is illuminated by a circular array with a radius R, with angles of illumination and detection of θ and ϕ respectively, as shown in Figure 7.3 in Chapter 7. It is also assumed that the cylinder is impenetrable and so the Dirichlet condition that the scattered field is zero on the boundary of the cylinder is used. In this case the scattered field, ψ_s, shown for example in [94] is given by:

$$\psi_s = -\frac{J_0(k_0 r)H_0(k_0 R)}{H_0(k_0 r)} - 2\sum_{n=1}^{\infty} \frac{i^n J_n(k_0 r)H_n(k_0 R)cos[n(\phi-\theta)]}{H_n(k_0 r)}, \tag{B.1}$$

where k_0 is the wavenumber of the interrogating wavefield, J_n are the n^{th} order Bessel functions of the first kind and H_n are the n^{th} order Hankel functions of the first kind which describe outward propagating waves. As the terms in the summation of Equation B.1 decay exponentially as $n \to \infty$ the summation is truncated so that the expression can be evaluated. Consider the cylinder and array setup used in Chapter

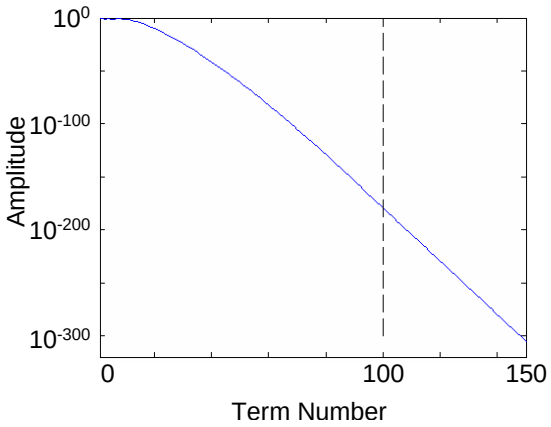

Figure B.1: *The amplitude of the first 150 terms of the infinite sum in Equation B.1 for* $r = 1.5\lambda$ *and* $R = 15\lambda$*, the truncation point is shown by the black dashed line.*

7, in this case $r = 1.5\lambda = 0.0225m$ and $R = 15\lambda = 0.225m$ (where $\lambda = 0.015m$), the amplitude of the first 150 terms of the summation in Equation B.1 are shown in Figure B.1 for the case when $\phi - \theta = \pi$ as this corresponds to the maximum amplitude of the scattered field as shown in Figure 7.4 in Chapter 7. It can be seen from Figure B.1 that the magnitude of the terms in the summation rapidly decay, this trend is followed for all combinations of θ and ϕ. The summation is truncated after the first 100 terms (indicated by the dashed line), the resulting expression was used in Chapter 7.

References

[1] G. G. van Dooren, M. Marti, C. J. Tonkin, L. M. Stimmler, A. F. Cowman, and G. J. McFadden. Development of the endoplasmic reticulum, mitochondrion and apicoplast during the asexual life cycle of plasmodium falciparum. *Molecular Microbiology*, 57(2):405–419, 2005.

[2] O. Gingerich. A brief history of our view of the universe. *Astron. Soc. of the Pacific*, 111:254–257, 1999.

[3] W. C. Röntgen. On a new kind of rays (1945 translation). *Würzburg's Physical-Medical Society journal*, 1895.

[4] W. P. Jensen, G. J. Palenik, and I. Suh. The history of molecular structure determination viewed through the nobel prizes. *J. Chem. Ed.*, 80(7):753–761, 2003.

[5] E. M. Purcell, H. Torrey, and R. V. Pound. *Resonance Absorption by Nuclear Magnetic Moments in a Solid*, volume 69. 1946.

[6] F. Bloch, W. W. Hansen, and M. Packard. The nuclear induction experiment. *Phys. Rev.*, 70(7 and 8):474–489, 1946.

[7] P. C. Lauterbur. Image formation by induced local interactions: examples employing nuclear magnetic resonance. *Nature*, 242:190–191, 1973.

[8] R. Damadian. Tumor detection by nuclear magnetic resonance. *Science*, 171(3976):1151–1153, 1971.

[9] P. A. Bottomley. NMR imaging techniques and applications: A review. *Rev. Sci. Instrum.*, 53(9):1319–1337, 1982.

[10] P. P. Ewald. *Fifty years of X-Ray Diffraction.* International Union of Crystallography, 1962.

[11] W. H. Bragg and W. L. Bragg. The reflection of x-rays by crystals. *Proc. Royal Soc. of London Series A*, 88(605):428–438, 1913.

[12] J. D. Watson and F. H. C. Crick. A structure for deoxyribose nucleic acid. *Nature*, 171:737–738, 1953.

[13] D. C. Hodgkin. The x-ray analysis of complicated molecules. *Science*, 150(3699):979–988, 1965.

[14] R. J. James. A history of radar. *IEE Review*, 35(9):343–349, 1989.

[15] L. D. Ehrman and A. D. Lanterman. Automated target recognition using passive radar and coordinated flight models. *Proc. SPIE*, 5094:196–207, 2003.

[16] G. Reber. A play entitled the beginning of radio astronomy. *J. Roy. Astron. Soc. Can.*, 82(3):93–106, 1988.

[17] A. Van der Veen, A. Leshem, and A. Boonstra. Array signal processing for radio astronomy. *Experimental Astronomy*, 17:231–249, 2004.

[18] D. Kane, W. Grassi, R. Sturrock, and P. V. Balint. A brief history of musculoskelatal ultrasound: 'from bats and ships to babies and hips'. *Rheumatology*, 43(7):931–933, 2004.

[19] P. N. T. Wells. The medical applications of ultrasonics. *Rep. Prog. Phys.*, 33:45–99, 1970.

[20] P. N. T. Wells. Ultrasonic imaging of the human body. *Rep. Prog. Phys.*, 62:671–722, 1999.

[21] D. J. Daniels, D. J. Gunton, and H. F. Scott. Introduction to subsurface radar. *IEE Proc*, 135 Part F(4):278–320, 1988.

[22] D. M. McCann, P. D. Jackson, and P. J. Fenning. Comparison of the seismic and ground probing radar methods in geological surveying. *IEE Proc*, 135 Part F(4):380–390, 1988.

[23] L. P. Jr. Peters, J. J. Daniels, and J. D. Young. Ground penetrating radar as a subsurface environmental sensing tool. *Proc IEEE*, 82(12):1802–1822, 1994.

[24] E. Abbe. Beiträge zur theorie des mikroskops und der mikroskipischen wahrnehmung (contributions to the theory of the microscope and the microscopic perception). *Arch. Mikrosk Anat*, 9:413–468, 1873.

[25] Lord Rayleigh. On the manufacture and theory of diffration gratings. *Phols. Mag.*, 47:81–93, 193–205, 1874.

[26] Lord Rayleigh. Investigations in optics with special reference to the spectroscope. *Phols. Mag.*, 8:261–274, 403–411, 477–486, 1879.

[27] Lord Rayleigh. Investigations in optics, with special reference to the spectroscope. *Phols. Mag.*, 9:continued from vol 8 p486, 40–55, 1880.

[28] E. H. Synge. Suggested method for extending microscopic resolution into the ultra-microscopic region. *Philos. Mag.*, 6:356–362, 1928.

[29] E. A. Ash and G. Nicholls. Super-resolution aperture scanning microscope. *Nature*, 237:510–512, 1972.

[30] E. Betzig, J. K. Trautman, T. D. Harris, J. S. Weiner, and R. L. Kostelak. Breaking the diffraction barrier: Optical microscopy of a nanometric scale. *Science*, 251:1468–1470, 1991.

[31] D. Courjon. *Near-field microscopy and near-field optics*. Imperial College Press, London, 2003.

[32] A. Lewis, H. Taha, Strinkovski, A. Manevitch, A. Khatchatouriants, R. Dekhter, and E. Ammann. Near-field optics: from subwavelength illumination to nanometric shadowing. *Nature Biotech.*, 21:1378–1386, 2003.

[33] J.-J. Greffet and R. Carminati. Image formation in near-field optics. *Prog. Surf. Sci.*, 56(3):133–237, 1997.

[34] J. B. Pendry. Negative refraction makes a perfect lens. *Phys. Rev. Lett.*, 18:3966–3969, 2000.

[35] J. B. Pendry, D. Schurig, and D. R. Smith. Controlling electromagnectic fields. *Science*, 312(5781):1780–1782, 2006.

[36] D. R. Smith, J. B. Pendry, and M. C. K. Wiltshire. Metamaterials and negative refractive index. *Science*, 305:788–792, 2004.

[37] P. M. Morse and H. Feshbach. *Methods of theoretical physics*. McGraw-Hill Book Company, New York, London, 1953.

[38] J. D. Jackson. *Classical electrodynamics*. John Wiley & Sons, Inc., third edition, 1999.

[39] D. Colton and R. Kress. *Inverse acoustic and electromagnetic scattering theory*, volume 93. Springer-Verlag, Berlin, 1992.

[40] B. Chen and J. J. Stamnes. Validity of diffraction tomography based on the first Born and the first Rytov approximations. *Appl. Opt.*, 37(14):2996–3006, 1998.

[41] M. Slaney, A. C. Kak, and L. E. Larsen. Limitations of imaging with first-order diffraction tomography. *IEEE Trans. Microwave Theory Tech.*, MIT-32(8):860–874, 1984.

[42] L. S. Rodberg and R. M. Thaler. *The quantum theory of scattering*. Academic Press, New York, 1967.

[43] F. Simonetti. Multiple scattering: The key to unravel the subwavelength world from the far-field pattern of a scattered wave. *Phys. Rev. E*, 73:036619–1, 2006.

[44] A. O. Barut. *The theory of the scattering matrix : for the interactions of fundamental particles*. Macmillan, New York, 1967.

[45] M. Reed and B. Simon. *Methods of Modern Mathematical Physics.* Academic Press, New York, 1979.

[46] D. Colton and R. Kress. Eigenvalues of the far field operator for the helmholtz equation in an absorbing medium. *SIAM J. Appl. Math.*, 55(6):1724–1735, 1995.

[47] C. Prada, J. L. Thomas, and M. Fink. Decomposition of the time reversal operator: detection and selective focusing on two scatterers. *J. Acoust. Soc. Am.*, 99(4):2067–2076, 1996.

[48] F. Rellich. Über das asymptotische verhalten der lösungen von $\delta u + \lambda u = 0$ in unendlichen gebieten. *Jber. Deutsch. Math. Verein.*, 53(3):57–65, 1943.

[49] P. D. Lax and R. S. Phillips. *Scattering theory.* Academic Press, New York, 1967.

[50] A. Kirsch and R. Kress. Uniqueness in inverse obstacle scattering. *Inverse Probl.*, 9:285–299, 1993.

[51] D. Colton. Inverse acoustic and electromagnetic scattering theory. *Inverse Probl.*, 47:67–110, 2003.

[52] R. Potthast. *Point Sources and Multipoles in Inverse Scattering Theory.* Chapman & Hall / CRC, London, 2001.

[53] R. Potthast. On a concept of uniqueness in inverse scattering for a finite number of incident waves. *SIAM J. Appl. Math.*, 58(2):666–682, 1998.

[54] R. D. Luke and R. Potthast. The no response test - a sampling method for inverse scattering problems. *SIAM J. Appl. Math.*, 63(4):1292–1312, 2003.

[55] F. C. Chen and W. C. Chew. Experimental verifiction of super resolution in nonlinear inverse scattering. *Appl. Phys. Lett.*, 72(23):3080–3082, 1998.

[56] D. Colton and A. Kirsch. A simple method for solving inverse scattering problems in the resonance region. *Inverse Probl.*, 12:383–393, 1996.

[57] A. Kirsch. Characterization of the shape of a scattering obstacle using the spectral data of the far field operator. *Inverse Probl.*, 14:1489–1512, 1998.

[58] M. Bertero and P. Boccacci. Super-resolution in computational imaging. *Micron*, 34:265–273, 2003.

[59] T. Habashy and E. Wolf. Reconstruction of scattering potentials from incomplete data. *J. Mod. Opt.*, 41:1679–1685, 1994.

[60] C. K. Rushforth and R. W. Harris. Restoration, resolution and noise. *J. Opt. Soc. Am.*, 58:539–545, 1968.

[61] D. Slepian and H. O. Pollak. Prolate spheroidal wave functions, fourier analysis and uncertainty I. *Bell Syst. Tech. J.*, 40:43–63, 1961.

[62] G. Toraldo Di Francia. Degrees of freedom of an image. *J. Opt. Soc. Am.*, 59:799–804, 1969.

[63] C. E. Shannon. Communications in the presence of noise. *Proc. IRE*, 37(1):10–21, 1949.

[64] F. Simonetti, L. Huang, and N. Duric. On the sampling of the far-field operator with a circular ring array. *J. Appl. Phys.*, 101:083103, 2007.

[65] M. P. Andre, Martin P.J. Janee, H. S., G. P. Otto, B. A. Spivey, and Palmer D. A. High-speed data acquisition in a diffraction tomography system employing large-scale toroidal arrays. *Int. J. Imag. Syst. Tech.*, 8:137–147, 1997.

[66] N. Duric, L. Littrup, P. Poulo, A. Babkin, R. Pevzner, E. Holsapple, O. Rama, and C. Glide. Detection of breast cancer with ultrasound tomography: First results with the computed ultrasound risk evaluation (CURE) prototype. *Med. Phys.*, 34(2):773–785, 2007.

[67] R. C. Waag, F. Lin, T. K. Varslot, and J. P. Astheimer. An eigenfunction method for reconstruction of large-scale and high-contrast objects. *IEEE Trans. Ultrason. Ferroelectr. Freq. Control*, 54(7):1316–1332, 2007.

[68] F. Simonetti, L. Huang, N. Duric, and O. Rama. Imaging beyond the born approximation: An experimental investigation with an ultrasonic ring array. *Phys. Rev. E*, 76:036601, 2007.

[69] H. Krim and M. Viberg. Two decades of array signal processing research. *IEEE Sign. Process. Magaz.*, 13(4):67–94, 1996.

[70] C. Prada and J. L. Thomas. Experimental subwavelength localization of scatterers by decomposition of the time reversal operator interpreted as a covariance matrix. *J. Acoust. Soc. Am.*, 114(1):235–243, 2003.

[71] A. J. Devaney. Super-resolution processing of multi-static data using time-reversal and music. *Unpublished*, page available at www.ece.neu.edu/faculty/devaney/ajd/preprints.htm, 2000.

[72] R. O. Schmidt. Multiple emitter location and signal parameter estimation. *IEEE. Trans. Antennas Propag.*, AP-34(3):276–280, 1986.

[73] M. S. Barteltt. Smoothing peridograms from time series with continuous spectra. *Nature*, 161:686–687, 1948.

[74] R. T. Lacoss. Data adaptive spectral analysis methods. *Geophysics*, 36(4):661–675, 1971.

[75] J. Capon. High-resolution frequency-wavenumber spectrum analysis. *Proc. IEEE Trans.*, 57(8):1408–1418, 1969.

[76] E. A. Marengo and F. K. Gruber. Subspace-based localization and inverse scattering of multiply scattering point targets. *EURASIP J. Adv. Sign. Processing*, 2007:ID 17324 16 pages, 2007.

[77] A. Kirsch. The MUSIC algorithm and the factorization method in inverse scattering theory for inhomogeneous media. *Inverse Probl.*, 18:1025–1040, 2002.

[78] H. Zhao. Analysis of the response matrix for an extended target. *SIAM Appl. Math.*, 64(3):725–745, 2004.

[79] E. A. Marengo, F. K. Gruber, and F. Simonetti. Time-reversal music imaging of extended targets. *IEEE Trans. Image Process.*, 16(8):1967–1984, 2007.

[80] S. Hou, K. Solna, and H. Zhao. A direct imaging algorithm for extended targets. *Inverse Probl.*, 22:1151–1178, 2006.

[81] L. L. Foldy. The multiple scattering of waves. i. general theory of isotropic scattering by randomly distributed scatterers. *Phys. Rev.*, 67(3):107–119, 1945.

[82] V. Twersky. Multiple scattering of waves and optical phenomena. *J. Opt. Soc. Am.*, 52(2):145–171, 1961.

[83] I. Tolstoy. Superresonant systems of scatterers. i. *J. Acoust. Soc. Am.*, 80(1):282–294, 1986.

[84] I. Tolstoy and A. Tolstoy. Superresonant systems of scatterers. ii. *J. Acoust. Soc. Am.*, 83(6):2086–2096, 1988.

[85] E. J. Heller. Quantum proximity resonance. *Phys. Rev. Lett.*, 77(20):4122–4125, 1996.

[86] J. S. Hersch and E. J. Heller. Observation of proximity resonances in a parallel-plate waveguide. *Phys. Rev. Lett.*, 81(15):3059–3062, 1998.

[87] F. Simonetti. Localization of point-like scatterers in solids with subwavelength resolution. *Appl. Phys. Lett.*, 89:094105, 2006.

[88] K-J. Bathe. *Finite Element Procedures*. Prentice-Hall, New Jersey, 1996.

[89] S. F. Brown. Hands on computing. *Scientific American*, 299(1):64–67, 2008.

[90] S. Zhu, A. W. Yu, D. Hawley, and R. Roy. Frustrated total internal reflection: A demonstration and review. *Am. J. Phys.*, 54(7):601–607, 1985.

[91] I. N. Court and F. K. von Willisen. Frustrated total internal reflection and application of its principle to laser cavity design. *Applied Optics*, 3(6):719–726, 1964.

[92] R. V. Craster, A. V. Shanin, and E. M. Doubravsky. Embedding formulae in diffraction theory. *Proc. R. Soc. Lond. A*, 459:2475–2496, 2003.

[93] M. Born and E. Wolf. *Principles of Optics*. Cambridge University Press, Cambridge, 1999.

[94] R. Harrington. *Time-harmonic electromagnetic fields*. McGrow-Hill, New York, 1961.

List of Publications

[P1] M. Fleming, M. J. S. Lowe, F. Simonetti and P. Cawley. Super Resolution Imaging: Performance Studies. *Review of Progress in Quantitative NDE*, 25:736-743, American Institute of Physics, Melville, New York, 2006.

[P2] F. Simonetti, M. Fleming and E. Gruber. Illustration of the role of multiple scattering in subwavelength imaging from far-field measurements. *J. Opt. Soc. Am.*, 25(2):292-303. February 2008.